Mechanics of fracture and flexure in Antarctic Ice Sheets and Ice Shelves

Hanwen Zhang

St John's College

University of Oxford

A thesis presented for the degree of

Doctor of Philosophy

Trinity 2024

Acknowledgements

First and foremost, I would like to thank my supervisors, Prof. Richard Katz and Prof. Laura Stevens, for their support and guidance throughout my PhD over the past four years. My journey into earth sciences began with a summer internship modelling mantle two-phase flow under Rich's mentorship. This experience later paved the way for my introduction to glaciology with Laura. It has been a truly rewarding journey, filled with mathematical modelling and fascinating glaciological challenges. From my supervisors, I have gained invaluable insights—not only on becoming a good scientist but also on being a supportive teacher and a responsible colleague.

I'm grateful to all FOALAB group members, Adina Pusok, Yuan Li, Tim Davis, Hamish Hay and Luke Kearny for their support and engaging discussions. Beyond the Department of Earth Sciences, I thank Prof. Ian Hewitt, Prof. Ching Yao-Lai, Prof. Dominic Vella, Prof. Brad Lipovsky, Prof. Luke Trusel and many other researchers for insightful suggestions and productive discussions.

I would also like to express my gratitude to all the staff of the Department of Earth Sciences and St John's College for their excellent support with accommodation, dining, administrative tasks, and IT services. Their efforts have provided a solid foundation for both our daily life and work.

I am fortunate to have been surrounded by many friends who supported me throughout my PhD journey: Tian Meng, Qiong Zhang, Anran Cheng, Qi Ou,Biao Wang, Xiaoxu Ma, Suyue Li, Chong Xu, Deze Liu, Yangfan Huang and many others. Life in Oxford became enjoyable thanks to your friendship. Finally, I would like to thank my parents, Guoyuan Zhang and Zhixia Hou. It was your love and understanding that have guided me forward.

Declaration

I, Hanwen Zhang, declare that except where explicitly stated otherwise in the text, the dissertation has been composed by myself under the supervision of Prof. R. F. Katz and L. A. Stevens. This work has not been submitted for any other degree or processional qualification.

Chapter 2 is based on a paper by H. Zhang, T. Davis, R. F. Katz, L. A. Stevens and D. May, published on the Journal of Glaciology.

Chapter 3 is based on a paper by H. Zhang, R. F. Katz, L. A. Stevens, under review by The Cryosphere.

Hanwen Zhang	16/08/2024
Signature	*Date*

Abstract

Understanding the mass balance of the Antarctic and Greenland ice sheets is essential to make accurate projections of global sea-level rise. Beyond their mechanics as viscous fluid flows, the mass balance is influenced by fracturing, a complex and challenging aspect of glaciology. In grounding zones and floating ice shelves, ice fracturing is often associated with flexure modulated by ocean tides and subglacial water flow, as well as stresses created by shearing, such as pinning points. Fracture and flexure significantly affect the vulnerability of Antarctic ice shelves to hydrofracturing and, by altering buttressing effects, the mass balance of the entire Antarctic Ice Sheet. In this thesis, I investigate the mechanics of ice fracture and flexure, as well as their potential impact on ice sheet mass balance using mathematical modelling and geospatial data analysis.

Chapter 1 provides an introduction to the context of my studies, including key topics such as sticky patches beneath grounded ice sheets and glaciers, tidally-modulated grounding line and ice–shelf calving front. In chapter 2, I consider basal fracturing in grounded glaciers and ice sheets. Sticky patches are regions with higher basal shear stress than their surroundings. By including basal shear stresses in the classical, vertical mode-I fracture model, I model basal hydrofracturing on the ice–bedrock interface near a sticky patch. The study shows the importance of spatially varying basal conditions in promoting water-assisted crevassing on the ice–bed interface.

In Antarctic grounding zones, where grounded ice sheets transition to floating ice shelves, ice experiences changing basal conditions and tidal flexure, which can promote fracturing. Meanwhile, meltwater from supraglacial lakes can provide additional stress that opens a fracture. In chapter 3, I develop a viscoelastic marine ice sheet model and study tidal flexure together with hydrofracture propagation. The model suggests that tidal

flexural stress significantly contributes to hydrofracturing in the grounding zones, and aligns well with remotely sensed data from the Amery Ice Shelf grounding zone.

Tidal flexure can also be modified by subglacial hydrology. To explore the effect of subglacial hydrology on the grounding line (GL) and tidal flexure, in chapter 4 I develop a model combining a viscoelastic ice stream and subglacial hydrology. Previous studies have examined these processes using a 2D elastic framework or 3D regional-scale ice sheet model. My model serves as an intermediate state, which makes predictions of tidal variations in velocity and provides a mechanistic understanding of the tidal flexure of an ice stream with a subglacial hydrological system.

In chapter 5, I focus on calving and flexure near the shelf edge. By using a viscoelastic flexure model, I investigate different mechanisms that cause flexure near the calving front, and how the flexure evolves due to viscous creep and leads to calving events.

Keywords— Tidal flexure - hydrofracturing - Antarctic grounding zone - subglacial hydrology

Table of Contents

List of Figures

List of Tables

List of Abbreviations

IPCC . . . . . Intergovernmental Panel on Climate Change

WAIS . . . . . West Antarctic Ice Sheet

LEFM . . . . . Linear Elastic Fracture Mechanics

SIF . . . . . stress intensity factor

GL . . . . . Grounding line

1 | Introduction

The Antarctic ice sheet is an important component of the Earth's climate system. With an area of 14 million km^2 and a total volume of 27 million km^3 ice, it holds 61 % of Earth's fresh water and has a potential to raise the eustatic global sea level by 58 metres (Morlighem et al., 2017). According to the Intergovernmental Panel on Climate Change(IPCC) Special Report on the Ocean and Cryosphere in a Changing Climate (Meredith et al., 2019), the Antarctic Ice Sheet is projected to contribute 12cm global sea level rise by 2100 under RCP8.5. Moreover, for the West Antarctic Ice Sheet (WAIS) that sits on the bedrock below sea level, the contribution may be increased by the fast and irreversible retreat caused by marine ice sheet instability related to bed topography, as well as marine ice cliff instability that are usually associated with fracturing and flexure of ice (e.g., Pattyn, 2018).

Unlike the Greenland ice sheet, which experiences significant surface melting, the Antarctic Ice Sheet has minimal surface melting. Instead, it loses mass primarily through glaciers feeding into the floating ice shelves, where basal melting and calving control ice mass loss (Pritchard et al., 2012; Depoorter et al., 2013; Rignot et al., 2019). Ice shelves provide resistive stress that slows the ice flow of inland ice sheets, known as the buttressing effect. In grounding zones, ice becomes afloat and undergoes flexure modulated by ocean tides and subglacial water flow. With atmospheric warming and increasing meltwater accumulation on the surface, Antarctic ice shelves might be destabilised by hydrofracturing (Lai et al., 2020), assisted by local extensional stresses such as flexural stress. Understanding the vulnerability of the Antarctic Ice Sheet to fracturing requires knowledge of ice flexure and fracture: their causes and their contributions to ice flow dynamics. The thesis aims to address these issues using a combined approach of mathematical modelling and data analysis.

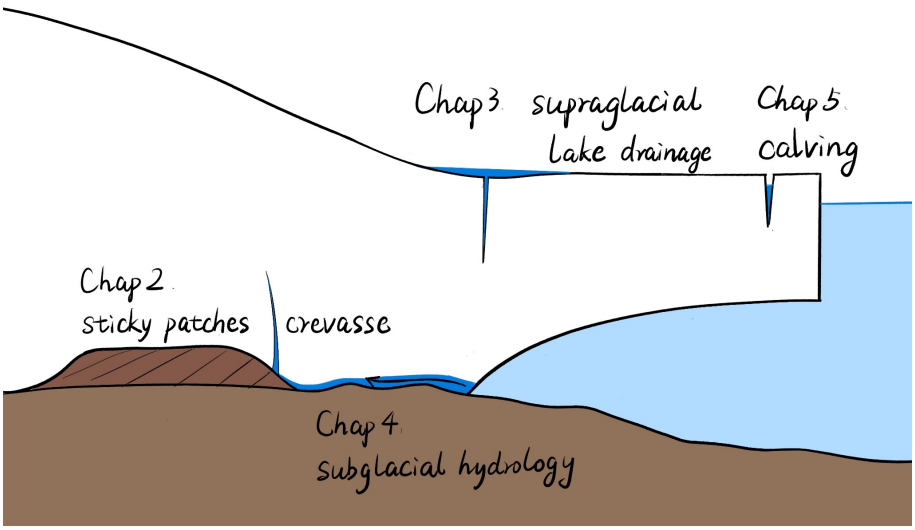

Figure 1.1: Research topics included in this thesis. The arrow on the ice–bed interface near the grounding line was intended to indicate subglacial water intrusion.

Fig. 1.1 is a schematic of different topics included in the thesis. The remainder of this thesis is organised as follows:

Chapter 2 — By modelling propagation of basal hydrofractures under spatially-nonuniform basal friction in a Linear Elastic Fracture Mechanics (LEFM) framework, I investigate how sticky patches(regions with excess shear stress on the ice–bed interface), promote basal hydrofracturing.

Chapter 3 — Using an idealised viscoelastic marine ice sheet model, I investigate tidally induced grounding line migration and flexure in a grounding zone that resembles that of the Amery Ice Shelf. I use a LEFM model to derive a criterion for lake drainage through hydrofracturing in the Amery grounding zone under the influence of tidally-induced flexure.

Chapter 4 — As an extension to chapter 3, I develop a 2D flowline model that captures the coupled dynamics of a viscoelastic ice sheet and ice shelf and the subglacial hydrology subject to tidal forcing. The model is used to

understand how tidal flexure affects the ice-flux rate across the grounding line, and to explain why tidal responses at different glaciers show different frequencies.

Chapter 5 — I model the viscoelastic flexure near the calving front of an ice shelf. The model helps to explain the "rampart–moat" profile observed near the Ross Ice Shelf edge and can be used to derive a calving mechanism from shelf-edge flexure.

In the following sections, I provide background motivation for each chapter. The study incorporates several methods including

LEFM theory,

Viscoelasticity,

Thin-plate theory.

1.1 Basal hydrofractures and sticky patches

In this chapter, we consider fracturing in grounded ice sheets and glacier that are driven by gravity and subject to basal resistance. In grounded ice sheets and glaciers, flexure is limited because basal ice is in contact with the underlying bedrock. Therefore, this chapter is focused on fracturing, particularly the water-assisted crevassing of basal ice, which we will refer to as basal hydrofracturing. As a typical type of ice fracturing, crevasses are deep cracks in glaciers, ice sheets and ice shelves. Based on their position in the ice, they can be classified as surface crevasses or basal crevasses. On ice shelves, the propagation of surface and basal crevasses is a precursor to calving and rifting, and thus affects the vulnerability of ice shelves to hydrofracturing (Scambos et al., 2000; Glasser and Scambos, 2008; Banwell et al., 2013; Bassis and Ma, 2015; Banwell et al., 2019; Lai et al., 2020;

Warner et al., 2021; Lipovsky, 2020). In grounded ice, basal crevasses may have important influences on subglacial hydrology and glacier dynamics (Das et al., 2008; Walter et al., 2013; Doyle et al., 2013; Tedesco et al., 2013; Stevens et al., 2015; Dunmire et al., 2020). Crevasses are also a potential explanation for seismic activity detected in glaciers and ice sheets (Hudson et al., 2020). In alpine glaciers, (Walter et al., 2013; Helmstetter et al., 2015) have detected clustered, deep icequakes with non-double-couple sources. In cryoseismology, double-couple icequake sources typically originate from pure shear mechanisms, such as stick-slip motion along the ice–bed interface. In contrast, non-double-couple sources are attributed to tensile mechanisms, producing icequakes with an isotropic component in the moment tensor, which cannot be explained by shearing. Instead, Walter et al. (2013) attributed these icequakes to opening-mode fractures deep within the ice. Basal crevasses have been studied less than surface crevasses because observations of basal crevasses are few, and because complicated, heterogeneous conditions characterise the ice–bed interface. The propagation of basal crevasses can be very sensitive to basal conditions, including subglacial hydrological conditions and bedrock rigidity (Jimenez and Duddu, 2018).

Various observations document the existence of basal crevasses. At Bench Glacier, Alaska, crevasses with connections to the bed were detected by both drilling experiments and radar imaging (Harper et al., 2010). Such crevasses, filled by high-pressure water, serve as important components of the subglacial hydrology system. In West Antarctica, Wearing and Kingslake (2019) detected relic basal crevasses in grounded regions of the Henry Ice Rise of the Ronne Ice Shelf using ice-penetrating radar. To consistently explain the formation of these buried relic crevasses on the ice rise, they proposed a conceptual model where the floating ice shelf re-grounds on high points of the bedrock, leading to upstream thickening and downstream crevassing. Here, the ice–bed contacts are areas where the basal

shear stress is higher than the nominally stress-free ice–sea water interface.

The complexity of basal crevasses arises from the heterogeneous condition of the ice–bed interface. Basal conditions of grounded ice sheets such as subglacial water pressure, basal shear stress and temperature vary spatially and temporarily (Anandakrishnan and Winberry, 2004; Joughin et al., 2004; Luthra et al., 2016; Colleoni et al., 2018; Kufner et al., 2021). For some ice streams of the Antarctic Ice Sheet, rib-like patterns of high basal shear stress are inferred on the basis of inversions of surface data (Sergienko and Hindmarsh, 2013). Other studies have argued that spatial and temporal variation of ice flow and surface velocity are a consequence of basal "sticky spots" (referred to here as sticky patches) that have higher basal shear stress than their surroundings (Stokes et al., 2007). The existence of sticky patches has significant influence on the nonuniformity of ice-flow dynamics (Wolovick et al., 2014). This arises an important question: *do the non-uniform basal conditions caused by sticky patches modulate surrounding basal crevassing?*

To advance our understandings of basal crevassing under grounded ice sheets, we model hydrofracture propagation under spatially-nonuniform basal friction in a Linear Elastic Fracture Mechanics (LEFM) framework. We investigate how sticky patches promote basal hydrofracturing and explore the relevant dimensionless parameters that control basal hydrofracturing.

1.2 Supraglacial lake drainage at the grounding line

The grounding line is as an internal boundary connecting a grounded ice sheet and a floating ice shelf. Retreat of the grounding line on retrograde slopes can potentially increase the ice flux through the grounding line, thereby accelerating the retreat—a positive feedback known as marine ice sheet instability (e.g., Pat-

tyn, 2018; Pattyn and Morlighem, 2020). Meanwhile, the grounding-line migration also occurs diurnally and fortnightly, which is subject to ocean tides. At the Amery Ice Shelf, East Antarctica, kilometre-scale tidal grounding-line migration with seawater intrusion has been observed from differential radar interferometry (Chen et al., 2023). The observed grounding zone is much larger than it would be if predicted from hydrostatic equilibrium. Model simulations (Rosier and Gudmundsson, 2020) suggest that tidal flexure might influence long-term ice mass balance, which is currently not well understood and not considered in large-scale ice models. Therefore, it is essential to address the question of *how ocean tides modulate the dynamics of marine ice sheets*.

In addition, tidal flexure can drive hydrofracturing in the grounding zone. In East Antarctica, satellite imagery suggests that supraglacial lakes often cluster in the grounding zone, particularly at low elevations and bedslopes (Stokes et al., 2019). Lakes drain either slowly, through surface drainage channels (Banwell et al., 2019), or rapidly, through hydrofractures (Das et al., 2008). Recently, Trusel et al. (2022) reported a series of repeated hydrofracturing drainage events of a supraglacial lake at the grounding line of the Amery Ice Shelf, East Antarctica. Interestingly, these drainage events did not occur when a threshold in lake volume was crossed, but rather tended to coincide with times of high daily tidal amplitude. Trusel et al. (2022) hypothesised that near the grounding line, the drainage events are promoted by tensile stress due to tidal flexure. These observations raise the question of *how tidal flexure near the grounding line contributes to lake drainages through hydrofracturing*?

In chapter 3, to test this, I present a numerical model that accounts for the tidal contribution to hydrofracturing near the Amery Ice Shelf grounding line. This enables me to derive a model-based criterion for supraglacial lake drainage in terms of tidal amplitude and lake-water depth, which I compare to the lake-drainage time

series presented by Trusel et al. (2022). Its results support the hypothesis that at the Amery Ice Shelf grounding line, supraglacial lake drainage is controlled by both lake depth and tidal amplitude.

1.3 Tidal subglacial hydrology and grounding line

Tidal grounding-line migration is influenced not only by ice rheology and bedrock profile, but also by subglacial hydrology, which I address in chapter 4. In chapter 3, for simplicity, I focused on the viscoelastic dynamics of the ice flow and assumed that the water pressure is hydrostatic on the ice–ocean interface. However, for fast-flowing ice streams and tidewater glaciers with grounding zones (WaIters, 1989; Reeh et al., 2000; Podrasky et al., 2014), the subglacial drainage system is an important component of basal slip and grounding-line dynamics. Subglacial water in the grounding zone reduces basal friction by lubricating the ice–bed interface. It can thereby cause tidal variations in ice velocity. A full-Stokes simulation of the entire Filchner-Ronne Ice Shelf suggested the importance of asymmetric grounding-line migration and lubrication caused by subglacial hydrology in producing the nonlinear tidal response of the horizontal displacement to tidal forcings (referred to as "nonlinear tidal response" from this point forward for simplicity) at the Rutford Ice Stream (Rosier and Gudmundsson, 2020). Warburton et al. (2020) modelled the combined elastic flexure and subglacial water flow to investigate the effect of subglacial hydrology on tidally induced grounding-line migration. The results show that a retained water layer appears on the ice–bed interface at low tides, causing detachment of basal ice from hosting bedrock and thus asymmetric grounding-line migration with respect to tidal height. This gives a mechanistic explanation of the non-linear tidal response of the Rutford Ice Stream.

In chapter 4, to address the problem that *how subglacial drainage system con-*

tributes to viscoelastic grounding-line dynamics, I combine a subglacial hydrology model with a vertically integrated viscoelastic grounding-line model and quantify the effect of subglacial hydrology on ice flow rates and tidal flexure. The model extends the mechanistic understanding from Warburton et al. (2020), and predicts the surface velocity and tidal variations in the surface elevation that can be compared with observations.

1.4 Ice flexure near the shelf edge and calving

As the floating extension of ice sheets, ice shelves are subject to membrane stress, flexure and fracturing. Calving, the breaking of icebergs from the shelf edge, remains one of the most critical and challenging problems in modelling the Antarctic Ice Sheet and projecting global sea-level change (Depoorter et al., 2013). In Antarctica, calving is a major ablation process and plays a crucial role in controlling the mass balance of the Antarctic Ice Sheet. The physics of calving is complex, involving factors such as longitudinal stretching, flexure, fracturing, and melting. The modes of calving vary according to the scale of the icebergs, ranging from the detachment of small icebergs from Greenland tidewater glaciers to the breaking of giant tabular icebergs typically observed on Antarctic ice shelves (Lazzara et al., 1999; Fricker et al., 2002; Bassis and Jacobs, 2013). Different calving laws are used to parameterize calving in ice sheet models based on these variations (Wilner et al., 2023).

Although the physics behind calving is not fully understood, empirical observations of calving rates have suggested that along-flow extension a major control on calving (Alley et al., 2008). Besides surface hydrofracturing, calving is promoted by several other factors that induce along-flow extensional stress. When an ice shelf bends due to gravity and other external forces, hydrofracturing can be

driven by flexural stress. Buck and Lai (2021) studied basal crevasse propagation in a floating ice shelf with flexure using high-resolution numerical simulations. MacAyeal and Sergienko (2013) estimated the flexural stress within an ice shelf with dolines and supraglacial lakes. Recently, Banwell et al. (2024) observed meltwater-induced flexure and fracture on the George IV Ice Shelf. Viscous flexure modelling suggested that flexural stress, with magnitudes up to 75 kPa, caused a "ring fracture" filled with surface meltwater.

Flexure also occurs near the shelf edge. ICESat elevation profiles of the Ronne Ice Shelf have shown two types of flexure at the ice-shelf edges and iceberg edges (Scambos et al., 2005). In cold areas covered with sea ice, berms about 0.6 meters high have been observed, with the outer edge sloping several meters downwards to the sea. In warmer regions, iceberg edges are raised, forming ramparts 2-to-5 metres high and upstream, edge-parallel moats 50-to-100 centimetres deep. Recent studies have proposed two different mechanisms to explain the rampart–moat profile. Sartore et al. (2024) analyzed the rampart–moat profile on the Ross Ice Shelf and suggested that underwater ice feet, protruding beyond the ice cliff, provide additional buoyancy force, contributing to the observed flexure near shelf edges, which is referred to as “footloose" mechanism (Wagner et al., 2014, 2016; Mosbeux et al., 2020). Conversely, Buck (2024) explained the profile as a result of the internal bending moment caused by vertically non-uniform ice temperature and viscosity acting on the extensional stress. Therefore, *the major control of flexure near the shelf edge* remains unclear, which I want to address in chapter 5.

Using scaling analysis, Hindmarsh (2012) investigated the viscous ice flow within a boundary layer at the calving front, which was later shown to align well with observed calving events in Antarctic ice shelves (Wearing et al., 2015). Christmann et al. (2016, 2019) considered the two-dimensional Maxwell viscoelastic ice shelf, creating a framework for numerically modeling time-dependent stress

and strain at the calving front. In chapter 5, using viscoelastic beam- bending theory, I model the evolution of flexure near the shelf edge analytically, considering both the footloose mechanism and non-uniform viscosity. My study provides a comprehensive framework that includes different factors related to shelf-edge flexure and predicts the evolution of shelf deflection, which can be compared with remotely sensed data.

Following “the direction of the ice flow", this thesis begins in chapter 2 by exploring the basal hydrofracturing in grounded ice sheets and glaciers. It then transitions to tidal flexure and fracturing in the grounding zone in chapter 3 and chapter 4, and finally examines flexure near the calving front in chapter 5.

2 | Basal hydrofractures near sticky patches

Statement of Authorship for joint/multi-authored papers for PGR thesis

To appear at the end of each thesis chapter submitted as an article/paper

The statement shall describe the candidate's and co-authors' independent research contributions in the thesis publications. For each publication there should exist a complete statement that is to be filled out and signed by the candidate and supervisor **(only required where there isn't already a statement of contribution within the paper itself).**

Title of Paper	Basal hydrofractures near sticky patches
Publication Status	☑ Published □ Accepted for Publication □ Submitted for Publication □ Unpublished and unsubmitted work written in a manuscript style
Publication Details	Hanwen Zhang, Timothy Davis, Richard F. Katz, Laura A. Stevens, and Dave A. May. Basal hydrofractures near sticky patches. Journal of Glaciology, page 1–12, 2022. doi: 10.1017/jog.2022.75.

Student Confirmation

Student Name:	Hanwen Zhang		
Contribution to the Paper	The general idea arose during a conversation with P.~Christoffersen and R.~Law. I set up the mathematical model of basal hydrofractures and performed the Finite Element Method (FEM) simulations. I performed the Boundary Element Method (BEM) simulations with the assistance of Dr. Davis, who developed the BEM code. I summarised the results and wrote the manuscript.		
Signature	Hanwen Zhang	Date	08/07/2024

Supervisor Confirmation

By signing the Statement of Authorship, you are certifying that the candidate made a substantial contribution to the publication, and that the description described above is accurate.

Supervisor name and title:	Professor Richard F Katz	
Supervisor comments I confirm what Hanwen has written above is true. I certify that the candidate made a substantial contribution to the publication, and that the description described above is accurate.		
Signature	Date	08/07/24

This completed form should be included in the thesis, at the end of the relevant chapter.

This work has been published as (Zhang et al., 2023). Above is the statement of authorship.

2.1 Introduction

The key hypothesis of this study is that for grounded regions of glaciers and ice sheets, variation of basal-stress conditions near sticky patches can promote basal crevassing, while high basal water pressure remains the prerequisite. We quantify and explore the fracturing process induced by a combination of water pressure and sticky patches. This arrangement is different from the process of pure hydrofracturing, as considered by Smith (1976) and Van der Veen (1998). At long timescales, glacial ice deforms as a viscous fluid, with a viscosity modelled by Glen's law (Glen, 1955), which states that the viscosity has a power-law relation to the effective stress. The fracturing process, however, typically occurs on a shorter timescale over which ice behaves elastically. Therefore, Linear Elastic Fracture Mechanics (LEFM) theory is widely used to explore the existence and growth of cracks in ice. Van der Veen (1998) applied LEFM to develop elastic models of surface and basal crevassing, with the assumption that basal crevasses are mode-I (i.e., opening) cracks propagating vertically in ice. More recently, Jimenez and Duddu (2018) reassessed a key component of previous LEFM models of crevassing, finding that the basal boundary conditions influence the crevasses. For grounded ice sheets, Jimenez and Duddu (2018) recommended a LEFM weight function from Tada et al. (2000) to study opening-mode fractures analytically.

The application of LEFM is not limited to opening-mode fractures, however. In several studies, LEFM is applied to calculating mixed-mode stress intensity factors in rift propagation on ice shelves in two dimensions (Hulbe et al., 2010) and

three dimensions (Lipovsky, 2020). Here, we use LEFM theory in the context of two-dimensional elasticity to explore the mixed-mode (in-plane opening mode and shearing modes) basal crevasses arising from sticky patches.

The chapter is organised as follows. In the model section we introduce the mathematical theory and its numerical implementation. The results section illustrates the essential mechanics and shows the dependence of crack propagation on physical parameters. We first consider crack propagation under the mode-I fracture assumption followed by a consideration of curved fracture trajectories produced by mixed-mode fracturing. We find that the propagation of basal crevasses is controlled by basal water pressure, the size of the sticky patch, and the stress variation between the sticky patch and the neighbouring bed. We then evaluate how these parameters affect the trajectories of basal crevasses. The discussion section explores the thermal consequences of basal crevasses, potential applications of the model to real ice sheets, and limitations of the model.

2.2 Governing equations and model set-up

We model a grounded ice sheet sliding due to gravity, influenced by a sticky patch. Under the assumption of plane strain (i.e., there is no cross-stream elastic strain), we model the ice sheet with a two-dimensional, infinite elastic strip on a slope. Figure 2.1 shows a schematic diagram of the mathematical model, which considers a finite length of the strip that extends across a sticky patch. The total system is decomposed into two different sub-problems, based on the two components of the gravity vector in the tilted coordinate system. The first sub-problem addresses the sliding state, where steady sliding is driven by down-slope component of gravity g_x and resisted by uniform basal stress (Fig. 2.1a). The second sub-problem is the sticky state, where the sticky patch provides additional basal drag, leading to

tensile stress that partially offsets the static compression due to g_z (Fig. 2.1b).

In the first sub-problem, the ice strip with height H and length $2L$ ($L \gg H$) is sliding at a constant speed. A uniform basal shear stress τ_0, representing background basal drag, is imposed on $(-L, L)$. The uniform basal stress τ_0 exactly balances the down-slope component of gravity g_x, leading to steady sliding with internal deformation (to maintain torque balance). This is consistent with the fact that the ice-sheet motion can be decomposed into basal sliding and internal deformation (Van der Veen, 2013).

In the second case of panel (b), we focus on the influence of a sticky patch by treating it as a superposition to the steady, sliding state. To model the stickiness of the sticky patch, an excess shear stress $\Delta\tau$ is imposed on $x \in [-W, W]$ at $z = 0$. Since the down-slope component of gravity is already balanced by τ_0 in panel (a), this excess traction needs to be balanced in order for there to be a steady state. We add an uniform increment of traction $W\Delta\tau/L$ in the opposite direction on $x \in [-L, L]$ at $z = 0$ — along the whole bottom boundary of the finite ice strip. This extra increment of uniform traction vanishes for $W/L \to 0$; for $W/L \ll 1$ it has little effect on basal stress estimates around the sticky patch.

In panel (b), the excess traction on $-W$ to W at $z = 0$ creates tension on the downstream side of the sticky patch. If that tension, combined with basal water pressure, is large enough to overcome the ice overburden pressure plus the fracture toughness of ice, basal crevassing should occur. In natural ice sheets, the basal drag on the sticky patch $\Delta\tau$ can be much larger than the background basal drag τ_0 (Sergienko and Hindmarsh, 2013). Therefore, in regions close to the sticky patch, the elastic deformation caused by the uniform basal drag is negligible compared with the effect of the patch. From this point forward, we will only focus on the model in panel (b), which accounts for the effect of the sticky patch.

Based on LEFM theory, the stress intensity factors (SIFs) are calculated and used to predict the maximum penetration of the crack (Broek, 1982). Stress intensity factors are parameters that describe the stress distribution and magnitude close to the crack tip. A more detailed discussion of stress intensity factors can be found in the following subsections.

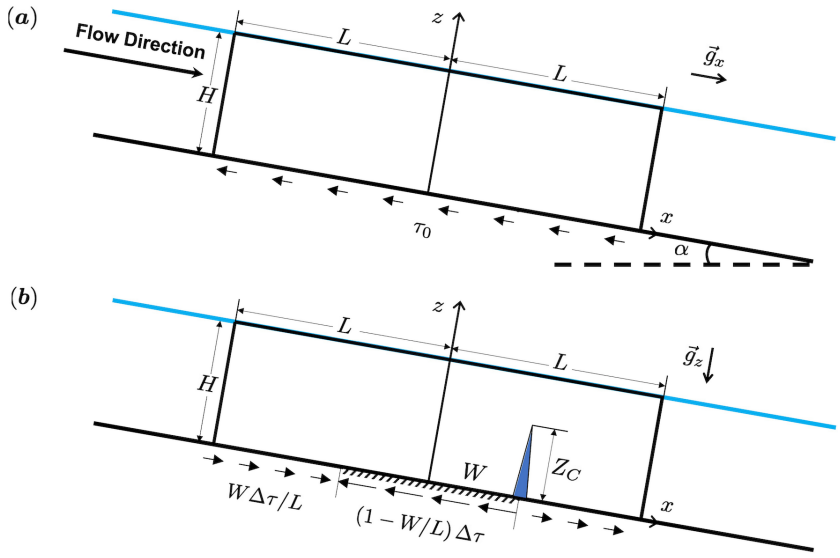

Figure 2.1: Schematic diagram of the computational domain: a $2L \times H$ strip extracted from the ice sheet on a slope with angle α. **(a)** The first sub-problem where ice is sliding at a constant rate under a uniform basal drag τ_0. **(b)** The second sub-problem where there is a stick patch and a hydrofracture downstream. The sticky patch is represented by an interval $[-W, W]$ on the x-axis with excess basal stress $\Delta\tau$. A water-filled crack is initiated on the downstream end of the sticky patch. The crack can be a vertical line with length Z_C (as illustrated in the figure), or a curve, depending on the criterion used to determine its propagation.

2.2.1 2D elastic model of basal hydrofracture

Focusing on sub-problem (b) shown in Figure 2.1(b), the equation governing the conservation of momentum in ice is

$$\boldsymbol{\nabla} \cdot \boldsymbol{\sigma} - \rho_i g_z \hat{\boldsymbol{z}} = \mathbf{0}, \tag{2.1}$$

where $\boldsymbol{\sigma}$ is the Cauchy stress tensor (tensile stress is positive), ρ_i is the density of ice, $g_z = g\cos\alpha$ is the z-component of gravity, and $\hat{\boldsymbol{z}}$ is the unit vector in positive-z direction. With the assumption that slope $\alpha \ll 1$, we take $g_z \approx g$ in the following calculations. Both side boundaries of the ice strip are loaded by a depth-dependent compression $\rho_i g\,(z-H)$ that represents the overburden stress due to the weight of the overlying ice,

$$\boldsymbol{\sigma}\cdot\boldsymbol{n} = \rho_i g\,(z-H)\,\boldsymbol{n} \quad \text{for} \quad x = \pm L, \tag{2.2}$$

where $\boldsymbol{n}$ is the outward-pointing unit normal vector of the domain. The top boundary is assumed to be traction free, neglecting the atmospheric pressure and other traction on the surface,

$$\boldsymbol{\sigma}\cdot\boldsymbol{n} = \boldsymbol{0} \quad \text{for} \quad z = H. \tag{2.3}$$

On the ice–bed interface $(z=0)$, we impose a zero-displacement boundary condition in the z-direction and the excess traction $\Delta\tau$ in x-direction,

$$\boldsymbol{u}\cdot\boldsymbol{n} = 0, \tag{2.4}$$

$$\boldsymbol{t}\cdot\boldsymbol{\sigma}\cdot\boldsymbol{n} = \tau\,(x,0) = \begin{cases} -\dfrac{W}{L}\Delta\tau & |x| \geq W, \\ \left(1-\dfrac{W}{L}\right)\Delta\tau & |x| < W, \end{cases} \tag{2.5}$$

where $\Delta\tau$ represents the stress variation caused by a sticky patch, $\boldsymbol{u}$ is the displacement, and $\boldsymbol{t} = -\hat{\boldsymbol{x}}$ is the unit tangent vector to the boundary. On the bottom, $\boldsymbol{t}$ is in the negative x-direction. The extra term $-W\Delta\tau/L$ is for force balance, as discussed above. Physically, we balance the excess shear stress on the sticky patch using a uniform stress on a much larger area. In our computation, the ratio W/L is set to be 0.1, which is small enough to make the effect of the extra term unimportant.

Crack walls are loaded by water pressure that is, in general, dependent on the subglacial hydrology. In this study, we assume static basal water pressure and represent subglacial hydrology in terms of the flotation fraction, which is the ratio of basal water pressure to basal overburden pressure,

$$f = \frac{p_w}{\rho_i g H} = \frac{\rho_w g H_w}{\rho_i g H}, \tag{2.6}$$

where H_w is the piezometric head measured in borehole experiments as $p_w = \rho_w g H_w$ (Harper et al., 2010). The fracture is assumed to initiate at $x = W$, where tensile stress is maximum, and reach a height Z_C that is to be determined. Using Eq. 2.6, the boundary conditions on the crack walls ($x = W$, $0 \leq z \leq Z_C$) can be written in terms of f and z,

$$\boldsymbol{\sigma} \cdot \boldsymbol{n} = \begin{cases} \rho_i g H \left(\dfrac{\rho_w}{\rho_i} \dfrac{z}{H} - f \right) \boldsymbol{n} & \text{at} \quad z < H_w, \\ \mathbf{0} & \text{at} \quad z \geq H_w. \end{cases} \tag{2.7}$$

The transition at $z = H_w$ occurs because water rises to that height in the crevasse.

In formulating the plane-strain elastic constitutive relation, we assume that strain occurs in response to deviations from the overburden stress, as suggested by Cathles (2015). This approach was used by Lipovsky (2020) to model rift propagation in floating ice. A perturbation stress tensor $\boldsymbol{T}$ (sometimes referred to as resistive stress in glaciology), is introduced as the total Cauchy stress tensor $\boldsymbol{\sigma}$ minus the ice overburden stress,

$$\boldsymbol{T} = \boldsymbol{\sigma} + p_i \boldsymbol{I}, \tag{2.8}$$

in which $p_i = \rho_i g \left(H - z \right)$ accounts for the ice overburden pressure and $-p_i \boldsymbol{I}$ is the ice overburden stress. The elastic constitutive law linearly relates the strain to

the perturbation stress as

$$\boldsymbol{T} = \frac{E\nu}{(1+\nu)(1-2\nu)}\text{tr}(\boldsymbol{\epsilon})\boldsymbol{I} + \frac{E}{1+\nu}\boldsymbol{\epsilon}, \tag{2.9}$$

where

$$\boldsymbol{\epsilon}(\boldsymbol{u}) = \frac{1}{2}\left(\nabla\boldsymbol{u} + \nabla\boldsymbol{u}^T\right). \tag{2.10}$$

To define the constitutive law, two parameters are needed to account for ice properties. Here we use the Young's modulus $E = 10$ GPa, and a Poisson's ratio $\nu = 0.33$ (Van der Veen, 1998). Further details associated with the problem description in terms of the perturbation stress are provided in Appendix A.1.

In the computation, with the boundary conditions given above, we solve the 2-dimensional elastic problem for the displacement field $\boldsymbol{u}$. Based on this solution, we then analyze the fracture propagation using the LEFM introduced below.

2.2.2 Stress intensity factors

In LEFM theory, stress intensity factors K_I, K_{II} are used to describe the additional stress near the tip of a crack that is due to the presence of the crack (Broek, 1982),

$$\sigma_{ij}^{I}(r,\theta) = \frac{K_I}{\sqrt{2\pi r}} f_{ij}^{I}(\theta) + \boldsymbol{O}\left(r^{\frac{1}{2}}\right), \tag{2.11}$$

$$\sigma_{ij}^{II}(r,\theta) = \frac{K_{II}}{\sqrt{2\pi r}} f_{ij}^{II}(\theta) + \boldsymbol{O}\left(r^{\frac{1}{2}}\right), \tag{2.12}$$

where I, II represent two in-plane modes of cracks (opening and shearing, respectively), r and θ are coordinates in a local plane-polar coordinate system with origin at the crack tip, and f_{ij}^{I}, f_{ij}^{II} are tensor-valued functions describing the angular dependence of the excess stress. The $O\left(r^{1/2}\right)$ terms are related to far-field

stress and are omitted when r is small.

The predicted extent of the crack that is in equilibrium with the total stress field, including its direction (if not constrained to be vertical), is determined by the criterion of crack propagation. The broadly accepted G-criterion states that cracks grow in the direction along which the maximum potential energy is released (Broek, 1982). In the context of this study, the potential energy is the strain energy stored in the elastic deformation. The elastic energy released when a crack extends is measured by the release rate G, defined as the energy released per unit of crack extension. The crack extends when G is greater than or equal to G_C, a threshold value for crack growth. Equilibrium is attained when this condition is no longer met and the crack ceases to propagate.

G is related to the stress intensity factors by

$$G = G_I + G_{II} = \frac{1-\nu^2}{E}\left(K_I^2 + K_{II}^2\right), \tag{2.13}$$

where G_I and G_{II} denote the energy release rate for mode-I and mode-II components, with G_C given by

$$G_C = \frac{1-\nu^2}{E} K_{I,C}^2, \tag{2.14}$$

where $K_{I,C}$ is the fracture toughness, a material property measured in experiments. The G-criterion $(G > G_C)$ can be expressed in terms of the stress intensity factors as $K = \sqrt{K_I^2 + K_{II}^2} > K_{I,C}$. Therefore, extension of a crack occurs when the total stress intensity factor exceeds fracture toughness $K_{I,C}$. We assume that $K_{I,C} = 100$ kPa m$^{1/2}$ (Rist et al., 1996), which is an estimate widely used in ice-fracture problems.

In the results section, we first assume a vertical, pure mode-I crack and employ a simple criterion for its propagation. In particular, we neglect the mode-II compo-

nent by assuming that $K_{II} = 0$. Thus the criterion for crack extension reduces to $K_I > K_{I,C}$; if satisfied, the crack can grow vertically in length. Later we reconsider mixed-mode crack growth with $K_{II} \neq 0$ and assess the difference associated with the different criteria.

2.2.3 Non-dimensionalisation

In the results section we focus on solutions of non-dimensional problems; we denote the non-dimensional version of a variable using the same symbol appended with a prime $'$. We choose to scale length (and displacement) by H and stress by $\rho_i g H$. Hence, the conservation of momentum (Eqs. (2.1)–(2.7)) and stress intensity factors are non-dimensionalised by the following scales:

$$\boldsymbol{x}' = \frac{\boldsymbol{x}}{H}, \quad \boldsymbol{u}' = \frac{\boldsymbol{u}}{H}, \quad \boldsymbol{\sigma}' = \frac{\boldsymbol{\sigma}}{\rho_i g H}, \quad \boldsymbol{T}' = \frac{\boldsymbol{T}}{\rho_i g H}, \quad \Delta\tau' = \frac{\Delta\tau}{\rho_i g H}, \tag{2.15}$$

$$K'_{I,II,C} = \frac{K_{I,II,C}}{\rho_i g H^{3/2}}. \tag{2.16}$$

Beside the flotation fraction representing basal water pressure, there are two important, non-dimensional parameters that control fracturing, $W' = W/H$ and $\Delta\tau'$, which represent the size and excess shear stress of the sticky patch, respectively. The non-dimensional stress intensity factors and non-dimensional fracture toughness are used in the fracture criterion. Note that although the dimensional fracture toughness is a material property measured by experiments, the non-dimensional fracture toughness is scaled by $\rho_i g H^{3/2}$, giving it a dependence on the ice-sheet thickness.

2.2.4 Numerical implementation

For the vertical-line-crack problem, the governing equations are solved using an open-source finite element (FE) software library, FEniCS (Logg and Wells, 2010; Logg et al., 2012; Langtangen and Logg, 2017), with meshes generated by Gmsh (Geuzaine and Remacle, 2009). The basal crevasse is represented by a straight, triangular notch in the mesh, perpendicular to the bottom boundary. The mesh is locally refined near the tip of the notch and the bottom boundary. The mesh is composed of triangular elements, with element size varying from 5×10^{-3} times the crack length (near the tip) to 0.2 ice thicknesses (away from the tip). For an 1000 m-thick ice sheet with a 500 m-high basal crevasse, the element sizes are 2.5 m near the tip and 200 m away from the tip. SIFs are calculated by the Displacement Correlation Method (DCM) (Chan et al., 1970; Banks-Sills and Sherman, 1986) with Richardson extrapolation (Guinea et al., 2000). The code is benchmarked by comparison with a weight function from Jimenez and Duddu (2018) (see Appendix A.2).

The FEniCS code relies on meshing the interior of the elastic domain, and requires local mesh refinement at the fracture tip to resolve the stress singularity there. To perform simulations of fracture growth where the path is not specified *a priori*, this method would require repeated remeshing. Dynamic remeshing is feasible with specialised software but is unreliable and incurs a significant computational cost. To avoid such issues and to provide an additional means to verify the numerical results, we use a separate code for consideration of curved fracture trajectories. This code employs the Displacement Discontinuity Method (DDM) (Crouch and Starfield, 1982), a scheme that is based on the Boundary Element Method (BEM).

In the DDM approach, only boundaries subject to given conditions must be meshed. The interior of the domain is assumed to be a uniform, linear elastic material

that deforms according to Green's functions forced by the facets of the boundary mesh. This method avoids reliance on meshing software. To extend the fracture at a given step, a new straight-line segment is connected to the former tip of the fracture. The orientation of this new segment is defined by the optimal direction of fracture growth. The new segment must have an appropriately small length, the choice of which defines the resolution of the model. At each growth step, we test for multiple orientations of growth and choose that with the highest strain-energy release rate, as defined by the G-criterion (Dahm, 2000). The BEM code used here is developed by Davis (2017). As with the FE models, in the DDM models we subject the base of the glacier domain to the condition of no vertical displacement.

2.3 Results

Results are presented in two parts. The first is for vertical fractures and uses the FE model; the second is for mixed-mode, curving fractures and uses the DDM model.

2.3.1 Mode-I fracture growth

We consider a vertical, mode-I fracture as part of a reference case where the sticky patch has a width two times the ice thickness ($W' = 1$). The non-dimensional excess shear stress is $\Delta\tau' = 0.3$, which means the dimensional excess shear stress is $0.3\rho_i g H$. The reference flotation fraction is $f = 0.7$, which we think is a reasonable estimate (Engelhardt et al., 1990; Harper et al., 2010; Andrews et al., 2014). Cases with larger f ($0.7 \leq f \leq 1$) are also included in the following results. Figure 2.2 shows the three components of the perturbation stress that arise due to the sticky-patch excess stress and an existing basal crevasse. Among these, we are most interested in T'_{xx} and T'_{xz}, which are related to the fracture

propagation. As shown in panel (a), there is horizontal tension concentrated on the downstream (right) end of the sticky patch and compression concentrated on the upstream (left) end. In panel (b), the vertical normal stress T'_{zz} is also concentrated near the ends of the sticky patch and the crack tip. This is a consequence of the no-vertical-displacement condition Eq. 2.4 imposed on the bottom boundary. Panel (c) shows the pattern of shear stress, which is localised to a region around the sticky patch. In this reference case in Fig. 2.2, the stress intensity is $K_I/K_{I,C} = 8.75$. Thus the crack is unstable and will continue growing vertically.

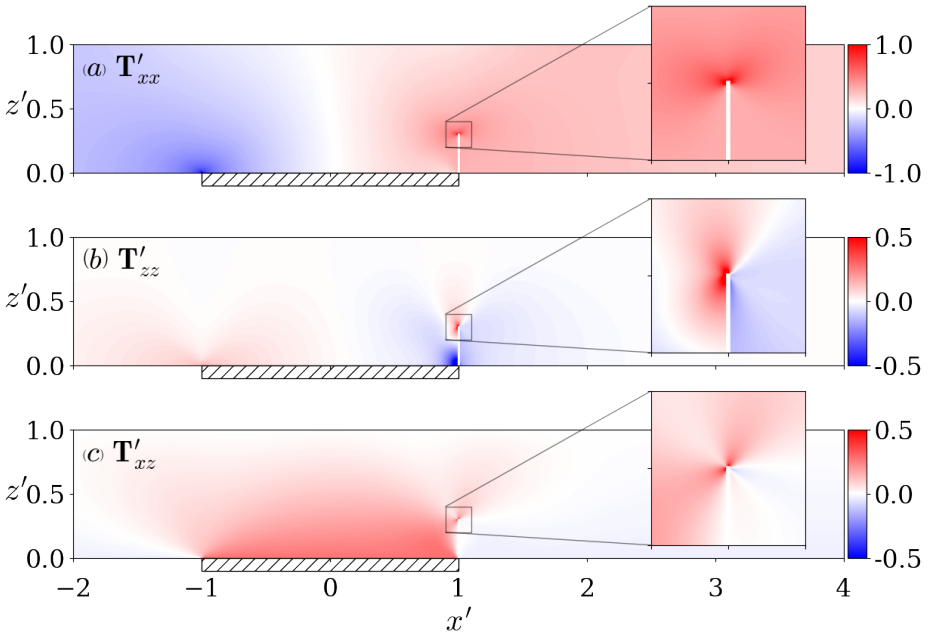

Figure 2.2: Dimensionless perturbation stress in a cracked ice-sheet with $W' = 1$, $\Delta\tau' = 0.3$, and $Z'_C = 0.3$. Panels show **(a)** T'_{xx}, **(b)** T'_{zz}, and **(c)** T'_{xz}. Tension is defined as having a positive sign. In the zoom-in box a white rectangle is added to highlight the crack, which is actually much narrower, making it difficult to see otherwise.

We are interested in the maximum stable crack length permitted by the fracture criterion, and how this depends on ice-sheet thickness and sticky-patch width. To investigate, we extend our calculation to cases with varying crack length Z'_C and

assume that the criterion for crack growth is $K'_I > K'_{I,C}$ (Van der Veen, 1998). Figure 2.3 shows the normalised stress intensity factor K_I/K_{Ic} as a function of Z'_C near the sticky patch for the reference case ($W' = 1$, $\Delta\tau' = 0.3$) and another case with smaller $\Delta\tau' = 0.2$. Comparison of the two cases show that increasing $\Delta\tau'$ leads to larger K_I. In each case, with the crack length Z'_C increasing, K'_I increases to its maximum due to tension near the sticky patch, then begins to drop and eventually reaches negative values due to overburden pressure. The maximum crack length is the value of Z'_C such that $K'_I = K'_{I,C}$ (i.e., the intersection of the K'_I curve and vertical $K'_{I,C}$ line in Figure 2.3). For the crack with this value of Z'_C to be in a stable equilibrium, the crack should be resistive to perturbations. If we add a positive perturbation $\Delta Z'_C > 0$ to the crack length Z'_C, the perturbed crack length should return to the stable state, which means $K'_I\left(Z'_C + \Delta Z'_C\right) < K'_{I,C}$. Thus, the condition for a stable crack is $K'_I = K'_{I,C}$ and $dK_I{}'/dZ'_C < 0$. In Sect. 2.3, we focus on stable cracks, where all crack solutions presented are stable. Note there is $K_I < K_{I,C}$ at small crack lengths. To propagate a basal crevasse, an initial flaw or crack of adequate length and orientation is required (Van der Veen, 1998). Here we simply assume a preexisting vertical line crack with $K_I > K_{I,C}$.

Figure 2.4 shows the maximum stable crack length $Z'_{C,max}$ as a function of dimensionless problem parameters $\Delta\tau'$ and W' for an ice thickness of 100 m. In panel (a), the flotation fraction is $f = 0.7$. The maximum crack length increases monotonically with W' or $\Delta\tau'$. As the sticky patch gets larger (increasing W') or stronger (increasing $\Delta\tau'$), its influences extends further into the surrounding ice sheet. This leads to an increase in tensile stress at the downstream end, which in turn promotes fracture propagation. For sticky patches with $W' = 1$, a minimum $\Delta\tau' \approx 0.2$ is required to have a crack with length $Z'_C \sim 0.2$. Panel (b) shows another case where the ice is closer to flotation (i.e., $f = 0.9$). Here, fracture can be propagated by smaller values of W' and $\Delta\tau'$, compared with panel (a). The

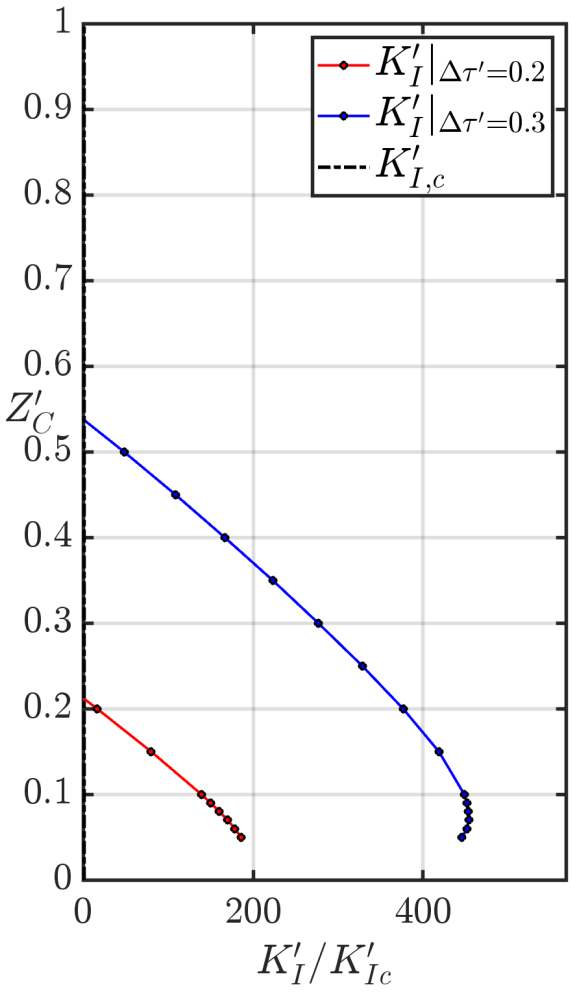

Figure 2.3: Stress intensity factor K_I versus crack length with $W' = 1$. Two cases with different $\Delta\tau'$ are considered: $\Delta\tau' = 0.2$ (red) and $\Delta\tau' = 0.3$ (blue). The vertical axis represents the dimensionless crack length. Horizontal axis represents the dimensionless stress intensity factors normalised by the fracture toughness, $K'_{I,C} = K_{I,C}/\left(\rho_i g H^{3/2}\right)$, where H is chosen to be 100 m. The black dash-dotted line represents the fracture toughness.

sticky patch creates a localised horizontal tension that promotes the growth of the vertical line crack, as shown by the reference case in Figure 2.2. Evidently, this effect is sensitive to the non-dimensional parameters W' and $\Delta\tau'$. When $Z'_C \to 1$, the hydrofracture will penetrate the entire ice thickness. For tidewater glaciers

experiencing sticky patches near their fronts, this could promote calving.

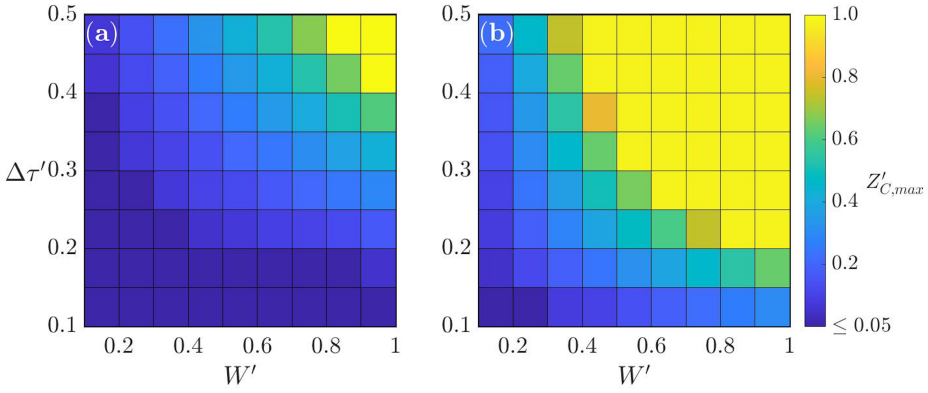

Figure 2.4: Maximum crack length $Z'_{C,max}$ as a function of W' and $\Delta\tau'$. Note that in the criterion, the non-dimensional fracture toughness depends on the ice thickness H. Here we set $H = 100$ m. For larger thicknesses, $K'_{I,C}$ gets smaller, leading to longer cracks. Two cases with different f are considered: **(a)** $f = 0.7$, **(b)** $f = 0.9$. When the crack length $Z'_C = 1$, the crack dissects the full ice-sheet thickness.

2.3.2 Mixed-mode fracture growth

A limitation of the models above is that they assume basal crevasses are mode-I cracks that only propagate vertically and, to simplify the calculation, neglect the mode-II component. This approach is consistent with previous LEFM models of basal crevasses that are pure hydrofractures (Van der Veen, 1998). However, with excess shear stress arising from the sticky patch, basal crevasses are expected to have both mode-I and mode-II contributions. Relaxing our assumption that the crack propagates vertically, we now consider the curved, quasi-static path of fractures using the BEM implementation. Note that for curved fracture paths, we use the G-criterion for fracture growth: the fracture stops when either $G < G_c$ or when there is closure of fracture walls just behind the fracture's tip ($K_I \leq 0$).

For an ice thickness $H = 1000$ m, we impose an initial vertical line crack with length 30m and propagate the crack in its curved trajectories determined by the above criterion. Figure 2.5 shows the mixed-mode fracture paths with different values of dimensionless excess shear stress $\Delta\tau'$ and flotation fraction f. The three panels represent three sizes of the sticky patch: $W' = 0.1$ for panel (a), $W' = 1.0$ for panel (b) and $W' = 10.0$ for panel (c).

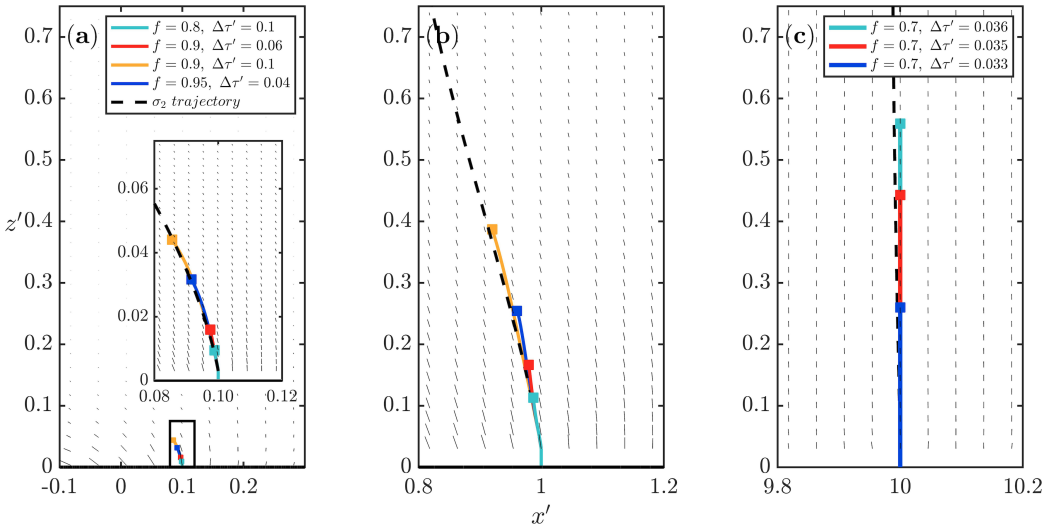

Figure 2.5: Fracture paths calculated under different excess basal shear stress $\Delta\tau'$ and flotation fraction f, with three values of W': **(a)** $W' = 0.1$; **(b)** $W' = 1.0$; **(c)** $W' = 10.0$. An ice thickness $H = 10^3$ m is used to scale the fracture toughness. The background vector field indicates the local direction of the maximum compressive stress, with the vector length scaled by the deviatoric stress $|T_1' - T_2'|$, where T_1' and T_2' are the local principal stresses calculated from $\boldsymbol{T}'$. In panels (a) and (b), the fracture paths (colors) are calculated by BEM, with the principal stress trajectory represented by the dashed curve. Colors represent four different combinations of $\Delta\tau'$ and f as in the legend. In panel (c), since the principal stress trajectory is nearly a vertical line, we no longer conduct the BEM simulation and just assume purely vertical fracture paths. Thus, the maximum crack length is determined as we have done in Figure 2.3. Colors represent three different combinations of $\Delta\tau'$ and f as in the legend.

In panel (a) we consider a sticky patch whose width is one fifth of the ice thickness ($W' = 0.1$). There is a zoom-in plot of the fracture paths in the black box. The

four curves are quasi-static paths with four combinations of flotation fraction f and dimensionless excess shear stress. The paths deviate from the vertical path assumed in models above. In particular, they incline upstream under the influence of the shear stress. Comparing the four curves in panel (a), we find that $\Delta\tau'$ and f have little effect on the direction of the paths.

In panel (b), the length of the panel is kept the same as panel (a). In addition, we keep the same combinations of f and $\Delta\tau'$. With $W' = 1$ (sticky patch width twice the ice thickness; an order of magnitude larger than in panel (a)), the fractures align closer to the vertical and extend further into the ice sheet.

Panel (c) shows the fracture paths when $W' = 10$. In this case the sticky patch is 20 times wider than the ice thickness. The magnitude of the excess shear stress $\Delta\tau'$ required for fracture propagation is reduced to about 0.035. Meanwhile, since $T'_{xx} \gg T'_{zz}$, the principal stress trajectories are nearly vertical lines, as indicated by the background stress field. Thus, fracture paths can be approximated by vertical lines, as we did previously. The crack length becomes very sensitive to the magnitude of $\Delta\tau'$, since a small perturbation to $\Delta\tau'$ (from 0.033 to 0.036) causes a large variation of the crack length.

It is possible to predict the trajectory of the curved cracks without solving the BEM model, using only stresses computed in an uncracked domain. This may be computationally convenient in combination with Stokes-flow models of ice sheets (Krug et al., 2014; Yu et al., 2017). As in the models discussed above, the excess shear stress due to the sticky patch is imposed as a boundary condition on the uncracked domain. We then calculate the perturbation stress in the uncracked domain and plot the principal stress trajectories as the dashed curves in Figure 2.5. We use the perturbation stress due to the excess shear only, because the overburden stress and water pressure are isotropic and do not contribute to the orientation of

the principal stresses. Comparison between these trajectories and the fracture paths predicted by the BEM shows that the former are accurate approximations of fracture paths under the conditions considered here.

If there is no deviatoric stress from sources other than the sticky patch, the magnitude of $\Delta\tau'$ does not contribute to the direction of the fracture path. Instead, the direction of trajectories depends only on the ratio W'. This is consistent with the results predicted by the BEM and indicates that for real basal crevasses affected by sticky patches, the direction of the fracture is predominantly controlled by the relative size of the sticky patch. Since the area of sticky patches can be of the order of 1 km^2 to 100 km^2 (Stokes et al., 2007), we believe the panels in Figure 2.5 are representative cases that reveal the influence of patch size. If sticky patches usually have $W' \gg 1$ in a real ice sheet, then crevasses are mostly vertical and the BEM would not be necessary for future studies.

2.4 Discussion

We have developed and analysed a model of basal crevassing associated with sticky patches at the bed of an elastic glacier or ice sheet. Our model, based on LEFM theory, evaluates the role of shear-stress variations and makes predictions of crack lengths and trajectories. As shown above, the growth of such basal cracks depends on the flotation fraction f, the non-dimensional size of the sticky patch W', and the non-dimensional stress variation $\Delta\tau'$.

2.4.1 Initiation of basal crevasses

When modelling both vertical and curved basal crevasses in the results section, we assumed pre-existing small cracks with $K_I > K_{I,C}$. They are a prerequisite for further fracture propagation. By using a simple Griffith fracture model (Tada

et al., 2000)

$$K_I = K_{I,C} = \sigma_{xx}\sqrt{\pi Z_C}, \tag{2.17}$$

we estimate the minimum crack length Z_C required for growth, given a local effective stress σ_{xx} across the fracture. In the BEM simulations we assumed a 30-m-long initial crack, corresponding to a 10 kPa local stress; this combination guarantees $K_I > K_{I,C}$. If tensile stress reaches 326 kPa, basal fractures might initiate on the boundaries of grains 3 cm in diameter. This large value of stress seems unlikely to be achieved under normal circumstances.

2.4.2 Potential applications to real ice sheets

For real ice sheets, basal shear stress patterns are difficult to observe directly. In several cases, they have been estimated by inversion of surface data under specific assumptions. Sergienko and Hindmarsh (2013) showed that for a region of the Antarctic ice sheet with large ice thickness ($H \approx 10^3$ m), the basal shear stress has rib-like patterns of variation. The width of such sticky patches varies from one ice thicknesses ($W' = 0.5$) to 10 ice thicknesses ($W' = 5$). The excess shear stress (200 to 300 kPa) estimated for these locations is small compared with the overburden pressure ($\Delta\tau' \sim 0.03$). In this case, the effect of the sticky patch depends on its size and local water pressure, as discussed in the Results section. For small patches ($W' < 1$), the excess shear stress $\Delta\tau'$ only affects the extent of fracture propagation, while the patch size W' governs the direction of propagation, as shown in Figure 2.5. Basal crevassing occurs when the flotation fraction f approaches 1, which means the ice sheet becomes nearly afloat. The result is consistent with the conclusions of Van der Veen (1998). For larger patches with $W' \sim 10$, the sticky patch extends 20 ice thicknesses in the flow direction, basal crevasses would initiate on the downstream end at a lower water pressure $f \sim 0.7$.

For alpine glaciers with an ice thickness of order 100 m, variations of basal shear stress have been found to be in the range of 0 to 200 kPa (Brædstrup et al., 2016). In the non-dimensional parameter space, $\Delta\tau'$ is of order 0.1, larger than in Antarctic settings. Moreover, W' is of the order of 1 to 10, which is similar to that of sticky patches in Antarctic ice sheets. Thus, we predict that sticky patches play a more important role in determining the length and direction of basal crevasses in alpine glaciers. For further investigations of the basal hydrofractures around sticky patches, we need to go beyond the inversion results, understand the specific causes of the sticky patches, and include the essential physics in our model.

In natural glaciers and ice sheets, there are many factors that might create sticky patches, including bedrock bumps, till-free areas, well-drained tills and basal freeze-on. All of these would lead to localised, high basal friction (Stokes et al., 2007). An important friction phenomenon is the stick-slip motion of ice, detected in Whillans Ice Stream (WIS) in West Antarctica. Wiens et al. (2008) investigated the WIS stick-slip motion and related it to a sticky patch on the bed. Furthermore, Sergienko et al. (2009) argued that WIS can be considered as a typical stick-slip system controlled by basal friction, where the sticky spot nucleates the stick-slip cycle. Therefore, for sticky spots associated with stick-slip ice motion, we can estimate the stress variation from parameters in relevant friction experiments (McCarthy et al., 2017; Lipovsky et al., 2019; Zoet et al., 2020), rather than from inversion from surface data based on viscous rheology. Assuming that the basal shear stress follows Coulomb's law of friction, we can interpret $\Delta\tau$ in terms of friction coefficient variation $\Delta\mu$, we find that

$$\Delta\tau' = \Delta\mu N', \tag{2.18}$$

where $N' = 1 - f$ is the dimensionless effective normal stress. The basal stress

variation is controlled by both friction coefficient variation $\Delta\mu$ and the flotation fraction f. The magnitude of $\Delta\mu$ during the stick-slip motion of ice can be measured experimentally. By keeping a constant normal stress of $N = 500$ kPa between the ice sample and the bedrock asperity, Zoet et al. (2020) found that the friction-coefficient decrease during stick-slip motion is between 0.1 and 0.4. We assume that the measurements of $\Delta\mu$ also apply to the sticky patch discussed in our model.

Well-drained till could serve as a sticky patch. For a well-drained till surrounded by a water saturated layer (Stokes et al., 2007), the water pressure on the till would be smaller than the surroundings. For such a till, we assume that the excess friction coefficient $\Delta\mu$ is 0.4 and flotation fraction f is 0.7. Then, according to (2.18), the excess basal shear stress is $\Delta\tau' \sim 0.1$, which would lead to a tensile-stress concentration on the downstream end of the patch. Meanwhile, in the surroundings, the local subglacial water pressure is expected to be higher ($f \geq 0.7$). For the case considered above, when f reaches 0.9, basal crevassing is likely to occur.

2.4.3 Thermal implications of basal crevasses

The temperature structure of ice has important effects on ice dynamics. Using high-vertical-resolution sensing, Law et al. (2021) reported spatial heterogeneity of englacial ice temperature and deformation. They found a basal temperate-ice zone with thickness that varies from 5 m to 73 m at two locations separated by only 9 km at Store Glacier, an outlet glacier of the Greenland Ice Sheet. Their study indicates spatially varying basal thermal conditions over distances of a few ice thicknesses. Injection of water-filled basal crevasses can locally modify the thermal profile of the ice sheet (Luckman et al., 2012) and is a potential explanation of the spatially-varying temperate ice layer. The thermal structure of basal crevassing, which is similar to that of dykes in rock (Daniels et al., 2014), has been

modelled in several studies (Jarvis and Clarke, 1974; McDowell et al., 2021). Their approach recognises that water-filled basal crevasses in sub-temperate ice propagate on a short timescale, followed by rapid refreezing of water inside the crack. McDowell et al. (2021) modelled the refreezing of a basal crevasse as an instantaneous heat source in a one-dimensional heat-conduction system, using the analytical solution of Carslaw and Jaeger (1959). We use the same analytical solutions for a two-dimensional thermal structure of a basal crevasse. Details of this calculation are provided in Appendix A.3.

To estimate the heat released by refreezing, we return to the dimensional problem and assume a static, water-filled vertical crack with crack length $Z_C = 50$ m in a 100 m-thick, subtemperate ice sheet. The crack width w is assumed to be 10 cm uniformly along the crack. The water inside the crack instantaneously refreezes at $t = 0$, releasing an amount of heat q_i per unit length per unit depth into the page (i.e., in the direction normal to the crack). The heat is estimated as

$$q_i = \rho_i w L = 3 \times 10^7 \text{ J m}^{-2}, \tag{2.19}$$

where $\rho_i w$ is the mass of water per unit area of the fracture and L is the latent heat of solidification. Mathematically, the refreezing process is assumed to be an instantaneous source at $t = 0$. The temperature rise caused by refreezing, ΔT, is held at 0 K on the surface boundary with the atmosphere, the basal boundary and at the limit of $x \to \pm\infty$. The temperature rise will asymptotically decay to zero after a long cooling process.

Figure 2.6 shows the perturbation in temperature due to the refreezing of water in a single basal crevasse over twenty years. The surrounding ice undergoes a rapid warming at $t = 0$, followed by a long cooling period until the temperature drops back to the background state $\Delta T = 0$ (McDowell et al., 2021). Panel (a) shows

that after 5 years of diffusion, the temperature perturbation due to refreezing is localised around the crevasse and decreases sharply within ± 30 m. Panels (b) and (c) show the temperature perturbation after 10, 15 and 20 years. After 20 years, ΔT drops back below 0.05 K and the system is again close to the background state.

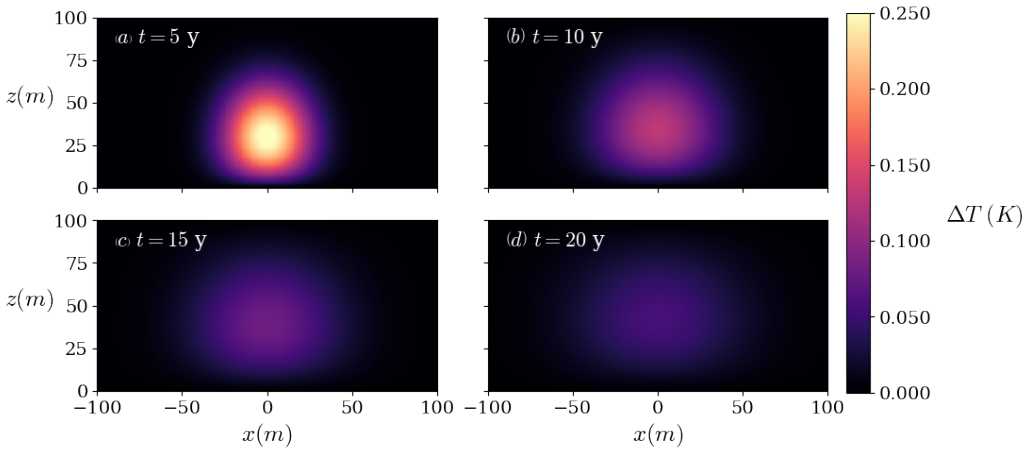

Figure 2.6: Perturbation of a single basal crevasse on background temperature field. The basal crevasse is modeled as a vertical, linear, and instantaneous heat source with a length of 50 m, positioned at the center of the domain. $t = 0$ is the time of crevasse opening and refreezing. **(a)** $t = 5$ years. **(b)** $t = 10$ years. **(c)** $t = 15$ years. **(d)** $t = 20$ years.

If a sticky patch is fixed on the bedrock beneath a sliding ice sheet, the patch could generate a series of basal crevasses, as shown in Figure A.2 (Appendix A.3). Thus, we next consider a case in which the spacing between these crevasses is equal to the half-width of the sticky patch $W = 100$ m. For these equally spaced basal crevasses, the temperature field is a linear superposition of the effect of each crevasse. In the mathematical model, the basal crevasse is initiated on the downstream end of the sticky patch and subsequently advected by sliding. Details are provided in Appendix A.3.

The thermal effect of a series of basal crevasses is shown in Figure 2.7. The down-

stream perturbation will gradually smooth out after decades of cooling. The stable pattern of temperature rise depends on the volume of water inside the crack. The BEM simulations show that the thickness of basal crevasses is of order 0.1 m, which is much smaller than the upper limit of basal crevasse thickness observed by Harper et al. (2010). Here we simply assume that the crack width is 0.1 m. The initial, localised temperature rise will decay rapidly as it smooths out. Refreezing in basal crevasses is a possible factor influencing the temperature profile of basal ice, leading to localised heating around the relic basal crevasses, followed by cooling back toward a steady state (McDowell et al., 2021).

Alternatively, if the basal fracture is embedded in temperate ice and hence doesn't freeze rapidly, it becomes a persistent mechanical perturbation to the ice sheet. A series of such basal crevasses will be carried downstream to the grounding line. If an ice shelf extends seaward from the grounding line, the basal crevasses will weaken the shelf to lateral shear stresses associated with buttressing and vertical shear associated with calving (Bassis and Ma, 2015). The recent numerical model developed by Berg and Bassis (2022) suggests that the advection of crevasses could increase the calving rate and promote glacier retreat.

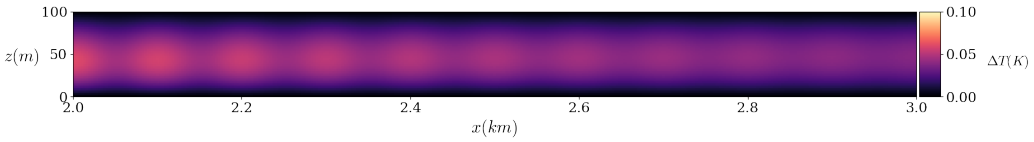

Figure 2.7: Thermal effect of a series of basal crevasses that is 2 km to 3 km downstream from the sticky patch. The basal crevasses occur at the sticky patch one by one at a specific time interval. As time progresses, these crevasses are advected downstream, during which the thermal anomaly created by each crevasse gradually diffuses and smooths out through conduction.

2.4.4 Limitations of the model

The model presented has three significant limitations. First, it is based on equilibrium equations of elasticity. The ice sheet is assumed to be an isotropic, elastic body without any internal viscous deformation that is commonly computed by a Stokes model. Therefore, our model only accounts for the physics of fracturing on a short timescale in which ice is dominated by elastic rheology. This approach might miss important interactions between the sticky patch and viscous deformation that would modify the stress field. Basal crevasses can be deformed by the internal deformation caused by viscous flow. For an ice sheet with a thickness $H = 1000$ m, the velocity difference between the surface and the bed can be up to several kilometers per year, which can significantly deform the basal crevasses whose length are of the same order as the ice thickness. Thus, a viscoelastic rheology is required to study basal crevasses on a longer timescale. Moreover, it is important to include the spatial and temporal variation of subglacial hydrology (Harper et al., 2005; Hewitt, 2013), which is simplified to a static water pressure in the current model.

The second main limitation is that the model does not account for the three-dimensional effects of sticky patches. In a real ice sheet, some sticky patches may have a round shape instead of a long, rib-like pattern. In that case, it is more appropriate to study them in a 3-D domain, which includes both vertical and lateral extension of cracks, rather than as a plane-strain problem in the x–z plane.

The third limitation relates to the fracture toughness. In applying the LEFM approach, we implicitly assume a brittle medium. However, a brittle-to-ductile transition occurs at a critical grain size (Schulson et al., 1984). Regions and layers of coarse-grained ice exist in ice sheets (Gow et al., 1997). Thus, in some glaciers and ice sheets there may exist ductile ice that eludes brittle fracture. This het-

erogeneity would modify the predicted crack lengths. Furthermore, Sinha (1978) argued that the Young's modulus of ice E depends on temperature, even on a short loading timescale. Further investigation is therefore required to determine whether the thermal profile is important for ice elasticity and fracture.

A more complete understanding of how basal crevasses grow and interact with viscous flow will require a three-dimensional, viscoelastic model including variations in fracture toughness.

2.5 Conclusion

Besides basal water pressure (Van der Veen, 1998), stress variations of sticky patches at the ice–bed interface can promote the propagation of basal crevasses. In previous studies, basal crevasses were assumed to be mode-I hydrofractures under pure horizontal tension (Van der Veen, 1998; Krug et al., 2014; Jimenez and Duddu, 2018). Assuming water pressure smaller than the flotation condition, we examined the effect of sticky patches on basal crevassing in a grounded glacier or ice sheet. We found that sticky patches can provide stress required for crack extension. Alongside the flotation fraction, such sticky-patch-assisted crevassing depends on two non-dimensional parameters: (1) the ratio W' of the sticky-patch half-width to the ice thickness, and (2) the ratio $\Delta\tau'$ of excess shear stress to the basal ice overburden pressure.

With a sufficient variation of basal shear stress, the direction of basal fracture is controlled by the relative size of the sticky patch. When the width of the sticky patch is much larger than the ice thickness, basal crevasses grow nearly vertically and are essentially mode-I fractures. When the width of the sticky patch is smaller than the ice thickness, however, curved basal crevasses grow with trajectories inclined upstream, which could explain the inclined relic basal crevasses in Wearing

and Kingslake (2019). In this case, principal stresses can be used to approximate crack trajectories.

For real glaciers or ice sheets with complicated geometries, our model can be combined with the basal stress pattern to investigate how stress variation promotes basal crevassing. Compared to stress estimates from inversion calculations (Sergienko and Hindmarsh, 2013; Brædstrup et al., 2016), qualitative analysis shows that for a flotation fraction of about 0.9, the basal-stress pattern in alpine glaciers and ice sheets may play an important role in determining the growth of basal crevasses. To better understand the basal crevasses controlled by sticky patches, future research could incorporate viscous ice flow, spatially resolved subglacial hydrology, and detailed fracturing properties of ice.

3 | Viscoelastic mechanics of tidally induced lake drainage in the Amery grounding zone

Statement of Authorship for joint/multi-authored papers for PGR thesis

To appear at the end of each thesis chapter submitted as an article/paper

The statement shall describe the candidate's and co-authors' independent research contributions in the thesis publications. For each publication there should exist a complete statement that is to be filled out and signed by the candidate and supervisor **(only required where there isn't already a statement of contribution within the paper itself).**

Title of Paper	Viscoelastic mechanics of tidally induced lake drainage in the Amery grounding zone
Publication Status	□Published □ Accepted for Publication √□Submitted for Publication □Unpublished and unsubmitted work written in a manuscript style
Publication Details	Hanwen Zhang, Richard F. Katz, and Laura A. Stevens. Viscoelastic mechanics of tidally induced lake drainage in the Amery grounding zone, 2024. URL https://arxiv.org/abs/2311.01249.

Student Confirmation

Student Name:	Hanwen Zhang		
Contribution to the Paper	The research idea arose from a discussion with my supervisors on a newly published work. I did the literature review, set up the mathematical model, performed the numerical simulations and wrote the manuscript.		
Signature	Hanwen Zhang	Date	08/07/2024

Supervisor Confirmation

By signing the Statement of Authorship, you are certifying that the candidate made a substantial contribution to the publication, and that the description described above is accurate.

Supervisor name and title:	Professor Richard F Katz	
Supervisor comments I confirm what Hanwen has written above is true. I certify that the candidate made a substantial contribution to the publication, and that the description described above is accurate.		
Signature	Date	08/07/24

This completed form should be included in the thesis, at the end of the relevant chapter.

This work is under review by *The Cryosphere*. Above is the statement of authorship.

3.1 Introduction

Supraglacial lakes are ephemeral meltwater ponds formed by surface melting, and have important influences on the mass balance of nearby ice shelves. In addition to lowering the albedo and increasing the surface melting (Tedesco et al., 2012; Leeson et al., 2015), the lakes can drain through hydrofractures, leading to accelerated ice flow (Stevens et al., 2022) or ice shelf collapses (Banwell et al., 2013). In East Antarctica, supraglacial lakes often cluster in the grounding zone (Stokes et al., 2019), where the lake drainage could be modulated by tidal flexure occurring in the grounding zone. Therefore, understanding the causes of lake drainage in these regions requires insight into how tidal flexure is induced and how it contributes to hydrofracturing that facilitates lake drainage.

Ice-shelf flexure at the grounding line can be modelled using thin-plate theory with an elastic (Vaughan, 1995; Sayag and Worster, 2011; Wagner et al., 2016; Warburton et al., 2020) or a viscoelastic constitutive relationship (Reeh et al., 2003; Gudmundsson, 2007). In these models, the GL is treated as a peeling front or as the clamped end of the ice shelf. Thin-plate models capture the large-scale flexure of ice shelves, and neglect the membrane stress that is governed by sliding.

Various studies have used a vertically integrated theory with a viscous rheology to investigate the dependence of steady-state grounding-line position on ice thickness, sliding laws, buttressing effects and bed topography (Schoof, 2007a,b; Katz and Worster, 2010; Schoof, 2012; Tsai et al., 2015; Pegler, 2018; Haseloff and Sergienko, 2022; Sergienko and Haseloff, 2023). Besides depth-integrated models, full-Stokes models have also been used to study the migration of ground-

ing lines on both longer timescales (Nowicki and Wingham, 2008; Durand et al., 2009; Favier et al., 2012; Gudmundsson et al., 2012; Cheng et al., 2020) and tidal timescales (Gudmundsson, 2011; Rosier et al., 2014, 2015; Rosier and Gudmundsson, 2020). In these models, the ice-sheet–bed contact problem has been implemented as boundary conditions. A more recent development by Stubblefield et al. (2021) and de Diego et al. (2022) has incorporated the contact boundary conditions into variational inequalities. This formulation enabled the representation of the contact condition within a variational framework that was implemented in the Finite Element method. In this study, we adopt the framework by Stubblefield et al. (2021) to study the tidal effects on GL dynamics of the Amery Ice Shelf.

For a Maxwell viscoelastic ice shelf subject to external tidal forcings, the shelf initially responds elastically, followed by viscous creep that relaxes the initial deformation. The Maxwell time represents the characteristic timescale over which the ice transitions from behaving elastically to viscously. Since the semi-diurnal tidal period at the Amery Ice Shelf (approximately 12 hours) is close to the Maxwell time of ice (approximately 9 hours in our estimation), we use a viscoelastic constitutive relationship to model the tidal flexure. In particular, we extend the framework for a marine ice sheet with viscous ice flow by Stubblefield et al. (2021) to an upper-convected Maxwell model to capture the stress and GL migration induced by tides. We predict the tensile stress at the GL for daily maximum tidal amplitudes. Then, using Linear Elastic Fracture Mechanics (LEFM) analysis, we estimate the contributions from tidal stress and lake-water supply to quasi-static hydrofracturing. This enables us to derive a relationship of tidal amplitude and lake-water depth for tidally-induced supraglacial lake drainage, which we compare to the lake-drainage time series presented by Trusel et al. (2022). Based on the model results, the relationship predicts tidally-induced lake drainage with tidal amplitude and lake water depth. The results support the hypothesis that at the

Amery Ice Shelf GL, supraglacial lake drainage is controlled by both lake depth and tidal amplitude. Moreover, this new model-based relationship enhances our understanding of the role ocean tides play in driving lake drainage through tidal flexure.

In this paper, we begin by analyzing remotely-sensed ice flow data near the selected lake, which informs the setup of the viscoelastic model. We then combine the model results with a LEFM model to explore hydrofracture propagation with tidal flexure. Finally, we discuss the model's sensitivity to variations in ice rheology and bedrock geometry.

3.2 Method

We first present an estimation of the local strain-rate and stress fields near the lake studied by Trusel et al. (2022). Our estimation indicates the lake region is extension-dominated with negligible shear stress. The background stress is insufficient to produce hydrofracturing, indicating the importance of tidal stress. Therefore, we extend the marine ice-sheet model with viscous ice rheology (Stubblefield et al., 2021) by incorporating a viscoelastic rheological formulation. We introduce the model set-up and how we predict lake drainage events.

3.2.1 Observed strain rate in the vicinity of the lake

Figure 3.1(a) shows the ice-surface velocity field $\boldsymbol{v}$ from the MEaSUREs InSAR-Based Antarctica Ice Velocity Map (Rignot et al., 2011b, 2017; Mouginot et al., 2012, 2017) near the lake, according to which we calculate the streamlines and the strain rate $\dot{\varepsilon}$ (Fig. 3.1b). The lake is located on the grounding line extracted from MEaSUREs Antarctic Grounding Line from Differential Satellite Radar Interferometry, Version 2 (Rignot et al., 2016a, 2011a, 2014; Li et al., 2015). Following

Wearing (2017), we denote the direction of velocity $\hat{\boldsymbol{v}}$, and the transverse direction $\hat{\boldsymbol{t}}$. The along-flow strain rate can be defined as

$$\dot{\varepsilon}_p = \hat{\boldsymbol{v}} \cdot \dot{\boldsymbol{\varepsilon}} \cdot \hat{\boldsymbol{v}}, \tag{3.1}$$

and the transverse strain rate as

$$\dot{\varepsilon}_t = \hat{\boldsymbol{v}} \cdot \dot{\boldsymbol{\varepsilon}} \cdot \hat{\boldsymbol{t}}. \tag{3.2}$$

Figure 3.1(c,d) shows $\dot{\varepsilon}_p$ and $\dot{\varepsilon}_t$ near the lake. We are particularly interested in $\dot{\varepsilon}_p$ and $\dot{\varepsilon}_t$ along the streamline that crosses the lake. Assuming that the z-components of ice deviatoric stress $\boldsymbol{\tau}$ are zero on the surface ($\tau_{xz} = \tau_{yz} = \tau_{zz} = 0$), we calculate the viscosity η using Glen's flow law (Glen, 1955). The deviatoric stress along (τ_p) and transverse (τ_t) to the streamline are $\tau_p = 2\eta\dot{\varepsilon}_p,\ \tau_t = 2\eta\dot{\varepsilon}_t$, as shown in Fig. 3.1(f). The magnitude of τ_t and τ_p are less than 40 kPa along the streamline. Specifically, at the lake, there is negligible background shear stress and an extensional stress with a magnitude of about 30 kPa in the flow direction. Therefore, for simplicity, we neglect the background stresses, focus on the streamline and adopt a 2-D flow line model that accounts for tidally induced extension along the flow direction.

We use BedMachine Antarctica v2 to obtain the basal topography and ice geometry along the streamline (Fig. 3.1e) (Morlighem et al., 2017, 2020). The surface gradient is relatively uniform upstream of the GL. The subglacial cavities downstream of the grounding zone are more than 20 m wide. Thus, we assume that the ice shelf downstream of the GL doesn't contact the bedrock, and the water pressure on the ice–ocean interface is hydrostatic. In the computation, we use a linear bedrock topography (Fig. 3.1e) with a slope angle extracted from reality.

This simplification enables us to further explore the sensitivity of GL dynamics to bedslope angle. In Appendix A.5 we present a set of model results with real bed topography for comparison. While the magnitude of tidal stress is modified quantitatively in the real-bed-topography case, tidal stress remains the main contribution to the extension on the GL, compared with the background extensional and shear stress.

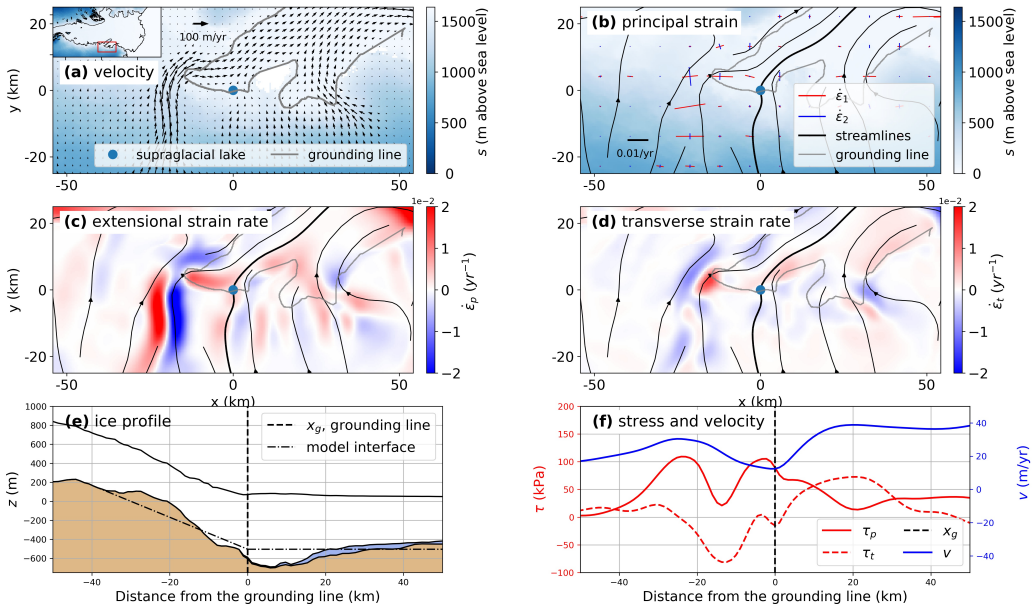

Figure 3.1: Ice surface velocity, strain rate and stress in the region of the supraglacial lake. **(a)** Velocity field near the grounding line (grey), where the supraglacial lake is denoted with the blue dot. Here the maximum velocity of the largest arrow in this figure is 20 m yr^{-1}. The color represents the ice-sheet surface elevation above sea level. The map inset on the top left corner shows the full Amery Ice Shelf topography, with the plotted region outlined with a red box; **(b)** principal strain rate and streamlines. The streamline that crosses the lake is marked with the bold line; **(c)** along-flow strain rate with positive values represent extension and negative values represent compression; **(d)** transverse strain rate; **(e)** local ice-sheet geometry and bed topography; **(f)** For the streamline that crosses the lake, along-flow deviatoric extension τ_p (solid red line) and shear stress τ_t (dashed red line), and speed v (blue). Note that $x = x_g = 0$ is the position of the supraglacial lake as well as the grounding line.

3.2.2 Lake basin bathymetry

For the drainage events reported in Trusel et al. (2022), we calculate lake-basin depth from a water-free, 2-m WorldView-1 DEM, with the data given by Trusel et al. (2022). We set the elevation of the flat basin, excluding craters and hydrofractures, as the deepest point of the lake. With this, the lake, located at 70.59 °S, 72.53 °E, has a depth of about 10 m and a width of about 1 km in the direction normal to the GL. Using a shoreline-extraction method (Moussavi et al., 2016; Trusel et al., 2022), water depth is calculated as the difference between the median shoreline elevation and the lake-basin elevation.

3.2.3 Model domain

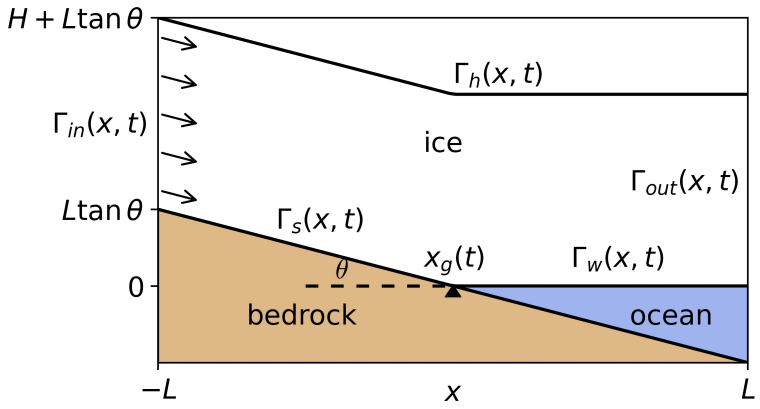

Figure 3.2: Schematic showing the model domain of a marine ice sheet system.

Figure 3.2 shows a schematic of the computational domain. We consider a segment of marine ice sheet with length $2L$ and thickness $H(x,t)$ in a Cartesian coordinate system with position vector $\boldsymbol{x} = (x,z)$, where z increases upward. The inflow and outflow boundaries are denoted Γ_{in} and Γ_{out}. The top surface is denoted Γ_h. The bottom is divided into two parts, according to whether the ice is in contact with the bedrock or the ocean. The ice–bedrock interface Γ_s is where

ice is in contact with the bedrock at a height $b\,(x)$. As a simplification, we assume that the bedrock has a uniform slope θ. The ice–ocean interface Γ_w is where ice is detached from the bedrock. The two boundaries Γ_s and Γ_w meet at the GL whose horizontal position, denoted $x_g\,(t)$, migrates with time t. The origin of the coordinate system is set at the middle of the domain on the ice–bedrock interface (at the position of the GL shown in the schematic).

Following Stubblefield et al. (2021), we first construct the mesh with piecewise linear bottom profile $s\,(x)$ and surface profile $h\,(x)$

$$s\,(x) = \max\left(b\,(x)\,, 0\right), \tag{3.3}$$

$$h\,(x) = s\,(x) + H, \tag{3.4}$$

which are shown in Fig. 3.2. We evolve this initial profile with no tides until the ice-flow geometry (i.e., $s\,(x)$, $h\,(x)$ and GL x_g) reaches a steady state. In practice, the ice flow reaches the steady state when the grounding line reaches its steady position, when the migration can not be resolved with the 25-m grid size. This provides a steady profile of the marine ice sheet for use as an initial condition for simulations with tides.

3.2.4 Governing equations

The governing equations for momentum and mass conservation are

$$\boldsymbol{\nabla} \cdot \boldsymbol{\sigma} + \rho_i \boldsymbol{g} = \mathbf{0}, \tag{3.5}$$

$$\boldsymbol{\nabla} \cdot \boldsymbol{u} = 0, \tag{3.6}$$

where $\boldsymbol{\sigma}$ is the total Cauchy stress tensor, ρ_i is ice density, $\boldsymbol{g}$ is gravity, and $\boldsymbol{u}$ is the ice velocity field. The $\cdot$ here represents dot product of tensors. The stress $\boldsymbol{\sigma}$

can be decomposed as an isotropic part and deviatoric part, $\boldsymbol{\sigma} = -p\boldsymbol{I} + \boldsymbol{\tau}$, where p and $\boldsymbol{\tau}$ represent the pressure and deviatoric stress, respectively. Here $\boldsymbol{I}$ is the unit tensor.

To model viscoelasticity, we adopt the upper-convected Maxwell formulation for the deviatoric stress $\boldsymbol{\tau}$. The constitutive relationship is

$$\boldsymbol{\tau} + \lambda \overset{\nabla}{\boldsymbol{\tau}} = 2\eta\dot{\boldsymbol{\varepsilon}}, \tag{3.7}$$

where the Maxwell time, $\lambda = \eta/\mu$, is the ratio of ice viscosity η to shear modulus μ. The strain rate is denoted $\dot{\boldsymbol{\varepsilon}}$. The upper-convected time derivative (Oldroyd rate) $\overset{\nabla}{\boldsymbol{\tau}}$ measures the temporal variation of $\boldsymbol{\tau}$ including the effect of rigid body rotation,

$$\overset{\nabla}{\boldsymbol{\tau}} = \partial_t\boldsymbol{\tau} + \boldsymbol{u}\cdot\nabla\boldsymbol{\tau} - (\nabla\boldsymbol{u})^T\cdot\boldsymbol{\tau} - \boldsymbol{\tau}\cdot\nabla\boldsymbol{u}, \tag{3.8}$$

where $(\cdot)^T$ represents tensor transpose.

We assume a constant shear modulus μ and non-Newtonian viscosity η that is governed by Glen's flow law with regularisation

$$\eta = \frac{1}{2}B\left(|\dot{\boldsymbol{\varepsilon}}|^2 + \delta_\nu\right)^{-(n-1)/2n}, \tag{3.9}$$

where $B = 2^{(n-1)/2n}A_0^{-1/n}$ is determined by the two flow law parameters A_0 and n, and $|\dot{\boldsymbol{\varepsilon}}| = \sqrt{\dot{\boldsymbol{\varepsilon}} : \dot{\boldsymbol{\varepsilon}}}$ is the Frobenius norm of the strain rate. The regularisation with the numerical parameter δ_ν is used to prevent infinite viscosity at vanishing strain rate (Jouvet and Rappaz, 2011; Helanow and Ahlkrona, 2018; Stubblefield et al., 2021). The value of δ_ν sets an upper limit on the viscosity and, therefore, also on the Maxwell time. In our reference parameter set, used below, $\eta \leq 4.3 \times 10^{13}$ Pa s and $\lambda \leq 40$ hr. For $\delta_\nu = 0$, Eq. 3.9 reduces to the classical form of Glen's flow law.

3.2.5 Boundary conditions

Neglecting atmospheric pressure and other surface loading, the top boundary is assumed to be stress-free. Its elevation h is governed by the kinematic condition

$$\frac{\partial h}{\partial t}(x,t) = \left[\left(\frac{\partial h}{\partial x}\right)^2 + 1\right]^{1/2} \boldsymbol{u}\cdot\boldsymbol{n} \qquad \text{on } \Gamma_h, \tag{3.10}$$

where $\boldsymbol{n}$ is the outward-pointing unit normal vector and Γ_h is the top boundary.

On the inflow boundary Γ_{in}, we impose a uniform horizontal inflow rate u_0 and zero shear stress

$$\begin{cases} \boldsymbol{u}\cdot\boldsymbol{n} = u_0, \\ \boldsymbol{t}\cdot\boldsymbol{\sigma}\cdot\boldsymbol{n} = 0, \end{cases} \qquad \text{on } \Gamma_{in}, \tag{3.11}$$

where $\boldsymbol{t}$ is the tangential unit vector. The inflow velocity u_0 is set to be the satellite-derived surface velocity, 17 m y^{-1} (Rignot et al., 2016b). On the outflow boundary, we impose the ice-overburden pressure

$$\boldsymbol{\sigma}\cdot\boldsymbol{n} = -\rho_i g\,(h-z)\,\boldsymbol{n}, \qquad \text{on } \Gamma_{out}, \tag{3.12}$$

which means that at the downstream boundary Γ_{out}, the ice shelf floats at hydrostatic equilibrium, without bending stress.

Similar to Eq. 3.10, the bottom profile $s\,(x,t)$ is governed by the kinematic equation

$$\frac{\partial s}{\partial t}(x,t) = -\left[\left(\frac{\partial s}{\partial x}\right)^2 + 1\right]^{1/2} \boldsymbol{u}\cdot\boldsymbol{n}, \qquad \text{on } \Gamma_w, \tag{3.13}$$

where Γ_w is the ice–ocean interface. The stress on the bottom boundary depends on the local contact condition. To introduce the boundary conditions related to the contact problem, we consider hydrostatic water pressure p_w on the ice–ocean

interface, defined as

$$p_w = \rho_w g \left[h_w \left(t \right) - s^* \right], \qquad \text{on } \Gamma_w, \tag{3.14}$$

where ρ_w is water density, g is gravitational acceleration, h_w is the sea level and s^* is the approximated bottom boundary that will be introduced in Sect. 3.2.6. The atmospheric pressure is neglected at the ice–ocean interface, as it is generally small compared to the hydrostatic pressure.

The sea level h_w is a superposition of a steady state h_0 and a sinusoidal function of time, representing ocean tides with amplitude A and frequency f,

$$h_w \left(t \right) = h_0 + A \sin \left(2 \pi f t \right). \tag{3.15}$$

On the ice–ocean interface, the hydrostatic pressure p_w is imposed as the traction

$$\boldsymbol{\sigma} \cdot \boldsymbol{n} = -p_w \boldsymbol{n}, \qquad \text{on } \Gamma_w. \tag{3.16}$$

On the ice–bedrock interface, ice can be either attached or detached from the bed. In the normal direction, the contact condition is established by the following boundary conditions

$$\begin{cases} \sigma_n \geq p_w, \\ u_n \leq 0, \\ \left(\sigma_n - p_w \right) u_n = 0, \end{cases} \qquad \text{on } \Gamma_s, \tag{3.17}$$

where σ_n is the normal component of traction. Here the water pressure p_w follows Eq. 3.14. When $u_n = 0$, ice is attached to the bed, $\sigma_n \geq p_w$. When $u_n < 0$, ice is detached from the bed, thus $\sigma_n = p_w$. The impenetrability is implemented

using a penalty term shown in Sect. 3.2.6, originally proposed by Stubblefield et al. (2021).

In the tangential direction, ice sliding is resisted by friction that is governed by a Weertman-type sliding law (Weertman, 1957)

$$\boldsymbol{t}\cdot\boldsymbol{\sigma}\cdot\boldsymbol{n} = -C\left[(\boldsymbol{u}\cdot\boldsymbol{t})^2+\delta_s\right]^{-\frac{n-1}{2n}}\boldsymbol{u}\cdot\boldsymbol{t} \qquad \text{on } \Gamma_s, \tag{3.18}$$

where C is the friction coefficient, δ_s is a numerical factor preventing singularity and n is the exponent in Glen's flow law Eq. 3.9. In the computation, we choose C such that the surface velocity at the GL matches the inflow speed u_0. This choice gives a relatively low surface velocity gradient, which agrees with satellite observations at the lake region (Rignot et al., 2016b).

3.2.6 Numerical Implementation

When implementing the hydrostatic water pressure on the ice–ocean interface, for numerical stability, rather than the bottom elevation from the previous time step, s^* is an approximation to the current step elevation (Durand et al., 2009; Stubblefield et al., 2021), defined as

$$s_*(x,t) = s(x,t-\Delta t) - u_n(x,s,t)\Delta t, \tag{3.19}$$

where Δt is the numerical time step, $s(x,t-\Delta t)$ is the bottom profile at the previous time step, and u_n is the normal velocity on the bottom boundary ($u_n > 0$ accounts for downward motion).

In the variational formulation, on the ice–bed interface, the contact condition Eq. 3.17 is accounted for by adding the hydrostatic pressure Eq. 3.16 , along with

a line integral as a penalty term

$$\frac{1}{\varepsilon}\int_{\Gamma_s}\frac{1}{2}\left(\boldsymbol{u}\cdot\boldsymbol{n}+|\boldsymbol{u}\cdot\boldsymbol{n}|\right)\boldsymbol{v}\cdot\boldsymbol{n}\,\mathrm{d}s, \tag{3.20}$$

where ε is the penalty parameter and $\boldsymbol{v}$ is the test function corresponding to the velocity field $\boldsymbol{u}$. The penalty term Eq. 3.20 becomes nonzero only when $u_n > 0$ and thus penalises penetration. For the viscous contact problem, when $\varepsilon \to 0$, the solution to the variational formulation weakly converges to the solution governed by the contact condition Eq. 3.17 (Kikuchi and Oden, 1988). Although for the viscoelastic, the variational formulation cannot be directly cast as a minimization problem, as $\varepsilon \to 0$, it is still a good approximation to the solution governed by the contact condition.

The variational formulation is implemented using the finite-element library FEniCS (Logg and Wells, 2010; Logg et al., 2012; Langtangen and Logg, 2017). A mixed finite element is used to solve for a combined field $(\boldsymbol{u},\ p,\ \boldsymbol{\tau})$. We use triangular elements in which the pressure varies linearly and the velocity and deviatoric stress vary quadratically. In A.4, we report convergence tests showing the results are mesh-independent and, in the limit of no elastic deformation ($\mu \to \infty$), converge to the viscous solutions by Stubblefield et al. (2021). For further details about the variational formulation and its numerical implementation, the reader is referred to Stubblefield et al. (2021).

3.3 Results

First, we show a reference case representing the tidal response of the marine ice sheet near the lake reported in Trusel et al. (2022). The lake, whose depth (≤ 10 m) is much smaller than the ice thickness (≈ 500 m) at the location, is assumed

Table 3.1: Parameters used in the model and their reference values.

Physical property	Notation	Value
Density of water	ρ_w	1027 kg m^{-3}
Density of ice	ρ_i	917 kg m^{-3}
Length of the domain	L	20 km
Ice thickness	H	500 m
Bedslope angle	θ	0.02
Glen's Law exponent	n	3
Viscosity coefficient	A_0	3.1689×10^{-24} Pa^{-n} s^{-1}
Characteristic (inflow) velocity	u_0	9 m y^{-1}
Friction coefficient	C	1.0×10^{7} Pa$^{1/n}$ m^{-1}
Shear modulus	μ	0.30×10^{9} Pa
Viscosity regularisation parameter	δ_ν	10^{-18} s^{-2}
Friction regularisation parameter	δ_s	10^{-15} m^{2}s^{-2}
Penalty parameter	ε	10^{-13}
Tidal amplitude	A	1 m

to have no effects on ice dynamics and thus is not included here. We consider a 20-km long section of a 500-m thick ice sheet sliding on bedrock with constant bedslope angle $\theta = 0.02$ that represents the characteristic bedslope angle upstream of the lake, as shown by the dash-dotted line in Fig. 3.1(e). The ice thickness and bedslope angle, representing the local topography, are adopted from Morlighem et al. (2017). Initially, the grounded ice sheet and floating ice shelf both cover 10 km of the domain. In the model of elasticity, we use Young's modulus $E = 0.88$ GPa and Poisson's ratio $\nu = 0.41$, as suggested by Vaughan (1995) for tidal flexure problems. A list of of parameters and their references values is provided in Table 3.1. The tidal amplitude $A = 1$m is a characteristic local tidal amplitude calculated from the CATS2008 (Circum-Antarctic Tidal Simulation) model (Howard et al., 2019).

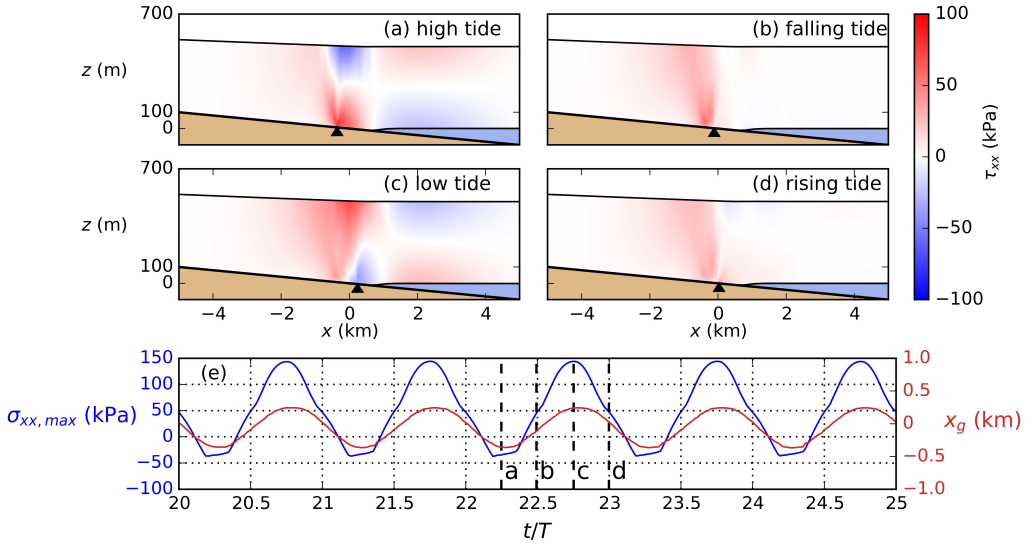

Figure 3.3: Tidal response of a marine ice sheet at different tidal phases. **(a)–(d)** Deviatoric stress τ_{xx} in one tidal period, with red colour indicating tensile stress and blue colour indicating compressive stress. The black triangle marks the position of the grounding line. **(e)** The maximum tensile stress $\sigma_{xx,max}$ (blue) on the top boundary within the lake region ($\bar{x_g} - 0.5$ km $\leq x \leq \bar{x_g} + 0.5$ km) and the GL position x_g (red) versus time (scaled by the tidal period T) with positive values representing downstream migration. Vertical dashed lines show the time of panels (a)-(d).

3.3.1 Tidally-induced grounding line migration and related stress

We find tidally-modulated GL migration and corresponding change in stress. The GL position x_g is shown in Fig. 3.3e. Whereas Stubblefield et al. (2021) find double GLs at low tides with a relatively small bedslope angle $\theta = 2.5 \times 10^{-4}$ (Stubblefield et al., 2021), in our model we find only a single GL migrating in phase with the tides. This migration results in a 600-m wide grounding zone, which is larger than estimated from hydrostatic equilibrium assuming a uniform ice thickness ($2A/\theta = 100$ m).

To demonstrate tidal flexure, we plot the deviatoric stress component τ_{xx} at four tidal phases (Fig. 3.3a–d). The ice undergoes upward and downward flexure at

high and low tides, respectively. At high tide (Fig. 3.3a), the stress is concentrated close to the GL, with compression near the top and tension near the bottom, closely downstream of the GL. This resembles the stress pattern of a thin plate (Timoshenko, 1955), indicating a region where the ice vertical velocity transitions from the ice-sheet flow to the ice-shelf oscillation with tides. Further downstream at the floating shelf, the stress is predominantly hydrostatic without bending, as indicated by the boundary condition Eq. 3.12. At low tide (Fig. 3.3c), the tensile stress dominates the ice-sheet top surface near the GL. The region experiencing tensile stress is larger and located further upstream. At rising tides (Fig. 3.3b) and falling tides (Fig. 3.3d), τ_{xx} is tensile at the GL, but the magnitude is smaller than τ_{xx} at low tide.

The full horizontal stress σ_{xx} is considered for hydrofracturing at the lake. Assuming that the lake covers the ice-sheet surface within $|x - \overline{x}_g| \leq 0.5$ km, where $\overline{x}_g$ is the time-averaged GL position in a tidal period, we calculate the maximum σ_{xx} on the ice-sheet surface within the lake region for any given time, which is denoted $\sigma_{xx,max}$. The temporal variation of $\sigma_{xx,max}$ is shown in Fig. 3.3e. In each tidal period, $\sigma_{xx,max}$ reaches its peak at low tide, corresponding to the downward flexural stress in Fig. 3.3c.

The reference case gives the tidal stress at tidal amplitude $A = 1$ m. We further consider cases with a series of tidal amplitude from 0 to 1 m, and thus obtain a stress–amplitude relationship for sinusoidal semi-diurnal tides, which is referred to as the "σ–A relationship" from this point forward. Specifically, it's the relationship between $\sigma_{xx,max}$, the maximum tensile stress in the lake region within one tidal period and the tidal amplitude A, assuming that the sea level variation due to tides follows a sinusoidal function over time. However, with solar tides, tidal amplitude is modulated in a two-week cycle. Given the viscoelastic rheology with its history-dependence, such an amplitude modulation might complicate

the σ–A relationship from monochromatic tides.

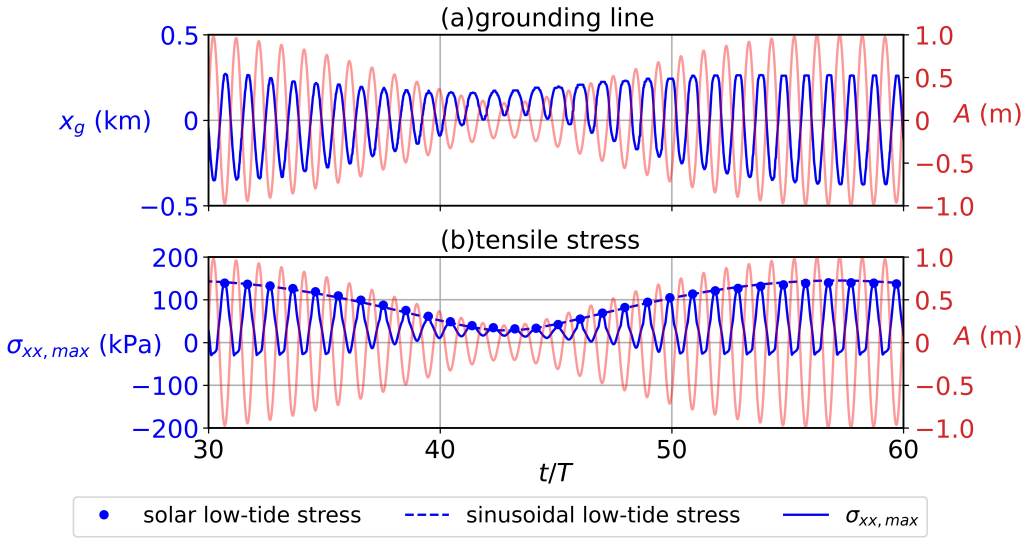

Figure 3.4: **(a)** Modulated tidal amplitude (red) and corresponding GL migration (blue). The horizontal axis is time scaled by the tidal period. **(b)** (blue) Maximum deviatoric tensile stress $\sigma_{xx,max}$ on the ice-sheet surface within the lake region with modulated tidal amplitude. The dots denote the low-tide stress in one tidal period. The dashed blue line is the estimated low-tide stress calculated from the modulated tidal amplitude using σ–A relationship from sinusoidal semi-diurnal tides in Sect. 3.3.1.

To explore the σ–A relationship with solar tides, we replace the sinusoidal tides in Eq. 3.15 with a modulated sine wave over a 14-day period, with sea-level variation shown in Fig. 3.4. Applying this forcing to the reference case, the GL migrates in phase with tides (Fig. 3.4a). In each tidal period the low-tide $\sigma_{xx,max}$ tracks the σ–A relationship for sinusoidal tides (Fig. 3.4b), indicating that solar tidal amplitude modulation does not change the σ–A relationship. Therefore, daily maximum tidal amplitude proves to be a good metric to estimate the daily maximum tidal stress that contributes to hydrofracturing.

3.3.2 Linear Elastic Fracture Mechanics model of the hydrofracture

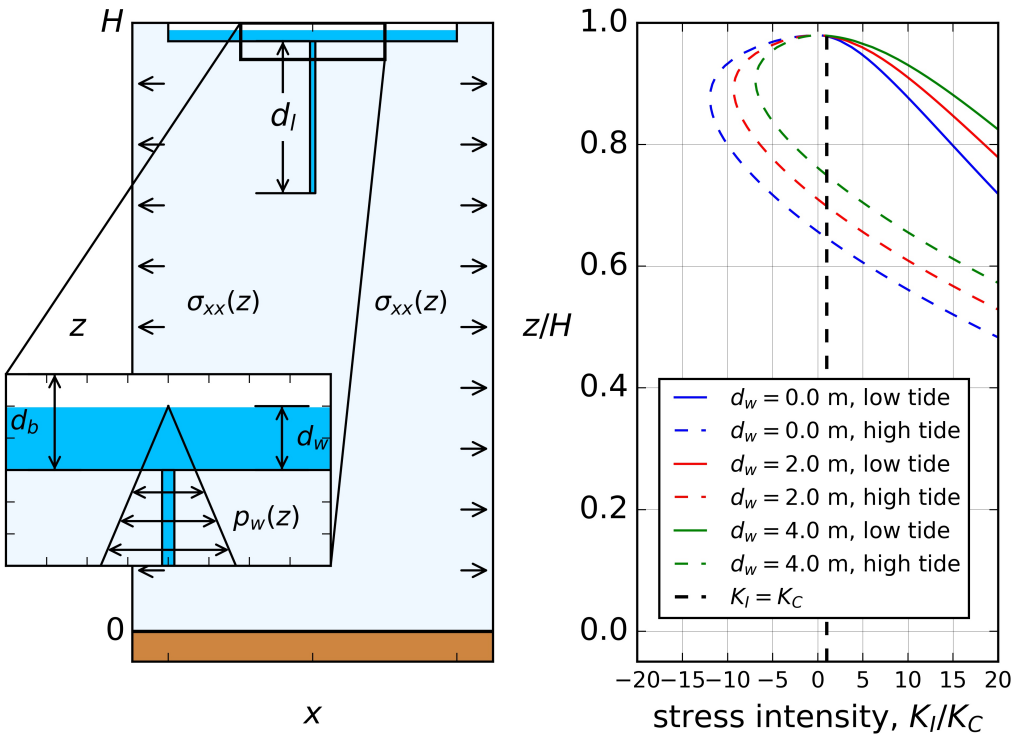

Figure 3.5: **(a)** The LEFM model of the hydrofracture. The lake basin with depth d_b, is filled with water to a depth d_w. Here d_w serves as a measurement of the water pressure p_w, as shown in the zoom-in window. Promoted by the tidal stress $\sigma_{xx}(z)$ and lake-water pressure p_w, a vertical fracture with length d_l is initiated from the lake bottom. **(b)** A reference case showing K_I/K_C varying with depth (scaled by the ice thickness) and tidal phases, with $A = 1.0$ m, $d_b = 10$ m, and $d_{l,init} = 0.1$ m. The solid lines represent K_I/K_C at low tides. The dashed lines represent K_I/K_C at high tides when upward flexure causes compression, and thus a negative tidal contribution to hydrofracture.

Since hydrofracturing typically occurs on a short timescale over which ice behaves elastically, we consider the fracture propagation in the LEFM framework. The hydrofracture is assumed to be a quasi-static elastic fracture occurring at the location with $\sigma_{xx,max}$ at low tides. The stress that drives its propagation is the sum of the

water pressure and tidal stress. The water pressure in the fracture p_w is assumed to be hydrostatic; the tidal stress $\sigma_{xx,max}$ is calculated by the viscoelastic model mentioned above. We use the weight-function method to calculate the stress intensity factor K_I (Tada et al., 2000). Since at low tides the GL goes downstream and leaves the ice beneath the lake attached to the bedrock, we use a weight function that is designed for ice grounded on rigid bedrock, as suggested by Jimenez and Duddu (2018).

Figure 3.5a shows a schematic of the fracture model. The lake basin has a depth $d_b = 10$ m (obtained from the DEM) and is filled with water to a depth d_w. The horizontal stress $\sigma_{xx}(z)$ represents the low-tide tidal stress, and is obtained from the numerical results with a given tidal amplitude A. For a vertical fracture, we can calculate the stress intensity factor K_I as a function of its length d_l. If K_I exceeds the ice fracture toughness K_C, the fracture can propagate, until $K_I = K_C$. We assume that lake drainage occurs when a vertical hydrofracture reaches the ice-sheet bottom.

Note that for the initial fracture, K_I is sensitive to its length $d_{l,init}$. However, there is little observational constraint on the lengths of pre-existing fractures at the lake basin. While the choice of $d_{l,init}$ requires further study, the relative importance of the lake pressure versus the tidal amplitude is independent of $d_{l,init}$, which is shown in the model-based relationship below. Here we will choose $d_{l,init}$ such that the modelled relationship best fits the drainage data.

In Fig. 3.5b, assuming that $A = 1$ m, we plot a reference case showing K_I/K_C versus the fracture length d_l, under different combinations of lake depth d_w ($d_w = 0,\ 2,\ 4$ m) and tidal phases (low tide and high tide). The vertical dashed line represents the ice fracture toughness K_C. At low tide, downward flexure gives positive K_I near the upper surface. Conversely, at high tides, compression gives

negative K_I there. Figure 3.5b can be used to predict lake drainage: at low tides, for a pre-existing fracture with length $d_{l,init}$, if $K_I > K_C$ holds for any depth that the fracture can reach, then A and d_w are predicted to induce lake drainage. Repeating this treatment for different combinations of A and d_w yields the model-based drainage relationship, which is shown in Sect. 3.3.3.

3.3.3 Drainage criteria in terms of tidal amplitude and lake depth

As shown above, at low tides for an initial fracture with a given length $d_{l,init} = 0.1$ m, the prediction of hydrofracturing is controlled by two factors: tidal stress and water pressure, measured by tidal amplitude A and lake depth d_w. When the combined effect of tidal flexure and lake-water pressure can overcome the ice fracture toughness and ice-overburden stress, the fracture propagates, reaches the ice–bedrock interface, and drains the lake.

We construct a model-based drainage relationship in terms of A and d_w in a 2-D parameter space. The relationship is defined as the marginal conditions at which the initial fracture can reach the ice–bedrock interface. In Fig. 3.6a, we show two criteria with different initial crack lengths $d_{l,init}$ of 0.1 and 0.2 m. When (A, d_w) of a lake crosses the critical line from bottom-left to top-right, the total tensile stress is large enough that the hydrofracture can reach the bottom of the ice sheet. As shown in Fig. 3.6a, the increasing tidal amplitude can reduce the lake depth required for hydrofracturing. This provides a measure of the relative importance of tidal flexure to water pressure for lake drainage. Meanwhile, there exists a maximum tidal amplitude above which fracturing can be induced entirely by tidal stress, without a water supply. Supraglacial lakes would not be able to form under such large tidal stress.

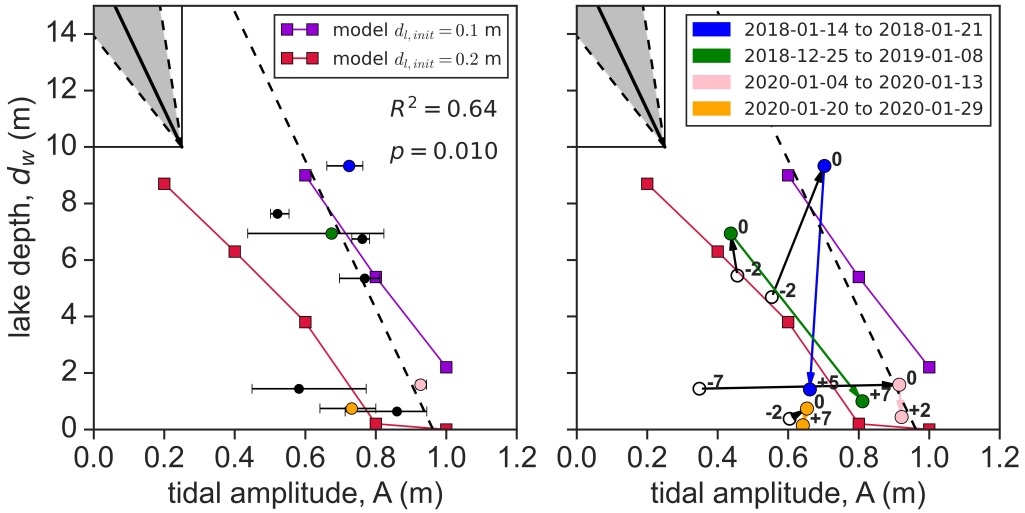

Figure 3.6: **(a)** A comparison between the model relationship and the drainage data. Each circle represents one drainage event from Trusel et al. (2022). The horizontal coordinate is the time-averaged daily maximum tidal amplitude during the drainage, with an error bar representing the range of the daily maximum tidal amplitude. The vertical coordinate is the pre-drainage lake depth. The dashed black line is a weighted linear regression of the observations. The red and violet lines are model-based criteria with different initial crack lengths, with squares representing the numerical experiments. The four coloured circles represent drainage events with best-constrained temporal evolution of lake depth and tidal amplitude. The 95% confidence interval on the regression slope is shown by the grey area on the top left corner, with the solid line indicating the regression result, and the dashed lines showing the upper and lower limit. **(b)** Temporal evolution of coloured events in panel (a). The points labelled "0" represent the day of the drainage. The negative and positive values represent the days before and after the drainage, respectively.

In Fig. 3.6a, we compare the model-based relationship with observations from Trusel et al. (2022). Each circle represents a drainage event. To leading order, the model agrees with the data. The data cluster close to the model-based relationship for realistic values of $d_{l,init}$. A weighted linear regression of the observations also suggests that higher tidal amplitude reduces the lake depth required for drainage. However, the steeper slope of the regression line suggests the dependence of drainage on tidal amplitude is stronger than predicted by our model.

To better demonstrate the drainage process, in Fig. 3.6b we show four events with the best observational constraint on temporal evolution of lake depth and tidal amplitude. We show measurements from before, during and after the drainage. Note that we simply assume the drainage occurs at the highest water level observed, which is the minimum pre-drainage water level due to the time interval between satellite images. The two events dated 2018-12-25 and 2020-01-04 cross the critical line with $d_{l,init} = 0.2$ m in the observational interval of several days. The event dated 2018-01-14 crosses both criteria. The post-drainage states are below the critical line with $d_{l,init} = 0.1$ m, representing the end of drainage due to insufficient water supply. Therefore, we believe our model captures the essential physics that controls hydrofracturing in the grounding zone.

3.4 Discussion

We use a viscoelastic model to predict GL migration and tidal stress of a marine ice sheet. By considering tidally-induced hydrofracturing in an LEFM model, we construct a model-based drainage relationship that accounts for the tidal amplitude and lake depth required for drainage. The relationship agrees with observations to leading order, thus supporting the hypothesis from Trusel et al. (2022) that "*hydrofracture is assisted by tidally forced ice flexure inherent to the ice shelf grounding zone*." Furthermore, the relationship suggests that, in grounding zones, ocean tides might set a maximum volume for supraglacial lakes. We hypothesise that lakes tend to remain at a smaller volume than this critical value due to regular drainage events. This hypothesis could be tested by a statistical study of more supraglacial lake drainage events with local ocean tides.

The tidal-flexure model and drainage relationship can be applied to other marine ice sheets with different rheological properties and bed topography. In the follow-

ing, we perform a sensitivity analysis to explore the dependence of GL migration and tidal stress on ice rheology and bedslope angle. Finally, we discuss the limitations of our model by exploring missing factors that might affect GL dynamics and hydrofracture.

3.4.1 Sensitivity to ice Maxwell time

The ice Maxwell time λ controls the viscoelastic tidal response of a marine ice sheet. Depending on the Deborah number De, the ratio of λ to the tidal period T, the tidal response can be dominated by either elasticity ($De \ll 1$) or viscosity ($De \gg 1$). Here, we explore the tidal response with a varying τ, representing a transition from viscoelastic to viscous rheology.

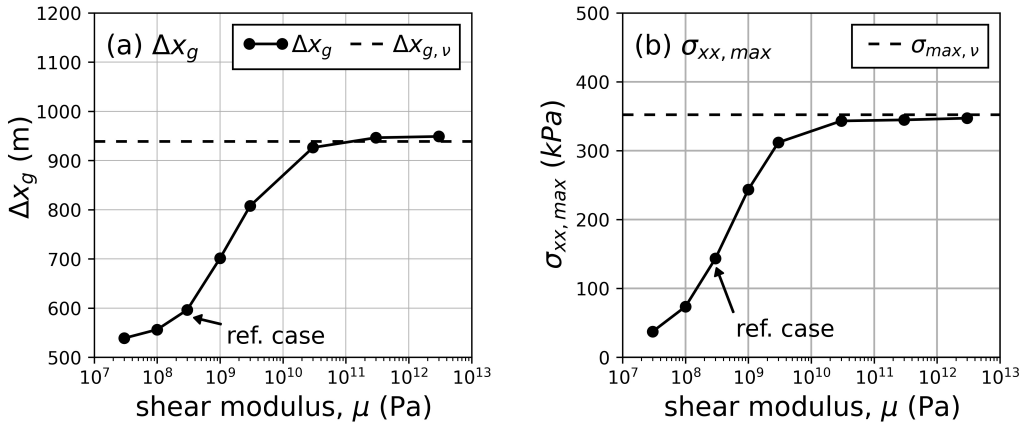

Figure 3.7: **(a)** The grounding-zone width Δx_g (solid line), defined as $\Delta x_g = \max\{x_r\} - \min\{x_l\}$ as a function of shear modulus $\mu = 3 \times 10^7$ to 3×10^{12} Pa, with x_l and x_r denote the left and right GL, respectively. Here for both the viscous case and the viscoelastic case, $x_l = x_r$. The dashed line shows $\Delta x_{g,\nu}$, the grounding-zone width in the viscous limit ($\mu \to \infty$). **(b)** Maximum tensile stress $\sigma_{xx,max}$ versus μ. The numerical reference case in Sect. 3.3 is labelled.

With the viscosity governed by Glen's Flow law, we consider cases with varying shear modulus μ, thus varying Maxwell time. All other parameters are set to their

reference values. We define a grounding-zone width, Δx_g, as the range of GL in a tidal period. In Fig. 3.7a, Δx_g is plotted versus μ. With the bedslope $\theta = 2\times10^{-2}$, only one GL is found to migrate with the tides, giving a grounding-zone width of about $0.5 - 1$ km. As $\mu \to \infty$, the tidal response becomes purely viscous and the grounding zone widens and reaches its viscous limit $\Delta x_{g,\nu}$. In Fig. 3.7b, $\sigma_{xx,max}$ increases with increasing μ and converges to the viscous stress calculated by the viscous model (Stubblefield et al., 2021).

The ice Maxwell time is crucial in determining GL migration and tidal stress, because viscous rheology tends to increase the width of a grounding zone and produce larger tensile stress than viscoelastic rheology. Therefore, our model indicates the importance of using viscoelastic rheology with an accurate ice Maxwell time to predict the magnitude of tidal stress. Given the dependence of Δx_g on μ (Fig. 3.7a), it may be possible to infer ice mechanical properties from observations on the range of GL migration.

3.4.2 Sensitivity to bedslope angle

The above discussion shows how tidal response varies with shear modulus, with a characteristic bedslope $\theta = 2 \times 10^{-2}$ at the Amery Ice Shelf GL. Here we extend the results to different bedslopes and explore how the tidal response of a GL would change with local bathymetry. We consider three marine ice sheets with bedslope $\theta = 2 \times 10^{-4}$, 2×10^{-3}, and 2×10^{-2}, with all other parameters set to be the same as the reference case. For simplification, we focus on the effect of θ while keeping the inflow velocity u_0 and basal friction coefficient C in Eq. 3.18 fixed. Because of this, the ice adjusts to the changing bedslope through either thinning or thickening. The modelled surface velocity near the grounding line deviates from the observed value u_0, but maintains the same order of magnitude. The GL migration is shown in Fig. 3.8a. Different from the single GL shown

above, the low-bedslope regime $\theta = 2 \times 10^{-4}$ is characterized by double grounding lines at low tides. Between the left GL at x_l and the right GL at x_r, the ice sheet is lifted due to a water layer trapped underneath (Stubblefield et al., 2021), forming a "low-tide grounding zone." For the other two cases, only a single GL is found, with the range of the GL decreasing with increasing θ. Moreover, the maximum tidal stress monotonically increases with θ (Fig. 3.8b). This is consistent with thin-plate models. As the bed slope angle increases, the curvature at the grounding line also increases, resulting in greater flexural stress. Simultaneously, the gravitational body force resisting grounding-line migration becomes stronger, causing the width of the grounding zone to decrease. However, the dependence is no longer linear in this viscoelastic model. For a specific grounding line, the local basal topography and characteristic bedslope angle can be constrained by observations (Fretwell et al., 2013). Thus, the uncertainties of the modelled tidal GL migration and stress mainly come from the rheological model.

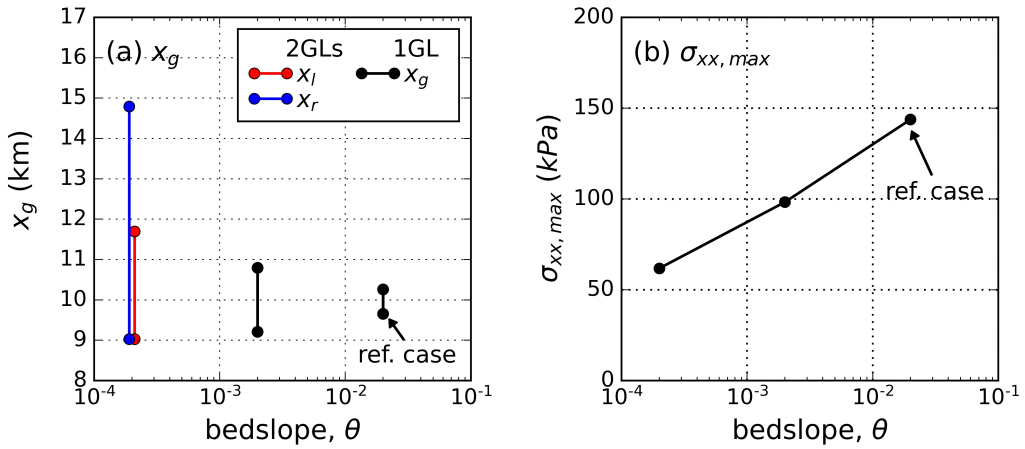

Figure 3.8: **(a)** The range of the GL position in one tidal period as a function of bedslope angle $\theta = 2 \times 10^{-4}$, 2×10^{-3}, 2×10^{-2}. When $\theta = 2 \times 10^{-4}$, there are two GLs. The left and right GLs are denoted x_l and x_r, respectively. The other two cases give single GL x_g shown by the black line. **(b)** Maximum tidal stress $\sigma_{xx,max}$ versus θ.

Our sensitivity analysis is based on the assumption of a fixed basal friction parameter. To estimate the tidal stress at a specific geographical location, the tidal response should be modelled with a basal sliding law that matches observed surface velocities. Then, a drainage relationship can be set up to estimate the local tidal contribution to supraglacial lake drainage.

3.4.3 Limitations

Deviations between the model-based relationship and data regression indicate that we may be underestimating the tidal contribution to hydrofracturing (Fig. 3.6). Currently, we assume a stress-free top surface and constant ice properties in the viscoelastic flow model. However, the supraglacial lake can induce additional stress in the surrounding ice, particularly on floating portions of the grounding zone that allow downward flexure (MacAyeal and Sergienko, 2013). Meanwhile, the existence of ice fatigue due to stress oscillations can weaken ice strength and promote hydrofracturing (Borstad et al., 2012; Lhermitte et al., 2020). A better approach may be to directly consider the supraglacial lake and the ice damage within the 2-D viscoelastic model.

Another limitation arises from our assumption of hydrostatic water pressure on the ice–ocean interface. The pressure gradient induced by tidally modulated subglacial water flow can cause elastic flexure in ice sheets close to the grounding line (Warburton et al., 2020). Furthermore, ocean tides can change the effective pressure at the bed and lubricate the ice–bedrock interface, leading to a variation of basal friction that is not accounted for by the sliding law in our model (Gudmundsson, 2011). Thus, it is important to incorporate the subglacial hydrology in simulating the tidal response of a marine ice sheet.

Limitations also come from the data availability. Relative to the tidal period and

lake-drainage period, the lower temporal resolution of the remotely sensed observations might obscure the true lake depth and tidal amplitude at the time of drainage. Field measurements and satellite images of supraglacial lake drainage with a higher observational frequency could improve our understanding of tidally-induced drainage.

3.5 Conclusion

Our study of tidally-induced stress and hydrofracture propagation in a viscoelastic marine ice sheet grounding zone supports the hypothesis on tidally-induced supraglacial lake drainage proposed by Trusel et al. (2022). We further propose a model-based relationship for lake drainage that indicates how ocean tides and lake depth together determine whether supraglacial lakes will drain via hydrofracture at the Amery Ice Shelf GL. Importantly, the relationship indicates that grounding-zone lakes tend to remain at a smaller volume than a critical value controlled by tidal flexure. For similar, tidally-modulated marine ice sheets, our results suggest that ocean tides can generate significant stress near the grounding line, potentially increasing the vulnerability of ice sheets to hydrofracturing in grounding zones where lakes form. Our work serves as an initial attempt to analyse the tidal effect on hydrofracturing, which helps to better explain the role of ocean tides in driving supraglacial lake drainage.

4 | Tides modulate ice-shelf and ice-stream velocity through asymmetric grounding line migration

4.1 Introduction

An ice stream is a region of fast-flowing ice within the surrounding grounded ice sheet. For Antarctica Ice Sheet, more than 90% of the discharge happens through outlet glaciers and ice streams. Thus, understanding the controlling mechanics is important for our understanding of the mass balance of Antarctic Ice Sheet. In this chapter, we focus on the responses of Antarctic ice streams to ocean tides on a diurnal or fortnightly timescale.

The tidal response of Antarctic ice streams can be classified depending on their linearity with respect to tidal forcings. In ice streams such as Whillans Ice Stream (Bindschadler et al., 2003) and the Bindschadler Ice Stream (Anandakrishnan et al., 2003) flowing into the Ross Ice Shelf, ice velocity varies at the same frequency as ocean tides, indicating a linear response to tidal forcings. Conversely, some other glaciers and ice streams exhibit tidal variations at a fortnightly frequency that is absent in tidal forcings. For example, the Rutford Ice Stream into the Filchner–Ronne Ice Shelf shows a predominantly fortnightly tidal response to semi-diurnal tidal forcings (Gudmundsson, 2006; Minchew et al., 2017). The Beardmore Glacier flowing into the Ross Ice Shelf (Marsh et al., 2013) also shows a fortnightly tidal variation in velocity but with a much smaller magnitude compared to the Rutford Ice Stream. On the Priestley Glacier, which is a highly buttressed valley glacier flowing into the Nansen Ice Shelf, the velocity responds

semi-diurnally to diurnal tidal forcings (Drews et al., 2021). On these ice streams and glaciers, these tidal signals can propagate up to 80 kilometres upstream of the grounding line (Gudmundsson, 2006), or persist within less than 20 kilometres upstream (Heinert and Riedel, 2007; Marsh et al., 2013; Drews et al., 2021), depending on the tidal amplitude. Due to their variability across regions, tidal responses serve as an ideal entry point to investigate the competing mechanisms that control the dynamics of Antarctic grounding zones. As a result, the tidal responses of Antarctic ice streams are garnering increasing attention from ice sheet modellers.

With the fortnightly variation dominating the tidal response, the Rutford Ice Stream is an ideal place to explore the mechanisms causing nonlinear tidal responses. Gudmundsson (2006) observed the tidal response of the Rutford Ice Stream using GPS measurements. This was followed by a series of numerical simulations investigating the potential causes, such as basal sliding law, subglacial hydrology and tidal flexure (Gudmundsson, 2007, 2011; Rosier et al., 2014, 2015). Minchew et al. (2017) developed a Bayesian method to infer surface velocity data from remote-sensing and synthetic-aperture-radar observations. They proposed that at the Rutford Ice Stream, periodic grounding of the ice shelf along the ice-shelf margins causes migration of shear margins and changes in the effective width of the ice shelf. The nonlinear dependence of horizontal ice velocity on the effective width is responsible for the nonlinear tidal responses. Robel et al. (2017) studied this hypothesis using a viscoelastic ice-shelf model with parameterised nonlinear dependence of ice-shelf buttressing stress on tidal height. They have shown that the asymmetry in buttressing stress to tidal height could cause fortnightly variations in horizontal displacement. Recently, Rosier and Gudmundsson (2020) conducted a 3-D full-Stokes simulation of the entire Filchner-Ronne Ice Shelf and highlighted the importance of asymmetric grounding-line migration with respect

to tidal forcings in producing the fortnightly tidal response.

Besides periodic grounding, asymmetric grounding-line migration can also occur through tidally modulated subglacial hydrology. By modelling the coupled dynamics of an elastic ice shelf with the subglacial water discharge, Warburton et al. (2020) showed that seawater can be retained in the subglacial cavity at low tides, causing detachment of basal ice from the bed and lubricating the ice–bed interface. This process can be nonlinear with tidal height, depending on the permeability of the subglacial hydrological system and tidal frequency. Their model produced asymmetric grounding line migration with respect to tidal height. However, the flow variability was not considered due to the limit of elastic ice rheology. On the other hand, MacAyeal et al. (2021) developed an ice-stream flow-line model that incorporates both viscoelastic vertical flexure and viscous horizontal flow, which could be further extended to modelling tidally-modulated grounding line dynamics. In this chapter, I combine the subglacial hydrology model by Warburton et al. (2020) with the ice-stream model by MacAyeal et al. (2021).

By applying the combined model to an idealised, Rutford-like ice stream, we predict tidal variations in ice velocity with a given tidal height. The model serves as an intermediate state between complex 3-D regional-scale models (Rosier and Gudmundsson, 2020) and simple 1-D elastic ice-shelf bending models, and is aimed at acquiring mechanistic understanding of the tidal response due to asymmetric grounding-line migration caused by subglacial hydrology and viscoelastic tidal flexure.

4.2 Governing equations and model set-up

For the dynamics of ice, we adapt the modelling framework by MacAyeal et al. (2021), in which ice motion is assumed to be a superposition of viscoelastic ver-

tical flexure and viscous horizontal flow. While the model by MacAyeal et al. (2021) is focused on the dynamics of ice shelves, we add the effect of subglacial hydrology by introducing a water layer between ice and bed, which gives us flexibility to model the grounded ice and migration of the grounding line. Fig. 4.1 shows a schematic of the model domain. The Cartesian coordinate is (x, z), with the origin $\mathcal{O}$ on the bedrock. The bottom and top of the ice shelf are represented by $B(x, t)$ and $S(x, t)$, respectively. The thickness is $H(x, t) = S - B$. The length of the domain is denoted as L. For simplicity, we use the vertical coordinate $\zeta = z - (B + H/2)$, with $\zeta = 0$ on the mid-plane in the ice.

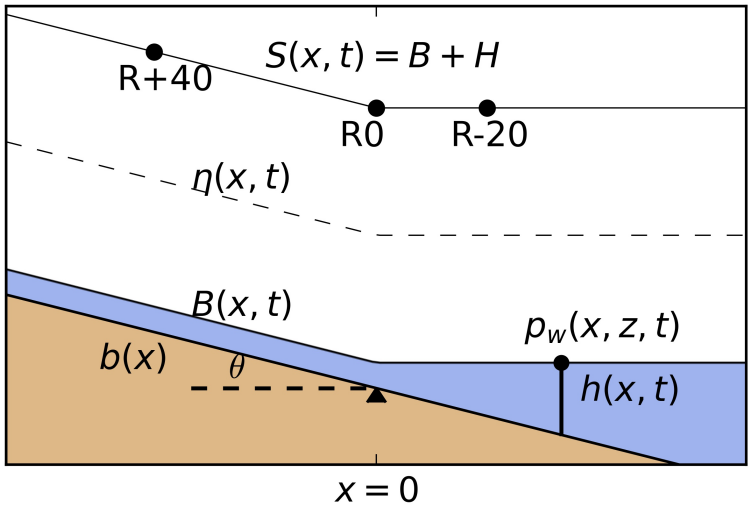

Figure 4.1: Model set-up. Here R+40 represents the GPS station 40 km upstream of the grounding-line station R0, and R-20 is the station 20 km downstream of the grounding line (Gudmundsson, 2007). Time series will be extracted from these three stations to study the tidal responses.

Ice motion is described by the horizontal velocity u and vertical deflection η. The rheology of the vertical flexure is assumed to be viscoelastic and governed by the Maxwell constitutive law. Thus, the net vertical displacement η is the sum of the elastic component $\eta_e(x, t)$ and viscous component $\eta_\nu(x, t)$.

The horizontal velocity u is assumed to be the superposition of vertically uniform stretching $\overline{u}$, flexure $-\frac{\partial^2 \dot{\eta}_\nu}{\partial x^2}\zeta$ (linear in ζ), and higher order terms in terms of the aspect ratio $\varepsilon = \dfrac{H}{L}$,

$$u = u\left(x, \zeta, t\right) = \overline{u}\left(x, t\right) - \frac{\partial \dot{\eta}_\nu}{\partial x}\zeta + \mathcal{O}\left(\varepsilon^2\right). \tag{4.1}$$

The overline is used to denote variables that are depth-averaged and thus independent of ζ.

4.2.1 Combined viscoelastic flexure and ice flow

The vertical stress balance related to flexure is

$$\frac{\partial^2 M}{\partial x^2} + f = 0, \tag{4.2}$$

where M is the bending moment and f is the distributed force. The bending moment M is associated with the elastic deflection η_e according to the thin-plate theory (e.g., Turcotte and Schubert, 2002)

$$M = -E' I \frac{\partial^2 \eta_e}{\partial x^2}, \tag{4.3}$$

where $E' = \dfrac{E}{1-\mu^2}$ is the effective Young's modulus for plane strain, μ is the Poisson's ratio, and $I = \dfrac{H^3}{12}$ is the second moment of area of the cross section. For simplicity, we drop the prime on E' and denote the effective Young's modulus as E. In the following, we derive the expression of M in terms of the viscous deflection η_ν to construct the constitutive law of viscoelastic bending.

We denote the stress tensor as $\boldsymbol{\sigma} = \boldsymbol{T} - p\boldsymbol{I}$, where $\boldsymbol{T}$ is the deviatoric stress, and p is the cryostatic pressure. Ice viscosity is denoted by ν. According to Eq. 4.1,

dropping the higher order terms $\mathcal{O}(\varepsilon^2)$, the horizontal net stress is

$$\sigma_{xx} = -p + 2\nu\frac{\partial u}{\partial x} = -p + 2\nu\left(\frac{\partial \overline{u}}{\partial x} - \frac{\partial^2 \dot{\eta_\nu}}{\partial x^2}\zeta\right). \tag{4.4}$$

Therefore, the bending moment M can be written as

$$M = \int_{-\frac{H}{2}}^{\frac{H}{2}} (T_{xx} - p)\,\zeta \mathrm{d}\zeta = \int_{-\frac{H}{2}}^{\frac{H}{2}} \left[-p + 2\nu\left(\frac{\partial \overline{u}}{\partial x} - \frac{\partial^2 \dot{\eta_\nu}}{\partial x^2}\zeta\right)\right]\zeta \mathrm{d}\zeta. \tag{4.5}$$

To get M in terms of u and η_ν, we need to derive an expression for p. The stress balance in the vertical direction gives

$$\frac{\partial}{\partial \zeta}(T_{zz} - p) + \frac{\partial}{\partial x}(T_{xz}) = \rho_i g, \tag{4.6}$$

where ρ_i and g are ice density and gravitational acceleration, respectively. The normal vertical deviatoric stress component is $T_{zz} = 2\nu\frac{\partial w}{\partial \zeta}$. We assume that the stream slides over an soft bed, thus shear deformation is negligible compared with horizontal stretching. Therefore, the vertical shear stress T_{xz} is negligible, thus $\frac{\partial}{\partial x}T_{xz} \ll \frac{\partial}{\partial \zeta}(T_{zz} - p)$, and Eq. 4.6 can be simplified to

$$\frac{\partial}{\partial \zeta}\left(2\nu\frac{\partial w}{\partial \zeta}\right) - \frac{\partial p}{\partial \zeta} - \rho_i g = 0. \tag{4.7}$$

Assuming that ice is incompressible, the continuity condition gives that

$$\frac{\partial w}{\partial \zeta} = -\frac{\partial u}{\partial x} = -\frac{\partial \overline{u}}{\partial x} + \frac{\partial^2 \dot{\eta_\nu}}{\partial x^2}\zeta, \tag{4.8}$$

which can be substituted into Eq. 4.7 to get

$$-\frac{\partial}{\partial \zeta}\left(2\nu\frac{\partial \overline{u}}{\partial x}\right) + \frac{\partial}{\partial \zeta}\left(2\nu\zeta\frac{\partial^2 \dot{\eta_\nu}}{\partial x^2}\right) - \frac{\partial p}{\partial \zeta} - \rho_i g = 0. \tag{4.9}$$

Assuming that the top surface is traction free, thus

$$\sigma_{zz} = (-p + T_{zz}) \mid_{\zeta=\frac{H}{2}} = -p|_{\zeta=\frac{H}{2}} + 2\nu \left(-\frac{\partial \overline{u}}{\partial x} + \frac{\partial^2 \dot{\eta}_\nu}{\partial x^2} \zeta \right) \mid_{\zeta=\frac{H}{2}}. \tag{4.10}$$

Integrating Eq. 4.9 from ζ to the top surface $\zeta = \frac{H}{2}$, and substituting Eq. 4.10, we obtain the expression of ice overburden pressure

$$p(\zeta) = -2\nu \frac{\partial \overline{u}}{\partial x} + 2\nu\zeta \frac{\partial^2 \dot{\eta}_v}{\partial x^2} + \rho_i g \left(\frac{H}{2} - \zeta \right). \tag{4.11}$$

Here the viscosity can be decomposed as $\nu = \overline{\nu}(x) + \mathcal{S}(x, \zeta)$, where $\overline{\nu}(x)$ is the depth-averaged component and $\mathcal{S}(x, \zeta)$ represents the depth-dependent component. Thus the depth-averaged pressure is

$$\overline{p}(\zeta) = -2\overline{\nu} \frac{\partial \overline{u}}{\partial x} + 2\overline{\zeta \mathcal{S}} \frac{\partial^2 \dot{\eta}_v}{\partial x^2} + \rho_i g \frac{H}{2}. \tag{4.12}$$

Similarly, $\overline{T}_{xx}$ can be derived as

$$\overline{T}_{xx} = \overline{2 \left(\overline{\nu} + \mathcal{S} \left(x, \zeta \right) \right) \left(\frac{\partial \overline{u}}{\partial x} - \frac{\partial^2 \dot{\eta}_\nu}{\partial x^2} \zeta \right)} = 2\overline{\nu} \frac{\partial \overline{u}}{\partial x} - 2 \left(\overline{\zeta \mathcal{S}} \right) \frac{\partial^2 \dot{\eta}_\nu}{\partial x^2}. \tag{4.13}$$

In our calculation, we assume a constant ice viscosity ($\nu = \overline{\nu} = \nu_0$, $\mathcal{S} = 0$) for simplicity. Substituting Eq. 4.11 into Eq. 4.5 gives the bending moment M in terms of the viscous deflection η_ν,

$$M = -\frac{\overline{\nu} H^3}{3} \frac{\partial^2 \dot{\eta}_v}{\partial x^2} + \frac{\rho_i g H^3}{12}. \tag{4.14}$$

The last term $\frac{\rho_i g H^3}{12}$ is a consequence of ice overburden pressure that is not involved in the constitutive relationship. We will treat it as a forcing term in the force balance equation Eq. 4.19. Combining Eq. 4.3 and Eq. 4.14 gives the vis-

coelastic constitutive law of flexure

$$\frac{\partial^2 \dot{\eta}}{\partial x^2} = \frac{\partial^2 \dot{\eta}_e}{\partial x^2} + \frac{\partial^2 \dot{\eta}_\nu}{\partial x^2} = -\frac{\dot{M}}{EI} - \frac{3}{\overline{\nu} H^3} M. \tag{4.15}$$

We follow MacAyeal et al. (2021) by introducing a new variable $\Phi = \frac{\partial^2 \eta_\nu}{\partial x^2}$ to denote the viscous curvature. Thus

$$\dot{\Phi} = \frac{\partial \Phi}{\partial t} + u \frac{\partial \Phi}{\partial x} = -\frac{3}{\overline{\nu} H^3} M. \tag{4.16}$$

The constitutive law for Maxwell viscoelasticity Eq. 4.15 can be rewritten by replacing the $-\frac{3}{\overline{\nu} H^3} M$ term with $\dot{\Phi}$:

$$\frac{D}{Dt}\left(\Phi - \frac{12\,(1-\mu^2)}{E H^3} M - \frac{\partial^2 \eta}{\partial x^2}\right) = 0. \tag{4.17}$$

Integrating Eq. 4.17 over t gives the constitutive law in terms of Φ

$$\Phi - \frac{12\,(1-\mu^2)}{E H^3} M - \frac{\partial^2 \eta}{\partial x^2} = 0. \tag{4.18}$$

In the stress balance equation Eq. 4.2, the distributed force f depends on the gravity and surface loadings. In the model, we assume that

$$f = p_w + N - \rho_i g H, \tag{4.19}$$

where p_w is the subglacial water pressure, N is the effective pressure applied on the bottom, and $-\rho_i g H$ is the weight of ice. There should be another term $-\frac{\partial^2}{\partial x^2}\left(\frac{\rho_i g H^3}{12}\right)$ related to the gravity term in Eq. 4.14. However, assuming that the x-derivatives of H are small, this term can be neglected from Eq. 4.19. More details about the thickness profile will be provided in Sect. 4.2.4.

The effective pressure N is defined as the pressure imposed vertically by the ice stream on its bed. Note that if there is no flexure in ice, $f = 0$, thus Eq. 4.19 is simplified to $N = \rho_i g H - p_w$, which is the typical definition of N. In Sect. 4.2.3 we will derive p_w and N as a part of the subglacial hydrology model adapted from Warburton et al. (2020).

4.2.2 Shelfy stream approximation

In the above section, we derive the vertical stress balance Eq. 4.19 and constitutive relationship Eq. 4.15 for the viscoelastic flexure problem. In the horizontal direction, the ice stream is accounted for by the shelfy stream approximation (MacAyeal, 1989). A more detailed derivation can be found in MacAyeal et al. (2021).

The stress balance in x gives

$$\frac{\partial}{\partial x}\left(T_{xx} - p\right) + \frac{\partial}{\partial z}\left(T_{zx}\right) = 0. \tag{4.20}$$

Integrating Eq. 4.20 over z from the bottom $B\left(x,t\right)$ to the top $S\left(x,t\right)$ gives

$$\frac{\partial}{\partial x}\left(H\overline{(T_{xx} - p)}\right) = \left[T_{xx} - p(S)\right]\frac{\partial S}{\partial x} - \left[T_{xx} - p(B)\right]\frac{\partial B}{\partial x} - T_{xz}\left(S\right) + T_{xz}\left(B\right). \tag{4.21}$$

We assume that the top surface is traction free

$$\left(\boldsymbol{T} - p\boldsymbol{I}\right)\cdot\boldsymbol{n} = \boldsymbol{0}, \quad z = S, \tag{4.22}$$

and the bottom of both the grounded and floating ice is loaded with water pressure

p_w, effective pressure N and basal friction τ_b

$$(\boldsymbol{T} - p\boldsymbol{I}) \cdot \boldsymbol{n} = -(p_w + N)\,\boldsymbol{n} - \tau_b \boldsymbol{t}, \tag{4.23}$$

where $\boldsymbol{n}$ is the outward-pointing normal unit vector and $\boldsymbol{t}$ is the tangential unit vector. Substituting Eq. 4.12 and Eq. 4.13 into Eq. 4.21, the stress balance Eq. 4.21 can be rewritten as

$$\frac{\partial}{\partial x}\left[H\left(4\overline{\nu}\frac{\partial \overline{u}}{\partial x} - 4\left(\overline{\zeta \mathcal{S}}\right)\frac{\partial^2 \dot{\eta}_\nu}{\partial x^2}\right)\right] - \tau_b = \rho_i g H \frac{\partial H}{\partial x} + (N + p_w)\frac{\partial B}{\partial x}. \tag{4.24}$$

If the ice stream is in hydrostatic equilibrium ($p_w = \rho_i g H$) with the water underneath and has a vertically uniform viscosity ($\mathcal{S} = 0$) dominated by the horizontal strain rate ($\overline{\nu} = \frac{1}{2}A^{-1/n}|u_x|^{1/n-1}$) based on Glen's flow law, Eq. 4.24 can be simplified to

$$\frac{\partial}{\partial x}\left[2A^{-1/n}H|u_x|^{1/n-1}\frac{\partial \overline{u}}{\partial x}\right] - \tau_b = \rho_i g H \frac{\partial (H+B)}{\partial x} = \rho_i g H \frac{\partial S}{\partial x}, \tag{4.25}$$

which is the typical horizontal stress balance for the shelfy stream approximation used by Muszynski and Birchfield (1987) and MacAyeal (1989). Eq. 4.24 represents the balance between the membrane stress, basal friction and gravitational body force. For τ_b, we will consider a sliding law that includes the effect of subglacial hydrology $\tau_b = C|u_b|^{1/m-1}u_b N^{q/m}$ (Budd et al., 1979), where q, m and C are adjustable parameters.

4.2.3 Subglacial hydrology model

We follow Warburton et al. (2020) by assuming that the subglacial water is a laminar flow with a thickness h and pressure p_w. Mass conservation requires that

$$\frac{\partial h}{\partial t} + \frac{\partial q}{\partial x} = 0, \tag{4.26}$$

where q is the flux driven by the hydraulic potential ϕ. Using lubrication theory, q can be written as

$$q = -\frac{h^3}{12\mu_w}\frac{\partial \phi}{\partial x}, \tag{4.27}$$

where μ_w is water viscosity. Here ϕ is defined as

$$\phi = p_w + \rho_w g B\left(x\right) = p_w + \rho_w g\left(b(x) + h\right), \tag{4.28}$$

where we use $b(x)$ to denote the bedrock profile. Substituting Eq. 4.2 and Eq. 4.19 into Eq. 4.28 to eliminate p_w gives

$$\phi = -\frac{\partial^2 M}{\partial x^2} + \rho_i g S - N + \left(\rho_w - \rho_i\right) g\left(b(x) + h\right). \tag{4.29}$$

To close the system, we need one more equation for the effective pressure N. Assuming that the bedrock is rigid, the contact condition of the ice stream and bedrock requires that $N \to \rho_i g H$ when $h \to 0$ and $N \to 0$ when $h \to \infty$. Therefore, we relate N to the water thickness h using the function $\Lambda\left(h\right)$ used by Kyrke-Smith et al. (2014). The function is

$$N(h) = \rho_i g H \Lambda(h) = \rho_i g H \delta \ln\left(1 + \exp\frac{h_c - h}{\delta h_c}\right), \tag{4.30}$$

where $\delta = 0.1$ is a small regularisation parameter, and h_c is the critical distance above which the ice stream is treated as detached from the bed with $N \sim 0$. When $h \to 0$, $N \to \rho_i g H$, which signifies the ice shelf grounding on the bed. Conversely, when $h \gg h_c$, $N \to 0$, indicating detachment from the bed. This is an ad-hoc treatment of the contact condition of an ice stream on a rigid bed.

4.2.4 Full governing equations

Eq. 4.31 is the full set of governing equations describing the coupled dynamics of vertical viscoelastic flexure, horizontal viscous flow and subglacial hydrology, in terms of seven variables Φ, u, M, H, h, p_w, N. The bottom of the ice shelf is $B = b + h$. Therefore the mid plane is $\eta = B + \dfrac{H}{2} = b + h + \dfrac{H}{2}$. Thus the deflection η is eliminated by using the geometric constraint $\eta - b - h - \frac{1}{2}H = 0$.

The full system of the ice shelf and the subglacial water flow is governed by

$$\begin{aligned}
\frac{\partial \Phi}{\partial t} + u\frac{\partial \Phi}{\partial x} + \frac{3}{\overline{\nu} H^3} M &= 0, \\
\Phi - \frac{12\left(1-\mu^2\right)}{E H^3} M - \frac{\partial^2}{\partial x^2}\left(b + h + \frac{1}{2}H\right) &= 0, \\
\frac{\partial^2 M}{\partial x^2} - \rho_i g H + N + p_w &= 0, \\
\frac{\partial}{\partial x}\left[4\overline{\nu} H \frac{\partial \overline{u}}{\partial x}\right] - C u^{1/m} N^{q/m} - \rho_i g H \frac{\partial H}{\partial x} - (N + p_w)\frac{\partial (b+h)}{\partial x} &= 0, \\
\frac{\partial H}{\partial t} + \frac{\partial (Hu)}{\partial x} &= 0, \\
\frac{\partial h}{\partial t} - \frac{\partial}{\partial x}\left[\frac{h^3}{12\mu_w}\frac{\partial}{\partial x}\left(p_w + \rho_w g\left(b + h\right)\right)\right] &= 0, \\
N - \rho_i g H \delta \ln\left(1 + \exp\frac{h_c - h}{\delta h_c}\right) &= 0.
\end{aligned} \tag{4.31}$$

We use $H_0(x)$ to denote the initial thickness profile of the ice stream. For the

inflow boundary, the boundary conditions are

$$\begin{aligned} M &= 0, \\ \Phi &= 0, \\ H &= H_0, \\ u &= U_0, \qquad\qquad \text{at } x = -L, \\ p_w &= \rho_w g \left(s_w - b - h\right), \\ N &= \rho_i g H_0 - p_w, \\ N &= \rho_i g H \delta \ln\left(1 + \exp \frac{h_c - h}{\delta h_c}\right), \end{aligned} \tag{4.32}$$

where s_w refers to the sea level. It is set at $z = \left(\frac{\rho_w}{\rho_i}\right) H_0|_{x=-L}$. Physically, $M = 0$ and $\Phi = 0$ represent the absence of bending moment and flexure, respectively, in the upstream ice shelf. The ice thickness H is assumed to remain at its initial value $H_0|_{x=-L}$. The inflow velocity is prescribed as U_0. In addition, we assume that the subglacial water pressure p_w is hydrostatic, proportional to $s_w - b - h$, which represents the depth below sea level. Consequently, the effective pressure N can be determined from $N = p_i - p_w$. Finally, we calculate the corresponding subglacial water thickness h using Eq. 4.30.

At the steady state where s_w is fixed, the subglacial hydrological system is in equilibrium with the sea, with no flux in the drainage system. However, water flow can be driven by ocean tides with s_w evolving periodically. For the outflow

boundary at $x = \infty$, the boundary conditions are

$$\begin{aligned} M &= 0, \\ h\left(x\right) &= s_w - \frac{\rho_i}{\rho_w} H_0 - b, \\ \Phi &= 0, \\ H &= H_0|_{x=L}, \qquad \text{at } x = L, \\ 4\overline{\nu}\frac{\partial u}{\partial x} &= \sigma_b\left(t\right), \\ p_w &= \rho_i g H, \\ N &= 0, \end{aligned} \tag{4.33}$$

where σ_b is a parameterisation of the buttressing stress (Robel et al., 2017). At the downstream boundary, we assume that the ice shelf is floating freely, with zero bending moment M and zero viscous curvature Φ. The subglacial water thickness h is determined by the elevation difference between the ice-shelf bottom and the bedrock. The water pressure p_w is balanced by the ice overburden pressure $\rho_i g H$, resulting in an effective pressure of 0. The ice thickness H remains at the initial value $H_0|_{x=L}$. In addition, the downstream boundary is subject to an extensional stress σ_b, which represents the buttressing effect exerted by pinning points.

For simplicity, a linear bedrock profile $b(x) = -\theta x$ ($\theta \ll 1$) and a linear initial ice thickness profile $H_0(x) = H_i - \beta x$ are used for all simulations. Here H_i is the ice thickness at $x = 0$ and treated as a constant. Note that on tide timescales, the thickness variation of the ice shelf is negligible, thus the ice thickness H can be approximated by the initial thickness profile H_0. We can drop the mass balance(5th) equation in Eq. 4.31 that governs H.

4.2.5 Nondimensionalisation

For the flexure problem, the bending lengthscale describes the characteristic wavelength of elastic flexure

$$l_w = \left(\frac{EI}{\rho_w g}\right)^{\frac{1}{4}}, \tag{4.34}$$

where ρ_w is the density of the sea water. We use the following scales to nondimensionlise the problem

$$[x] = l_w, \quad [H] = l_w, \quad [b] = l_w, \quad [h] = h_0, \quad [t] = \frac{12\mu_w}{\rho_w g l_w \varepsilon^2} = \tau, \quad [u] = U_0,$$
$$[N] = N_0 = \rho_i g l_w, \quad [p_w] = p_0 = \rho_i g l_w, \quad [M] = M_0 = \rho_i g l_w^3, \quad [\Phi] = \Phi_0 = \frac{1}{l_w}. \tag{4.35}$$

Here h_0 is the characteristic thickness of the subglacial water layer, which is inferred from the permeability and has a reference value of 5×10^{-4} m (Warburton et al., 2020), and τ is the characteristic timescale of subglacial water transport. We define a small parameter $\varepsilon = \dfrac{h_0}{l_w}$, which is the ratio of water thickness to the ice bending lengthscale.

Table 4.1 shows the reference values of the variables used in the model. The values of β and θ are set to resemble the geometry at the grounding line of Rutford Ice Stream. The velocity accounts for the upstream inflow velocity, and the friction coefficient is chosen such at the velocity at the grounding line matches the observed value $v \sim 400$m/yr.

Physical property	Notation	Value
Density of water	ρ_w	1027 kg m^{-3}
Density of ice	ρ_i	917 kg m^{-3}
Length of the domain	L	20 km
Ice thickness	H_i	1700 m
Initial ice thickness gradient	β	2×10^{-3}
Bedslope angle	θ	10^{-3}
Sliding law component (velocity)	m	3
Sliding law component (effective pressure)	q	1
Glen's Law exponent	n	3
Characteristic (inflow) velocity	u_0	300 m y^{-1}
Friction coefficient	C	1.5×10^4 Pa$^{1/n}$ m^{-1}
Young's modulus	E	0.88×10^9 Pa
Poisson's ratio	μ	0.33
M2 (Lunar) Tidal amplitude	A_M	3 m
S2 (Solar) Tidal amplitude	A_S	3 m
Lunar tidal period	T_M	12.42 hr
Solar tidal period	T_S	12.00 hr
Water thickness	h_0	5.0×10^{-4} m

Table 4.1: Parameters used in the model and their reference values.

The dimensionless governing equations are

$$
\begin{aligned}
&\frac{M_0}{l_w^2}\frac{\partial^2 \hat{M}}{\partial \hat{x}^2} - \rho_i g l_w \hat{H} + p_0 \hat{p_w} + N_0 \hat{N} = 0, \\
&\frac{\Phi_0}{\tau}\frac{\partial \hat{\Phi}}{\partial \hat{t}} + \frac{U_0 \Phi_0}{l_w}\hat{u}\frac{\partial \hat{\Phi}}{\partial \hat{x}} + \frac{3M_0}{\nu_0 \hat{\nu} l_w^3}\frac{\hat{M}}{\hat{H}^3} = 0, \\
&\Phi_0 \hat{\Phi} - \frac{12\left(1-\mu^2\right)M_0}{E l_w^3}\frac{\hat{M}}{\hat{H}^3} - \frac{h_0}{l_w^2}\frac{\partial^2 \hat{h}}{\partial \hat{x}^2} = 0, \\
&\frac{h_0}{\tau}\frac{\partial \hat{h}}{\partial \hat{t}} - \frac{h_0^3}{12\mu_w l_w^2}\frac{\partial}{\partial \hat{x}}\left[\hat{h}^3 \frac{\partial}{\partial \hat{x}}\left(p_0 \hat{p}_w - \rho_w g l_w \hat{b}\left(\hat{x}\right) + \rho_w g h_0 \hat{h}\right)\right] = 0. \\
&\hat{N} N_0 - \rho_i g H \delta \ln\left(1 + \exp\frac{h_c/h_0 - \hat{h}}{\delta h_c/h_0}\right) = 0, \\
&\frac{4\nu_0 U_0}{l_w}\frac{\partial}{\partial \hat{x}}\left[\hat{\nu}\hat{H}\frac{\partial \hat{u}}{\partial \hat{x}}\right] - C U_0^{1/m} N_0^{q/m} \hat{u}^{1/m} \hat{N}^{q/m} - \rho_i g l_w \hat{H}\frac{\partial \hat{H}}{\partial \hat{x}} - \left(\hat{N} N_0 + \hat{p} p_0\right)\frac{\partial\left(\hat{b} + \varepsilon \hat{h}\right)}{\partial \hat{x}} = 0.
\end{aligned}
\tag{4.36}
$$

Further simplification gives

$$
\begin{aligned}
&\frac{\partial^2 \hat{M}}{\partial \hat{x}^2} - \hat{H} + \hat{p} + \hat{N} = 0, \\
&\frac{\partial \hat{\Phi}}{\partial \hat{t}} + \frac{U_0}{l_w/\tau}\hat{u}\frac{\partial \hat{\Phi}}{\partial \hat{x}} + \frac{3\rho_i g \tau}{\nu_0 \hat{\nu} \Phi_0}\frac{\hat{M}}{\hat{H}^3} = 0, \\
&\hat{\Phi} - \frac{12(1-\mu^2)\rho_i g l_w}{E}\frac{\hat{M}}{\hat{H}^3} - \frac{h_0}{l_w^2}\frac{\partial^2 \hat{h}}{\partial \hat{x}^2} = 0, \\
&\frac{\partial \hat{h}}{\partial \hat{t}} - \frac{\tau \rho_w g l_w \varepsilon^2}{12\mu_w}\frac{\partial}{\partial \hat{x}}\left(\hat{h}^3\left(\frac{\rho_i}{\rho_w}\frac{\partial \hat{p}_w}{\partial \hat{x}} - \frac{\partial \hat{b}}{\partial \hat{x}} + \varepsilon\frac{\partial \hat{h}}{\partial \hat{x}}\right)\right) = 0, \\
&\hat{N} - \frac{\rho_i g H}{N_0}\delta \ln\left(1 + \exp\frac{h_c/h_0 - \hat{h}}{\delta h_c/h_0}\right) = 0. \\
&\frac{\partial}{\partial \hat{x}}\left[\hat{\bar{\nu}}\hat{H}\frac{\partial \hat{u}}{\partial \hat{x}}\right] - \frac{C U_0^{1/m} N_0^{q/m} l_w}{4\nu_0 U_0}\hat{u}^{1/m}\hat{N}^{q/m} - \frac{\rho_i g l_w^2}{4\nu_0 U_0}\hat{H}\frac{\partial \hat{H}}{\partial \hat{x}} - \left(\hat{N} + \hat{p}\right)\frac{\rho_i g l_w^2}{4\nu_0 U_0}\frac{\partial\left(\hat{b} + \varepsilon\hat{h}\right)}{\partial \hat{x}} = 0,
\end{aligned}
\tag{4.37}
$$

The dimensionless boundary conditions are

$$
\begin{aligned}
&\hat{M} = 0, \\
&\hat{\Phi} = 0, \\
&\hat{u} = 1, \\
&\hat{p}_w = \frac{\rho_w g(s_w - l_w\hat{b} - h_0\hat{h})}{p_0}, \qquad \text{at } \hat{x} = -\frac{L}{l_w} \\
&\hat{N} = \frac{\rho_i g H_0 - \rho_w g(s_w - l_w\hat{b} - h_0\hat{h})}{N_0}, \\
&\hat{N} = \frac{\rho_i g H_0}{N_0}\delta \ln\left(1 + \exp\frac{h_c - h_0\hat{h}}{\delta h_c}\right),
\end{aligned}
\tag{4.38}
$$

and

$$\begin{aligned}
\hat{M} &= 0, \\
\hat{h}\left(x\right) &= \frac{h_w}{h_0} + \frac{1}{h_0}\left(s_w - \frac{\rho_i}{\rho_w}H_0 - l_w\hat{b}\right), \\
\hat{\Phi} &= 0, \\
\hat{\overline{\nu}}\frac{\partial \hat{u}}{\partial \hat{x}} &= \frac{l_w}{4\nu_0 U_0}\sigma_b, \qquad \text{at } \hat{x} = \frac{L}{l_w} \\
\hat{p}_w &= \frac{\rho_i g H}{p_0}, \\
\hat{N} &= 0,
\end{aligned} \tag{4.39}$$

where L is the dimensionless half-length of the domain, and $s_w(t)$ is the sea level variation induced by tides.

The initial condition is determined by a purely floating ice-shelf bending profile with hydrostatic subglacial water pressure. For the floating part, the initial condition is

$$\begin{aligned}
\hat{H} &= \frac{H_0}{l_w}, \\
\hat{p}_w &= \frac{\rho_i g H_0}{p_0}, \\
\hat{h} &= \frac{h_w}{h_0} + \frac{1}{h_0}\left(s_w - \frac{\rho_i}{\rho_w}H_0 - l_w\hat{b}\right), \\
\hat{N} &= 0, \\
\hat{M} &= 0, \\
\hat{\Phi} &= 0, \\
\hat{u} &= \frac{Q_i}{U_0 H_0},
\end{aligned} \qquad . \tag{4.40}$$

where $Q_i = U_0 H_0|_{x=-L}$ is the total inflow flux at the left boundary. For the

grounded part, the initial condition is

$$\begin{aligned}
\hat{H} &= \frac{H_0}{l_w}, \\
\hat{p} &= \frac{\rho_w g \left(s_w - l_w \hat{b} - h_0 \hat{h} \right)}{p_0}, \\
\hat{N} &= \frac{1}{N_0}(\rho_i g H_0 - p_0 \hat{p}) = \frac{\rho_i g H_0 - \rho_w g (s_w - l_w \hat{b} - h_0 \hat{h})}{N_0}, \\
\hat{M} &= 0, \\
\hat{\Phi} &= 0, \\
\hat{u} &= \frac{Q_i}{U_0 H_0}, \\
\hat{h} &= -\delta \frac{h_c}{h_0} \ln \left[\exp \left(\frac{\hat{N} N_0}{\rho_i g H_0 \delta} \right) - 1 \right] + \gamma \frac{h_c}{h_0},
\end{aligned} \tag{4.41}$$

where γ is a constant such that $\hat{h}$ is continuous across the grounding line.

4.2.6 Numerical implementation

The full set of governing equations Eq. 4.36 is solved by a finite difference implementation with the SNES library of PETSc (Balay et al., 1997, 2024a,b). The computational domain is set between $\hat{x} = -50$ and $\hat{x} = 20$. The grid size is $\Delta\hat{x} = 0.35$. We use the Crank–Nicolson method for time stepping in the governing equation for h.

4.3 Results

In the model, the horizontal stress balance in Eq. 4.36 includes basal friction, gravitational driving stress, membrane stress and buttressing. In this section, we show two reference cases to demonstrate the tidal response of an idealised ice stream.

In the first case we assume that there is no buttressing from the downstream ice shelf, thus the fortnightly tidal response is a consequence of the nonlinear sliding law and viscoelastic flexure. In the second case, we adapted the tidally induced buttressing stress from Robel et al. (2017) as an additional source of nonlinearity.

4.3.1 Semi-diurnal tidal forcing without buttressing

Here we show a reference case in comparison with the results from Sect. 3.3. The outflow boundary condition is ice overburden stress with no buttressing stress $\sigma_b = 0$. The tides consist of M_2 and S_2 components with the same magnitude $A_M = A_S = 3$ m. The period of M_2 and S_2 components are denoted by $T_M = 12.42$ hr and $T_S = 12$ hr, respectively. For simplicity, we assume a constant ice viscosity $\nu = \bar{\nu}$. The Maxwell time of ice, denoted λ, is given by $\lambda = \bar{\nu}/E \sim 63$ hr. For the sliding law, we choose a nonlinear one with $m = 3$ and $q = 1$. The geometric and tidal parameters are close to the characteristic parameters observed at the Rutford Ice Stream (Morlighem et al., 2017, 2020).

As done in Sect. 3.3, we calculate the tidal variations in flexural stress, grounding-line position, and ice velocity near the grounding line.

Fig. 4.2 shows the tidal response at different tidal phases in one tidal period. Similar to Sect. 3.3, the maximum tensile stress and surface velocity occur at low tides shown in panel (d), similar to the results in chapter 3. In this case, the ice-thickness gradient β is large in the grounding zone. Therefore, tidal variations in the subglacial water pressure are too small to overcome the increasing weight of the ice column upstream of the grounding line, making it difficult for the grounding line to migrate further upstream at high tides. Fig. 4.3 shows the water thickness in the grounding zone at four tidal phases. At low tides, the retained water thickness in the grounding zone is close to the critical value h_c, which is the boundary condi-

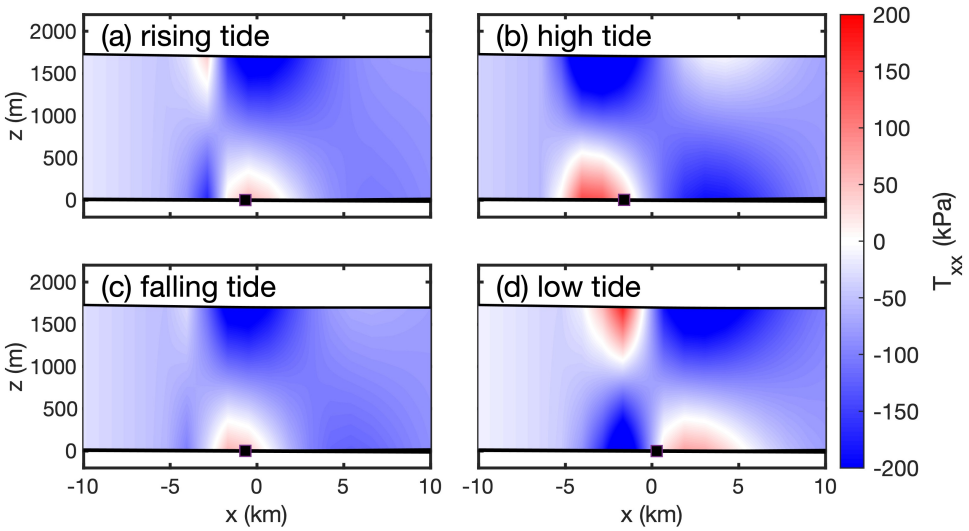

Figure 4.2: Tidally induced horizontal deviatoric stress T_{xx} in a tidal period near the grounding line, which is denoted by the black square. **(a)** rising tide at $t = 0$, **(b)** high tide at $t = 0.25T_S$, **(c)** falling tide at $t = 0.5T_S$, **(d)** low tide at $t = 0.75T_S$.

tion for h at $x \to -\infty$, indicating that the shelf is attached to the bed, with $N > 0$. This is different from Warburton et al. (2020), where the retained water layer is much larger than h_c, causing detachment of the shelf from the bed. Therefore, subglacial water pressure p_w in this case can be approximated to be hydrostatic. Recall that in this case, we use $h_0 = 5 \times 10^{-4}$ m, and the permeability of the subglacial hydrological system scales with h_0^3. Models with a higher drainage permeability ($h_w = 5 \times 10^{-3}$ m and 5×10^{-2} m) give similar results, indicating that the subglacial drainage process occurs without any temporal lag and can be approximated as hydrostatic in this Rutford-like case.

This is different from the results from Warburton et al. (2020), where the bedslope angle is smaller and the variations in the ice thickness is not considered. Therefore, tidal variations in the ice velocity u are mainly caused by the tidally modu-

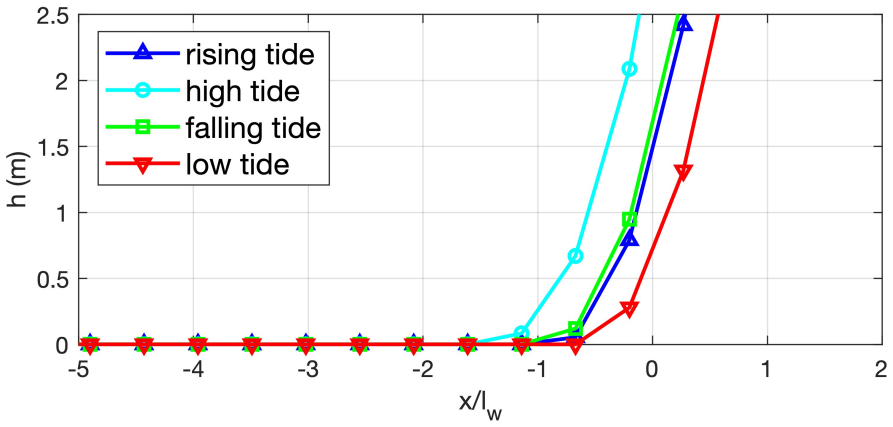

Figure 4.3: Tidally modulated subglacial water thickness h at different tidal phases. Here the origin of the x-axis is randomly chosen. And the y-axis is the water thickness in metres.

lated gravitational driving stress $\rho_i g H \dfrac{\partial S}{\partial x}$. At low tides, when the ice shelf in the grounding zone is attached to the bedrock, the surface elevation gradient is $\dfrac{\partial S}{\partial x} = \theta + \beta$. The gravitational driving stress is thus $\rho_i g H\,(\theta + \beta)$. At high tides, when the ice shelf floats up, the surface gradient is reduced to $\dfrac{\partial S}{\partial x} = \left(1 - \dfrac{\rho_i}{\rho_w}\right)\beta$, giving a much smaller driving stress $\rho_i g H \left(1 - \dfrac{\rho_i}{\rho_w}\right)\beta$. Thus the amplitude of tidal variations in gravitational driving stress is $\sigma_{h0} = \rho_i g H \left(\theta + \dfrac{\rho_i}{\rho_w}\beta\right) \approx 40$ kPa.

Fig. 4.4 shows the time series of velocity, grounding-line migration and detrended horizontal displacement over several tidal periods. The results begin with $t = 30T$, after spin-up of the model. While the ice is advected by the background flow at a constant velocity, our primary focus is on the tidal variations in displacement. Therefore, the displacement is detrended to exclude the effects of background advection. Here R+40 represents the GPS station 40 km upstream of the grounding line, R-20 is the station 20 km downstream of the grounding line, and $R0$ is the one at the grounding line. The horizontal velocity reaches its maximum at low tides when the driving stress is maximised (Fig. 4.4c). Spa-

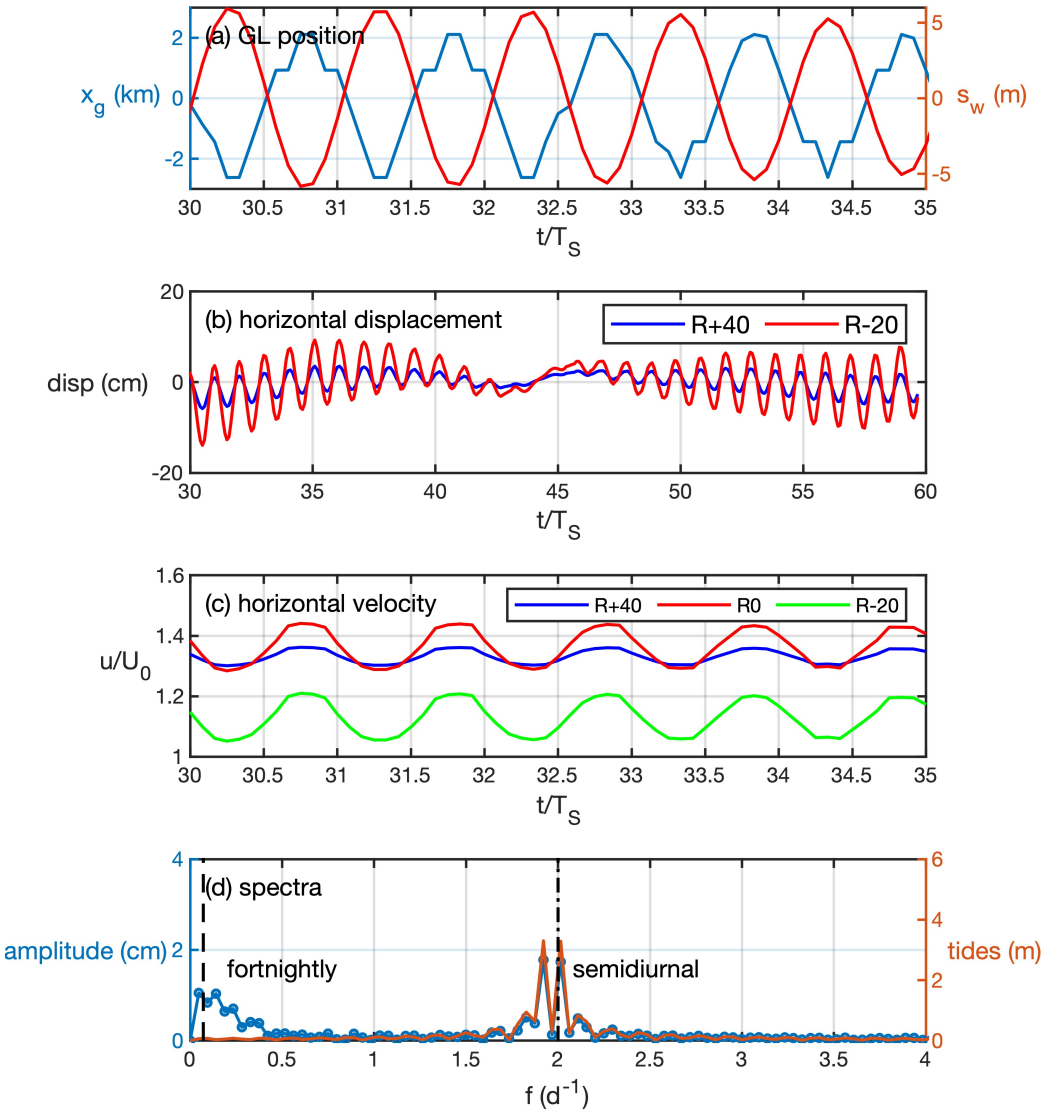

Figure 4.4: Time series of **(a)** grounding-line position and sea level s_w, **(b)** detrended horizontal displacement, **(c)** velocity. **(d)** Spectra of tides and the detrended tidal displacement at R+40 in the reference case.

tially, the tidal variation reaches the max magnitude at $R0$ and diminishes further upstream. The tidal signals observed on the ice shelf at $R - 20$ are nearly identical to those at R_0, indicating minimal spatial variation at the ice shelf. As shown in Fig. 4.4(a), the grounding-line migration is asymmetric with respect to tidal height. Fortnightly variations in the detrended horizontal displacement are observed (Fig. 4.4b). Fig. 4.4(d) shows the tidal responses in the frequency domain, where there are two peaks corresponding to fortnightly variations and semi-diurnal variations. However, the produced fortnightly variations have a smaller magnitude compared with observations ($\sim$ 10 cm). More importantly, the above results indicate that the ice stream is dominated by tidal variations in the gravitational driving force. The daily maximum horizontal velocity occurs at low tides with higher driving stress. However, at the Rutford Ice Stream, the observed daily maximum horizontal velocity occurs at high tides instead, indicating that the basal shear stress or buttressing from downstream ice shelves is the dominant control. We will discuss the effect of buttressing in the following.

4.3.2 Tidal responses with buttressing

The nonlinear tidal responses can be a consequence of tidally modulated buttressing stress due to ephemeral grounding at the pinning point (Robel et al., 2017) or ice-shelf margin (Minchew et al., 2017). The low-tide downward deflection of ice shelves is restricted by the pinning points underneath, but the high-tide upward deflection is free. Therefore, variations in the depth-integrated basal shear stress are larger from mean to high tide than from low tide to mean, leading to a buttressing effect that is asymmetric to tidal height. Robel et al. (2017) studied the tidal response of a viscoelastic ice shelf with a parameterised buttressing stress. We follow this parameterisation by imposing a buttressing stress σ_b on the outflow

boundary of the domain. It takes the form

$$\sigma_b = \sigma_{b0} \left[2^{1-\alpha} (1 + \hat{s_w}(t))^{\alpha} - 1 \right], \tag{4.42}$$

where α is a "shape parameter measuring the asymmetry in buttressing stress with respect to tidal height", and σ_{b0} is the magnitude of buttressing stress. Eq. 4.42 serves as a parametrisation of the nonlinear dependence of the buttressing stress on tidal height. The physics underlying Eq. 4.42 is the nonlinear dependence of the total contact area on tidal height at a pinning point. As the tide rises from mean to high tide, the reduction in contact area is larger than rising from low to mean tide. If we assume that the basal shear stress is uniform across the contact area, this results in a nonlinear dependence of the buttressing force, derived from the spatially integrated basal shear stress, on tidal height.

When $\alpha = 1$, it is reduced to the linear case $\sigma_b = \sigma_{b0} \hat{s_w}(t)$. In this case, we consider the Rutford-like case where $\alpha = 1.54$ following Robel et al. (2017). The magnitude of tidal variations in buttressing stress is 1.4 times the driving stress, giving $\sigma_{b0} = 1.4\sigma_{h0}$.

The pattern of tidal stress T_{xx} in Fig. 4.5 is similar to the case without buttressing (Fig. 4.2). However, because of the additional compressive stress provided by the pinning point on the outflow boundary, the tensile stress on the ice surface is reduced. Meanwhile, in addition to the tidal responses due to asymmetric grounding-line migration (Fig. 4.4), the buttressing nonlinearity in Eq. 4.42 produces fortnightly variations through "frequency mixing" of the solar tidal component S_2 and the lunar tidal component M_2 (Robel et al., 2017), giving rise to larger fortnightly variations (Fig. 4.6d) compared with the previous case. The magnitude of fortnightly variations (Fig. 4.6d) is about five times larger than the previous case.

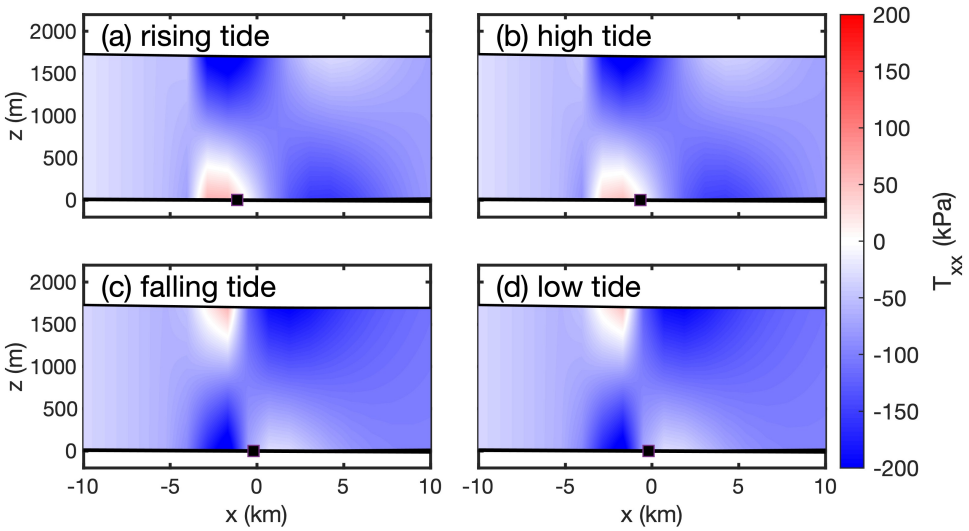

Figure 4.5: Tidally induced stress T_{xx} in a tidal period near the grounding line where buttressing is provided by pinning points. **(a)** rising tide at $t = 0$, **(b)** high tide at $t = 0.25T_S$, **(c)** falling tide at $t = 0.5T_S$, **(d)** low tide at $t = 0.75T_S$.

4.4 Discussion

In Sect. 4.3, we have shown that for an ideal Rutford-like ice stream, the subglacial hydrology is nearly hydrostatic. Besides the ephemeral grounding at the ice-shelf pinning point (Minchew et al., 2017; Robel et al., 2017; Zhong et al., 2023), asymmetric grounding-line migration with viscoelastic flexure can cause fortnightly variations through the nonlinear basal sliding law. Here, we focus on exploring the effects of the nonlinear sliding law and viscoelastic flexure near the grounding line. Although the effect of the nonlinear sliding law is much smaller than of the buttressing in the reference cases, we show now that it can be large depending on the choice of sliding laws and rheological parameters. In the following calculation, we exclude the parameterised buttressing stress in the force balance and only consider the effect of basal sliding.

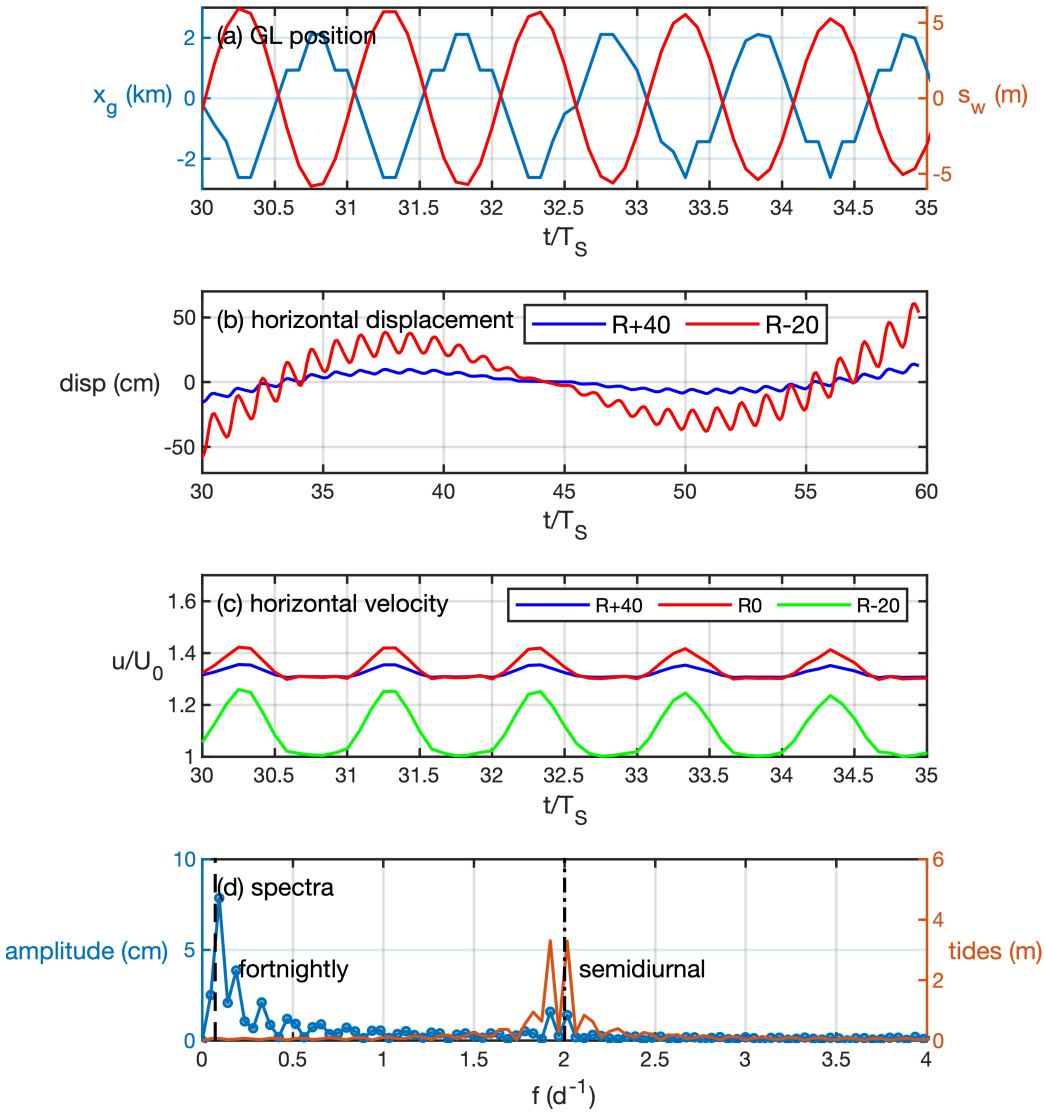

Figure 4.6: Time series of **(a)** grounding-line position and sea level s_w, **(b)** detrended displacement, **(c)** velocity with the buttressing effect from pinning points. **(d)** Spectra of the detrended tidal displacement at R+40 in the reference case.

4.4.1 Effect of the nonlinear sliding law

As shown by Gudmundsson (2011), the basal sliding law can cause nonlinearity and affect the tidal responses of ice streams. For the horizontal viscous flow, we investigate how the nonlinear sliding law contributes to the tidal response. The key dimensionless parameter here is the ratio of the basal friction to the membrane stress $\frac{\tau_b}{4\nu_0 U_0/l_w}$. Here we follow Gudmundsson (2011) and consider sliding laws where $q = 1$ and $m = 1, 3, 10$. Here m serves as a metric of nonlinearity, where $m = 1$ represents the linear case and $m = 3, 10$ represents the nonlinear cases. The typical Weertman type sliding law ($m = 3$, $q = 0$) accounts for sliding on a hard bed. And the limit $m \to \infty$ corresponds to sliding on plastic subglacial sediments, where basal shear stress is constant. The nonlinearity gets stronger with increasing m, which accounts for the transition from a hard bed to plastic sediments. For all cases we modify the value of the slipperiness C such that the ice velocity at the grounding line matches the observed value $u \approx 400$ m/yr. Fig. 4.7 shows the modelled time series of the fortnightly and semi-diurnal variations in the detrended displacement (Fig. 4.7(a)) and the corresponding amplitude in the frequency domain (Fig. 4.7(b)). The semi-diurnal component is insensitive to the form of the sliding law. However, the fortnightly component increases with m and can dominate the system with a sufficiently nonlinear sliding law with $m = 10$, which is in agreement with Gudmundsson (2011). However, different from Gudmundsson (2011), even with a linear sliding law $m = 1$, there is still a fortnightly component comparable to the semi-diurnal component, which can be explained by the asymmetric grounding-line migration caused by the viscoelastic flexure (Fig. 4.4(b), Fig. 4.6(b)).

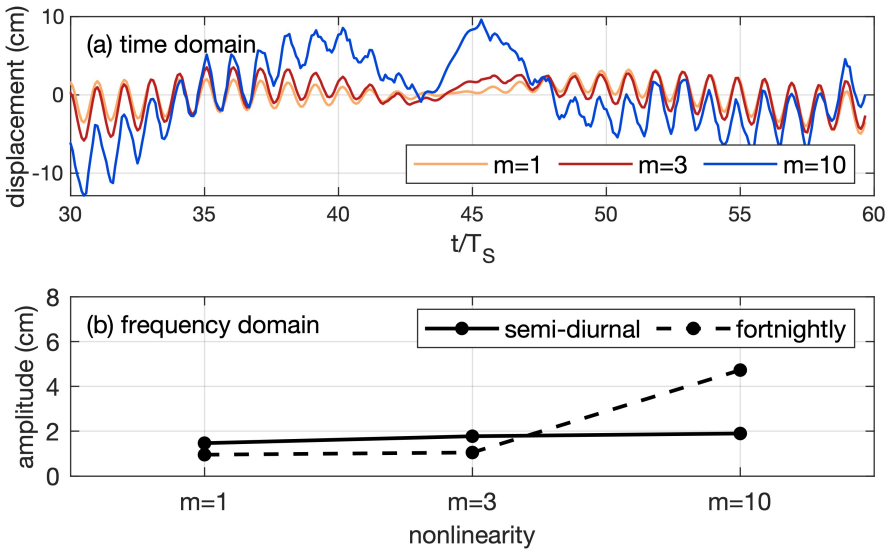

Figure 4.7: **(a)** The time series of detrended displacement at R+40 with different values of m. **(b)** Amplitude of the fortnightly and semi-diurnal detrended displacement with different m.

4.4.2 Sensitivity to elastic modulus

The tidally induced viscoelastic flexure has two important timescales: the tidal timescale $T_S = 12$ hr and the Maxwell time of ice $\lambda = \bar{\nu}/E$. The Maxwell time of ice controls how quickly elastic deformation is relaxed by viscous creep. However, the elastic modulus of the ice shelf is poorly constrained, causing uncertainties in λ and thus the modelled tidal responses. Here we assume a constant ice viscosity and show how different elastic moduli and the corresponding ratio λ/T_S controls the type of tidal responses. We use a nonlinear sliding law with $q = 1$ and $m = 3$ that is consistent with the reference case in Sect. 4.3.

In Fig. 4.8, the amplitude of both fortnightly and semi-diurnal tidal variations at R+40 is plotted against the ratio λ/T_S. When the elastic modulus E is large, λ is close to the tidal period ($\lambda/T_S \sim 1$), and ice behaves viscoelastically. The tidal response is predominantly fortnightly. When E is small, elastic deformation

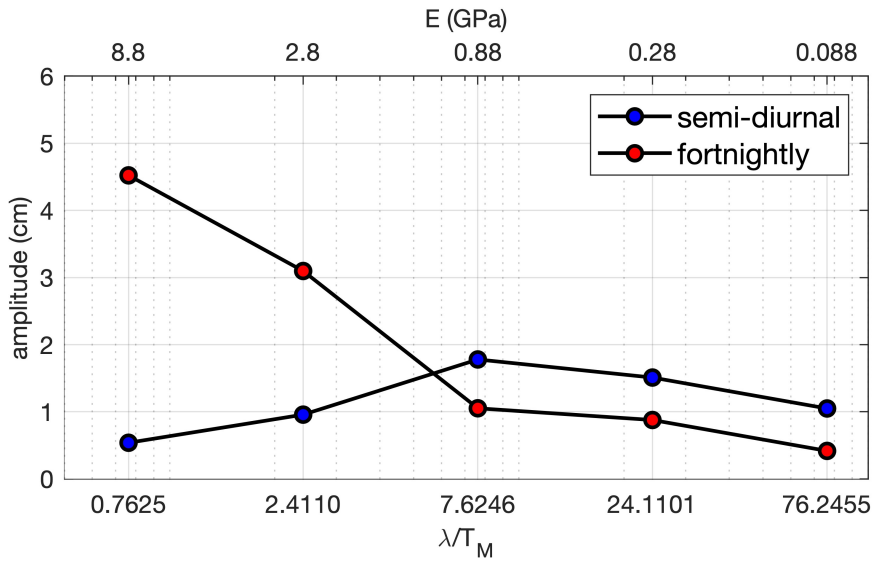

Figure 4.8: The amplitude of tidal variations in detrended displacement at 40 km upstream the grounding line as a function of Maxwell time λ. The red-dotted line represents the fortnightly component, and the blue-dotted line represents the semi-diurnal component.

dominates in the grounding zone. The semi-diurnal tidal variation remains close to other cases, but the fortnightly variations vanish. The results suggest that the viscoelastic rheology is critical in producing the nonlinear tidal responses.

A possible explanation is that the fortnightly variation depends on the asymmetric grounding-line migration. When ice in the grounding zone is elastic, the grounding-line migration is symmetric to tidal forcings, as shown by the elastic flexure models (Sayag and Worster, 2011; Wagner et al., 2016). The linear system can not produce fortnightly variations in the displacement through frequency mixing of M2 and S2 tidal components. However, when the shelf is sufficiently viscous, the grounding line migrates asymmetrically with respect to tidal forcings, as shown by Stubblefield et al. (2021) and chapter 3. The asymmetry might be an intrinsic property of the viscous and viscoelastic contact problems, even with hydrostatic subglacial water pressure. Further analysis of the viscoelastic contact

problem is required to find the dependence of tidal responses on ice rheology.

4.4.3 Limitation

The model is limited by a lack of lateral shear stress in the horizontal stress balance. Lateral stress may also contribute to nonlinearity in tidal responses, particularly through periodic grounding (Minchew et al., 2017). Since lateral stress can be formulated similarly to basal friction, the flowline model can be extended to incorporate a parameterisation of lateral shear stress into Eq. 4.24.

Meanwhile, the robustness of the numerical model should be enhanced to explicitly account for the ephemeral grounding line at a pinning point, instead of using the current parameterisation in Eq. 4.42 (Robel et al., 2017).

4.5 Conclusion

We modelled the tidal responses of an idealised Rutford-like ice stream and its subglacial hydrology using a depth-integrated flow-line model. The subglacial water pressure was found to be nearly hydrostatic, primarily due to the increasing weight of the ice towards the inland ice streams. Our findings demonstrate that in addition to ephemeral grounding at pinning points (Minchew et al., 2017; Robel et al., 2017) and nonlinear sliding law (Gudmundsson, 2011), viscoelastic flexure modulate fortnightly tidal variations. We further examined the sensitivity of these fortnightly variations to changes in the elastic modulus and the form of the sliding law. The results underscore the importance of viscoelastic flexure and nonlinear sliding law in driving nonlinear tidal responses, which are governed by the ratio of the Maxwell time to the tidal period.

As discussed in chapter 3 and Sect. 4.3, viscoelastic and viscous grounding zones

exhibit asymmetric grounding-line migration—a characteristic not present in purely elastic models. For nonlinear tidal responses induced by buttressing, Robel et al. (2017) demonstrated that the magnitude of these responses is influenced by the geometry of the ice and bedrock, with viscoelastic rheology primarily contributing to the phase lag between tidal variations in horizontal displacement and tidal height. However, our results suggest that for nonlinear tidal responses induced by viscoelastic flexure, viscoelasticity modulates the magnitude of fortnightly tidal variations. Future research will focus on the analytical properties of the viscoelastic contact problem in the grounding zone, with a particular focus on the dependence of nonlinear tidal responses on ice rheology.

5 | Ice shelf bending near the calving front

5.1 Introduction

Ice shelves can provide buttressing to grounded ice sheets. They lose mass through calving and basal melting (Depoorter et al., 2013). Unlike ice sheets that are influenced by basal friction, ice shelves behave like a floating, thin plate that undergoes vertical flexure and horizontal stretching (Cuffey and Paterson, 2010).

As typical flexure profiles of Antarctic ice shelves near their edges, the rampart–moat and berm profiles were first observed and named by Scambos et al. (2005) at the Ronne Ice Shelf. In warm water, the ice-shelf edge is raised up by up to 5 meters, with an edge-parallel moat located upstream. In contrast, in colder water, the shelf edge bends down and forms so-called "berms" upstream of the edge (Scambos et al., 2005). Both profiles are consequences of the shelf-edge flexure. A similar deflection profile was also observed by Sartore et al. (2024) at the Ross Ice Shelf. They analyse ICESat elevation profiles from 2003 to 2007 that have a growing rampart–moat deflection profile between 2003 and 2006, followed by a calving event of about 950 meters. Using an elastic thin-plate model, they have attributed the rampart–moat profile to elastic bending caused by an underwater ice foot that provides additional buoyancy force at the calving front. Such observations of growing flexure and subsequent calving events motivate us to investigate shelf-edge flexure using the viscoelastic thin plate theory and consider its relationship with calving.

As introduced in Sect. 3.1, edge flexure can be treated with thin plate theory using viscous (Reeh, 1968), elastic (Wagner et al., 2016) or viscoelastic rheology (Walker et al., 2013; MacAyeal and Sergienko, 2013; MacAyeal et al., 2021). For

a vertically uniform ice shelf, the imbalance between the ice overburden stress and water pressure on the edge causes downward flexure, as shown in Reeh (1968). However, Buck (2024) modelled the elastic flexure near the edge with vertically non-uniform viscosity. He showed that the vertical variations in ice viscosity can reverse the bending moment due to stress imbalance, causing upward flexure that forms a rampart. The modelled deflection profile matched the observations when using an effective bending lengthscale that is determined by viscous creep. However, the temporal evolution of the shelf deflection and the effect of underwater feet were not studied.

This chapter, as an extension to Buck (2024), is aimed at setting up a viscoelastic flexure framework that includes both the vertically non-uniform viscosity and underwater ice feet. The model should predict the evolution of the shelf deflection and the tensile stress that is associated with calving, thus answer the question that *what is the controlled mechanism of ice–shelf edge flexure in the rampart–moat and berm profiles*. We follow the viscoelastic bending model by Walker et al. (2013) to account for both the elastic response after a calving event and the subsequent viscous creep. We show how strain and stress are built up near the shelf edge to form the rampart–moat and berm profiles and how these profiles evolve due to viscous creep.

5.2 Method

In this section, we set up the viscoelastic thin plate model by adding a viscous modification to the elastic beam theory of Walker et al. (2013). Fig. 5.1 shows a schematic of the model. The coordinate system is $\boldsymbol{x} = (x, z)$, with the positive x direction pointing to the upstream direction and positive z direction pointing upward. The calving front is at $x = 0$, with the ice flow from right to left. The

thickness of the ice shelf is assumed to be a constant h. The neutral plane is defined by $z = w(x)$, where $w(x)$ is the deflection.

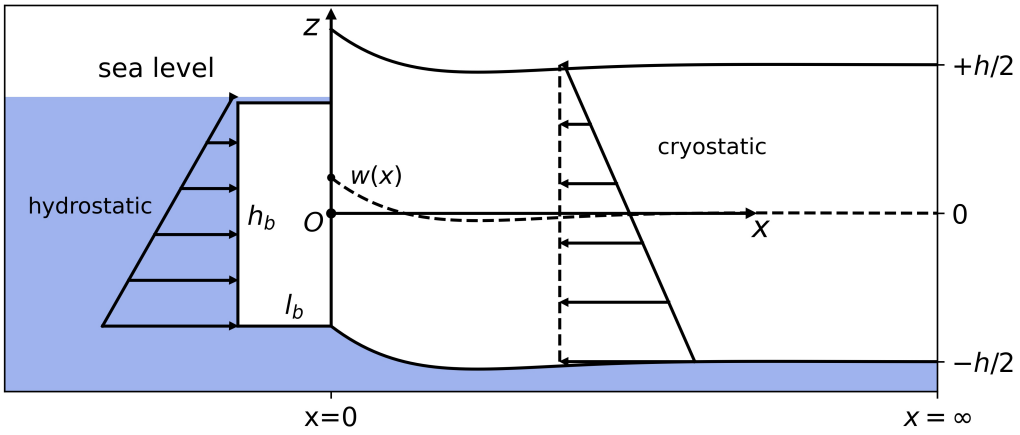

Figure 5.1: The model set up for flexure at the edge of an ice shelf.

5.2.1 Elastic thin plate

According to the elastic thin plate model (Turcotte and Schubert, 2002), the deflection profile $w(x)$ satisfies

$$\frac{\partial^2}{\partial x^2}\left(E'I\frac{\partial^2 w}{\partial x^2}\right) = q(x), \tag{5.1}$$

where $E' = \dfrac{E}{1-\mu^2}$ is the effective Young's modulus for plane strain, E is the Young's modulus, μ is Poisson's ratio, I is the second moment of area, and $q(x)$ is the distributed force. Here we assume that E' is constant and drop the $'$ from E'. For an ice shelf with thickness h, the moment I is $I = \dfrac{h^3}{12}$, and the distributed force is the sum of gravity and water pressure

$$q(x) = -\rho_i g h + \rho_w g\left(\frac{\rho_i}{\rho_w}h - w\right) = -\rho_w g w. \tag{5.2}$$

Substituting Eq. 5.2 into Eq. 5.1, we have

$$\frac{\partial^2}{\partial x^2}\left(EI\frac{\partial^2 w}{\partial x^2}\right) + \rho_w g w = 0. \tag{5.3}$$

The ice shelf is loaded with a bending moment M_e and a shear force Q_e on the edge $x = 0$, and is assumed to be flat without flexure far upstream ($x \to \infty$). The boundary conditions are

$$\begin{aligned} M = -EI\frac{\partial^2 w}{\partial x^2} &= M_e, \quad x = 0, \\ Q = \frac{\partial M}{\partial x} = -\frac{\partial}{\partial x}\left(EI\frac{\partial^2 w}{\partial x^2}\right) &= Q_e, \quad x = 0, \\ w = w_x = w_{xx} &= 0, \quad x \to \infty. \end{aligned} \tag{5.4}$$

Physically, M_e accounts for the net bending moment due to the pressure difference between water and ice (Reeh, 1968) and the vertically non-uniform viscosity (Buck, 2024). Here Q_e accounts for the buoyancy shearing force provided by the underwater ice foot (Scambos et al., 2005; Sartore et al., 2024). Both M_e and Q_e should depend on the deflection at the edge w_e. For the elastic flexure problem, we assume that w_e is small so that M_e and Q_e can be approximated as constants. In the viscoelastic model, we consider the full problem with M_e and Q_e as functions of w_e. Eq. 5.3 can be solved analytically to obtain the elastic flexure profile

$$w = -\frac{2M_e}{\rho_w g l_w^2}\exp\left(-\frac{x}{l_w}\right)\left[-\sin\left(\frac{x}{l_w}\right) + \left(1 + \frac{Q_e l_w}{M_e}\right)\cos\left(\frac{x}{l_w}\right)\right], \tag{5.5}$$

where l_w is the bending lengthscale of a floating ice shelf

$$l_w = \left(\frac{4EI}{\rho_w g}\right)^{1/4}. \tag{5.6}$$

The elastic flexure profile Eq. 5.5 is essentially a linear superposition of the deformation induced by M_e and Q_e. In Sect. 5.2.2, we will use Eq. 5.5 as the initial condition for the viscoelastic flexure problem.

5.2.2 Viscoelastic thin plate

For a viscoelastic ice shelf, the elastic bending strain is relaxed viscously. The dimensional governing equation is (Walker et al., 2013)

$$\frac{\partial}{\partial t}\left[\frac{\partial^2}{\partial x^2}\left(EI\frac{\partial^2 w}{\partial x^2}\right)\right] + \rho_w g\frac{\partial w}{\partial t} + \frac{E\rho_w g}{2\eta}w = 0, \tag{5.7}$$

where η is the viscosity of ice, assumed to be a constant for simplicity. A detailed derivation of Eq. 5.7 can be found in Sect. A.6. Eq. 5.7 shows that the curvature of the viscoelastic beam increases with time due to viscous creep. This results in a decrease of the effective bending legnthscale, which will be discussed in the following. The bending moment M_e and shearing force Q_e are applied on the edge. The boundary conditions are

$$\begin{aligned}
\int_0^t \frac{E}{2\eta}M_e \mathrm{d}\tau + M_e - M_{e,0} &= -EI\left[\frac{\partial^2 w}{\partial x^2} - \frac{\partial^2 w_0}{\partial x^2}\right], \quad x = 0, \\
\int_0^t \frac{E}{2\eta}Q_e \mathrm{d}\tau &= -EI\left[\frac{\partial^3 w}{\partial x^3} - \frac{\partial^3 w_0}{\partial x^3}\right], \quad x = 0, \\
w = w_x = w_{xx} &= 0, \quad x \to \infty,
\end{aligned} \tag{5.8}$$

where $\int_0^t \mathrm{d}\tau$ represents the integration over time from the initial condition to time t, $M_{e,0}$ and w_0 are the initial ($t = 0$) bending moment and the initial shelf deflection at the edge, respectively. Here we drop the term $Q_e - Q_{e,0}$ in the second equation because the buoyancy force provided by an underwater ice foot is constant if the foot remains under the sea level, which is true in our study. Because of the viscoelastic rheology, the deflection at the edge increases with time due to

viscous creep, causing changes in the bending moment and the shearing force.

5.2.3 Nondimensionalisation

We nondimensionalise the governing equation Eq. 5.7 with the following scales,

$$\begin{aligned} \hat{x} = \frac{x}{l_w}, \quad \hat{w} = \frac{w}{w_a}, \quad \hat{t} = \frac{t}{\lambda} = \frac{t}{\eta/E}, \\ \hat{M}_e = \frac{M_e}{EIw_a/l_w^2}, \quad \hat{Q}_e = \frac{Q_e}{EIw_a/l_w^3} \end{aligned} \tag{5.9}$$

where $\hat{\cdot}$ represents dimensionless variables. The dimensionless equation and boundary conditions are given in Eq. 5.10 and Eq. 5.11, respectively,

$$\frac{\partial^4 \hat{w}}{\partial \hat{x}^4} + 4\hat{w} + 2\int_0^{\hat{t}} \hat{w} \mathrm{d}\hat{t} = \frac{\partial^4 \hat{w}}{\partial \hat{x}^4}|_{\hat{t}=0} + 4\hat{w}|_{\hat{t}=0} = 0, \tag{5.10}$$

$$\begin{aligned} \frac{\partial^2 \hat{w}}{\partial \hat{x}^2} = \frac{\partial^2 \hat{w}}{\partial \hat{x}^2}\left(\hat{t}=0\right) - (\hat{M}_e - \hat{M}_{e,0}) - \frac{1}{2}\int_0^{\hat{t}} \hat{M}_e d\hat{t}, \quad \hat{x} = 0, \\ \frac{\partial^3 \hat{w}}{\partial \hat{x}^3} = \frac{\partial^3 \hat{w}}{\partial \hat{x}^3}\left(\hat{t}=0\right) - \frac{1}{2}\int_0^{\hat{t}} \hat{Q}_e d\hat{t}, \quad \hat{x} = 0, \\ \hat{w} = \frac{\partial \hat{w}}{\partial \hat{x}} = \frac{\partial^2 \hat{w}}{\partial \hat{x}^2} = 0, \quad \hat{x} \to \infty. \end{aligned} \tag{5.11}$$

Here $\hat{t} = 0$ represents the initial condition. In the following section, we assume that the initial condition is the elastic bending profile given by Eq. 5.5.

5.2.4 Boundary conditions on the edge

In this section, we derive the net bending moment M_e and the shearing force Q_e on the shelf edge. We consider the effect of both an underwater ice feet (Scambos et al., 2005; Sartore et al., 2024) and a vertically non-uniform viscosity(Buck, 2024).

5.2.4.1 Underwater ice foot

The underwater ice foot is formed due to variations of frontal melt with depth. At the calving front, ice melting at the waterline is enhanced by warm surface water and convection due to surface waves. This leads to the formation of a melting notch, followed by the collapse of the overhanging ice slab and the formation of the underwater ice foot (Slater et al., 2018, 2021; Sartore et al., 2024). Assuming that the foot has a rectangular shape and is completely below sea level, the force balance suggests that $Q_e = -\left(\rho_w - \rho_i\right) g l_b h_b$, where l_b and h_b are the length and height of the ice foot, respectively. We choose the length of the ice foot to be 10 m. The top surface of the ice foot is assumed to be 20 m below the sea level (Sartore et al., 2024). Therefore $h_b = \dfrac{\rho_i}{\rho_w} h - 10$ m, $l_b = 20$ m.

5.2.4.2 Internal bending moment due to vertical viscosity gradient

We follow Buck (2024) in deriving the internal bending moment M_e due to the vertical viscosity gradient. For an ice shelf, neglecting the atmospheric pressure, the stress consists of ice overburden pressure and horizontal tensile resistive stress $\Delta\sigma$

$$\begin{aligned} \sigma_{xx} &= \rho_i g \left(z - \frac{h}{2}\right) + \Delta\sigma\left(z\right), \\ \sigma_{zz} &= \rho_i g \left(z - \frac{h}{2}\right). \end{aligned} \tag{5.12}$$

We assume hydrostatic water pressure P_w on the edge,

$$P_w\left(z\right) = \begin{cases} 0 & \left(z \geq s_w\right), \\ \rho_w g \left(s_w - z\right) & \left(z < s_w\right), \end{cases} \tag{5.13}$$

where $s_w = \left(\dfrac{\rho_i}{\rho_w} - \dfrac{1}{2}\right) h$ is the sea level. The internal bending moment M_I

is caused by the stress imbalance between the internal stress σ_{xx} and the water pressure P_w at the edge

$$M_I = \int_{-h/2}^{h/2} \left(-P_w(z) - \sigma_{xx}\right) z \mathrm{d}z. \tag{5.14}$$

To calculate M_I we need to derive the tensile resistive stress $\Delta\sigma\,(z)$ with further assumptions. If we assume that $\Delta\sigma\,(z)$ is vertically uniform ($\Delta\sigma\,(z) = \overline{\Delta\sigma} =$ const), the force balance gives

$$\overline{\Delta\sigma} = \left[\frac{1}{2}\rho_i g h - \frac{1}{2}\rho_w g \left(\frac{\rho_i}{\rho_w} h - w_e\right)^2\right], \tag{5.15}$$

where w_e is the edge deflection. When the deflection is negligible $w_e \sim 0$, the simplified Eq. 5.15 is in agreement with Weertman (1957).

We denote the bending moment with a vertically uniform tensile resistive stress $\overline{\Delta\sigma}$ as M_w:

$$M_w = -\frac{1}{12}\left(\frac{\rho_i}{\rho_w}\right)\left(\rho_w - \rho_i\right) g h^3 \left[1 - 2\frac{\rho_i}{\rho_w}\right] > 0, \tag{5.16}$$

which indicates that the edge bends down due to the stress imbalance with vertically uniform tensile resistive stress. However, the ice shelves in Antarctica are usually subject to a vertically non-uniform temperature profile, with the upper surface colder than the bottom that is in contact with the sea (Cuffey and Paterson, 2010). According to Glen's law, the ice viscosity is also vertically non-uniform

$$\eta(\dot{\varepsilon}, T) = A^{-1/n} \dot{\varepsilon}^{\left(\frac{1}{n}-1\right)} \exp\left(\frac{Q_0}{RT}\right), \tag{5.17}$$

where $\dot{\varepsilon}$ is the strain rate, A, n and R are constants, Q_0 is the activation energy, and T is the temperature. Vertical variations in T cause vertically non-uniform

viscosity $\eta(z)$ and thus the stress $\Delta\sigma\,(z)$. Following Buck (2024), we assume the temperature varies linearly with the depth, from T_S on the top surface to $T = T_B$ on the bottom

$$T(z) = T_S - \frac{T_B - T_S}{h}\left(z - \frac{h}{2}\right). \tag{5.18}$$

Substituting Eq. 5.18 into Eq. 5.17, the vertical distribution of viscosity can be approximated using Taylor expansion for $T_B - T_S \ll T_S$

$$\eta\left(\dot{\varepsilon}, z\right) = \eta\left(\dot{\varepsilon}, 0\right)\exp\left(\frac{z - h/2}{z_0}\right) = \eta_s \exp\left(\frac{z - h/2}{z_0}\right), \tag{5.19}$$

where $z_0 = \dfrac{RT_s^2}{Q_0(T_B - T_S)}h$ is the characteristic lengthscale of vertical variations in viscosity, and η_s is the ice viscosity on the top surface. Further assuming vertically uniform strain rate $\dot{\varepsilon} = \text{const}$, the stress distribution is

$$\Delta\sigma\,(z) = \eta\left(\dot{\varepsilon}, z\right)\dot{\varepsilon} = \eta_s \exp\left(\frac{z - h/2}{z_0}\right)\dot{\varepsilon} = \Delta\sigma_s \exp\left(\frac{z - h/2}{z_0}\right), \tag{5.20}$$

where $\Delta\sigma_s = \eta_s\dot{\varepsilon}$ is the tensile resistive stress on the top surface. Integrating Eq. 5.20 across the depth and using the force balance at the calving front gives

$$\Delta\sigma_s = \overline{\Delta\sigma}\left(\frac{h}{z_0}\right)\left[1 - \exp\left(\frac{-h}{z_0}\right)\right]^{-1}. \tag{5.21}$$

Note that $\overline{\Delta\sigma}$ is the uniform tensile resistive stress from Eq. 5.15. Substituting Eq. 5.15 into Eq. 5.21 gives

$$\Delta\sigma_s = \left[\frac{1}{2}\rho_i g h - \frac{1}{2}\rho_w g\left(\frac{\rho_i}{\rho_w}h - w_e\right)^2\right]\left(\frac{h}{z_0}\right)\left[1 - \exp\left(\frac{-h}{z_0}\right)\right]^{-1}. \tag{5.22}$$

Thus we can calculate $\Delta\sigma\,(z)$ by substituting Eq. 5.22 into Eq. 5.20. Combining

with the definition of M_I (Eq. 5.14), $M_I(w_e)$ can be expressed as

$$\begin{aligned} M_I\left(w_e\right) = &-\frac{1}{12}\rho_i g h^3 - \frac{1}{6}\frac{\rho_i^3}{\rho_w^2} g h^3 + \frac{1}{4}\frac{\rho_i^2}{\rho_w} g h^3 + \left(\frac{\rho_i^2}{2\rho_w} - \frac{\rho_i}{2}\right) g h^2 w + \\ &\left(\frac{\rho_w}{4} - \frac{\rho_i}{2}\right) g h w^2 + \frac{1}{6}\rho_w g w^3 + \frac{1}{4}\left[\rho_i g h - \frac{\rho_w g}{h}\left(\frac{\rho_i}{\rho_w} h - w_e\right)^2\right] \\ &\left(\frac{h^3}{z_0}\right)\left[1 - \exp\left(\frac{-h}{z_0}\right)\right]^{-1}\left(1 - 2\frac{z_0}{h} + \exp\frac{-h}{z_0}\left(1 + 2\frac{z_0}{h}\right)\right). \end{aligned} \tag{5.23}$$

When imposed on the edge Eq. 5.23 causes either downward or upward deflection depending on the value of z_0. When the temperature difference $T_B - T_S$ is small, $z_0 \to \infty$, and the stress is nearly vertically uniform, giving $M_I > 0$ and downward deflection at the edge. On the other side, when z_0 is small due to a big temeprature difference, the internal bending moment $M_I < 0$ gives upward deflection.

5.2.5 Numerical implementation

Here we denote the solution at the n-th time step as $\hat{w}_n$. The initial condition is $\hat{w}_0$, and the time step is Δt. We descritise the time integral in Eq. 5.10 and keep the spatial derivative. At time step n, the equation is

$$\frac{\partial^4 \hat{w}_n}{\partial \hat{x}^4} + 4\hat{w}_n + 2\sum_{i=0}^{n-1} \hat{w}_i \Delta t = \frac{\partial \hat{w}_0}{\partial \hat{x}} + 4\hat{w}_0| = 0, \tag{5.24}$$

with boundary conditions

$$\begin{aligned} \frac{\partial^2 \hat{w}_n}{\partial \hat{x}^2} &= \frac{\partial^2 \hat{w}_n}{\partial \hat{x}^2}\left(\hat{t} = 0\right) - \int_0^{\hat{t}} \hat{M}_e d\hat{t}, \quad \hat{x} = 0, \\ \frac{\partial^3 \hat{w}_n}{\partial \hat{x}^3} &= \frac{\partial^3 \hat{w}_n}{\partial \hat{x}^3}\left(\hat{t} = 0\right) - \int_0^{\hat{t}} \hat{Q}_e d\hat{t}, \quad \hat{x} = 0, \\ \hat{w}_n = \frac{\partial \hat{w}_n}{\partial \hat{x}} &= \frac{\partial^2 \hat{w}_n}{\partial \hat{x}^2} = 0, \quad \hat{x} \to \infty. \end{aligned} \tag{5.25}$$

Thus the governing equation is reduced to a boundary value problem at the n-th time step in terms of $\hat{w}_n$. It is solved by the *NDSolve* function in *Mathematica*.

5.3 Results

5.3.1 Viscoelastic bending due to vertically non-uniform viscosity

The viscoelastic bending problem can be solved by numerically integrating Eq. 5.10 over time from an initial state. Here we consider a reference case with only the internal bending moment $M_e = M_I$ from Eq. 5.23 on the shelf edge. The values of parameters used in this case can be found in Table 5.1. In this case, the temperature difference between the top and bottom is large such that $M_I < 0$, causing upward flexure on the edge.

Physical property	Notation	Value
Density of water	ρ_w	1027 kg m^{-3}
Density of ice	ρ_i	917 kg m^{-3}
Length of the domain	L	20 km
Ice thickness	h	200 m
Deflection scale	w_a	1 m
Foot length	l_b	20 m
Foot height	h_b	169 m
Viscosity	η	1.0×10^{15} Pa s
Young's modulus	E	1.1×10^{9} Pa
Poisson's ratio	μ	0.33
Activation energy	Q_0	60 kJ mol^{-1}
Ideal gas constant	R	8.314 J mol^{-1} K^{-1}
Surface temperature	T_S	253.15 K
Basal temperature	T_B	273.15 K

Table 5.1: Parameters and their reference values.

Fig. 5.2 shows the evolution of the deflection. At $t = 0$, the shelf bends as an

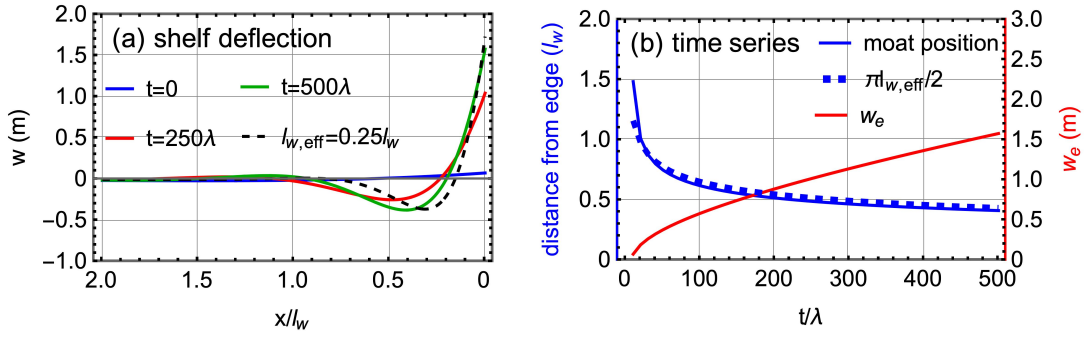

Figure 5.2: **(a)** Shelf deflection profile near the edge at $t = 0, 1000\lambda, 2000\lambda$, and the elastic bending solution with $l_{w,\text{eff}} = 0.25 l_w$. **(b)** The modelled moat position (solid blue) and the approximation according to Eq. 5.27 (dashed blue). Here the x-axis is time scaled by the ice Maxwell time. The y-axis is the distance from the edge. The red line represents the increasing deflection at the ice-shelf edge. Note that for the figures from this point forward, the horizontal axis is flipped compared with Fig. 5.1 to have a natural view of ice-flow direction from the left to the right.

elastic plate with the effective bending lengthscale $l_{w,\text{eff}}$ equal to the elastic bending lengthscale l_w given by Eq. 5.6, followed by viscous creep causing decreasing $l_{w,\text{eff}}$. Fig. 5.2(a) shows the shelf deflection near the edge at $t = 0, 1000\lambda, 2000\lambda$, where $\lambda \approx 9$ d is the Maxwell time of ice. As a result of decreasing $l_{w,\text{eff}}$, the moat gets deeper and moves towards the edge, and the edge deflection w_e increases, forming a rampart–moat profile. The dashed line represents the elastic bending solution Eq. 5.5 with the effective bending lengthscale $l_{w,\text{eff}} = 0.25 l_w$.

In Fig. 5.2(b), we plot the time series of the moat–edge distance and the edge deflection w_e. We calculate the moat position x_{moat} as where w reaches the minimum. According to the elastic solution, $x_{moat} = \frac{\pi}{2} l_w$. For a viscous or viscoelastic thin plate, Reeh (1968) and Olive et al. (2016) found that $l_{w,\text{eff}}$ decreases with time as

$$l_{w,\text{eff}}(t) = \left(\frac{\eta h^3}{\rho_w g t} \right)^{1/4}. \tag{5.26}$$

Therefore, the moat position x_{moat} can be estimated as

$$x_{moat} = \frac{\pi}{2} l_{w,\text{eff}}(t) = \frac{\pi}{2}\left(\frac{\eta h^3}{\rho_w g t}\right)^{1/4}. \tag{5.27}$$

In Fig. 5.2(b), the calculated moat position agrees well with the estimation from Eq. 5.27, and the edge deflection keeps increasing without reaching a steady state, indicating that the edge flexure might keep growing until reaching the calving criterion. We thus investigate the variation in the horizontal tensile stress within the shelf. The bending moment of the shelf can be calculated according to the vertical stress balance $\frac{\partial^2 M}{\partial x^2} + \rho_w g w = 0$, with the boundary conditions

$$\begin{aligned} M &= M_e, \quad x = 0 \\ M &= 0. \quad x = \infty \end{aligned} \tag{5.28}$$

The tensile stress within the thin-plate can be calculated as

$$\sigma_{xx}(x, z) = \frac{M(x) z}{I}, \tag{5.29}$$

which indicates that the maximum tensile stress occurs on the top or bottom surface. The maximum stress stress $|\sigma_{max}|$ is then

$$\sigma_{max} = \frac{\max(|M|)\, h}{2I} = \frac{6\max(|M|)}{h^2}, \tag{5.30}$$

where $\max(|M|)$ is the maximum of $|M|$ within the shelf. In Fig. 5.3(a) we plot the bending moment $M(x)$ profile at $t = 0, 1000\lambda, 2000\lambda$. The bending moment reaches its maximum near the moat, and reaches its minimum at the edge. The maximum stress magnitude $|\sigma_{max}|$ occurs at the edge where $M = M_e$ and increases with time (Fig. 5.3(b)) due to the increasing deflection w_e.

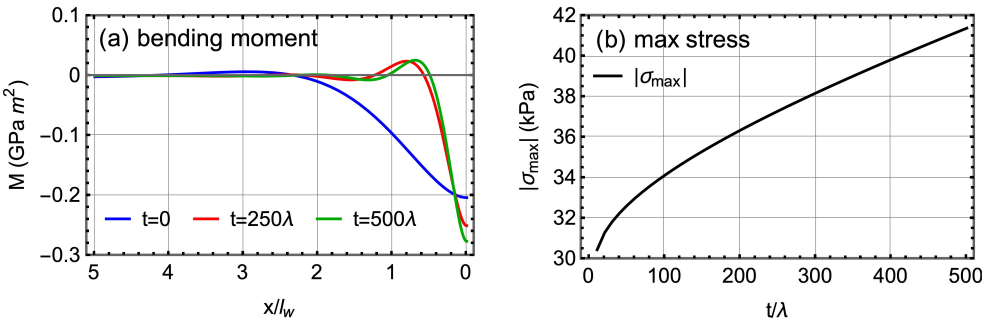

Figure 5.3: **(a)** Bending moment M near the edge at $t = 0, 1000\lambda, 2000\lambda$. **(b)** Evolution of the maximum horizontal stress magnitude $|\sigma_{max}|$.

The model results suggest a possible mechanism for the calving events near the shelf edge: the tensile stress and shelf deflection increase until reaching the calving criterion and causing break-up of ice near the edge. The size of the produced iceberg will provide information about the effective bending scale at the time of calving. But such calving processes can be influenced by non-uniform ice thickness and preexisting crevasses that weaken the strength of the ice shelf.

5.3.2 Viscoelastic bending due to underwater ice foot

In this section we investigate the alternative mechanism for flexure by modelling the effect of the underwater ice foot as well as the imbalance Eq. 5.16 between hydrostatic pressure and water pressure. The underwater ice foot tends to cause upward deflection, while the pressure imbalance between the ocean and ice causes downward deflection. So the total deflection is controlled by the trade-off between the two factors.

We assume that the viscosity is vertically uniform, with an ice foot whose size is given in Table 5.1. The boundary condition is $M_e = M_w$ (Eq. 5.16) and $Q_e =$

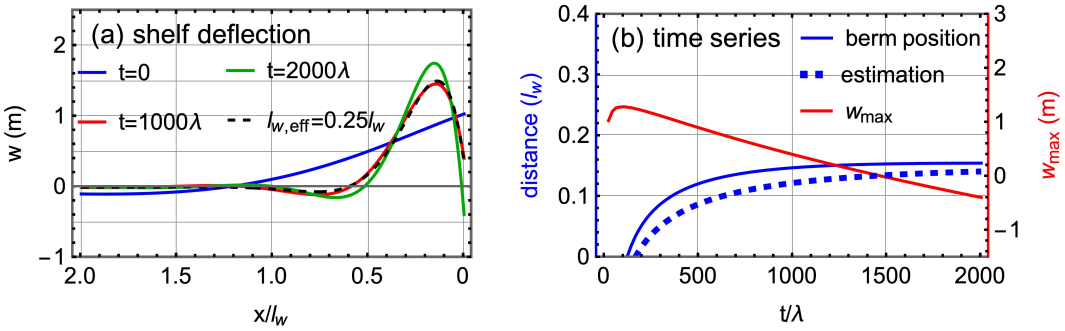

Figure 5.4: **(a)** Shelf deflection profile near the edge at $t = 0,\ 1000\lambda,\ 2000\lambda$. The dashed black line is the elastic solution with an effective bending wavelength of $0.25l_w$, in contrast to the elastic solution with a bending wavelength of l_w as shown by the blue line. **(b)** time series. The solid blue line is where $\partial_x w = 0$. Initially, there is the rampart–moat profile rather than the berm on the ice shelf. The solid blue line represents the position of the moat. As the shelf creeps viscously, the rampart–moat profile transitions to the berm profile. And the blue line represents the berm position. The dashed blue line is the estimated moat/berm position using the elastic solution with a varying $l_{w,eff}$. The red line is the maximum elevation w_{max}. Initially the topographic high occurs on the edge, and then transitions to the top of the berm.

$(\rho_w - \rho_i)gl_b h_b$ on the edge. Assuming M_w is constant, the elastic solution is

$$w\left(x\right) = -\frac{2M_w}{\rho_w g l_w^2}\exp\left(-\frac{x}{l_w}\right)\left[-\sin\left(\frac{x}{l_w}\right) + \left(1 - \frac{(\rho_w - \rho_i)gl_b h_b l_w}{M_w}\right)\cos\left(\frac{x}{l_w}\right)\right]. \tag{5.31}$$

Fig. 5.4 shows the evolution of shelf deflection and relevant time series. Initially there is upward deflection on the edge due to the buoyancy force Q_e provided by the ice foot, which is similar to the rampart–moat profile in Fig. 5.2. Then the upward deflection vanishes by viscous creep and the applied bending moment M_w, forming a berm with a downward-deflected edge. However, the transition is very slow: given the 200m-thick ice with a 20m-long ice foot, it takes 2000λ to form a 2m-high berm. The transition can be explained using the elastic bending solution Eq. 5.31 with a decreasing bending lengthscale $l_{w,\text{eff}}(t)$. According to

Eq. 5.31, the edge deflection $w_e(t)$ can be approximated by

$$w_e(t) = w\left(x,t\right)|_{x=0} = -\frac{2M_w}{\rho_w g l_{w,\text{eff}}^2\left(t\right)}\left(1-\frac{(\rho_w-\rho_i)gl_b h_b l_{w,\text{eff}}\left(t\right)}{M_w}\right), \quad (5.32)$$

where $M_w > 0$. The sign of $w_e(t)$ depends on the value of $1-\frac{(\rho_w-\rho_i)gl_b h_b l_{w,\text{eff}}\left(t\right)}{M_w}$. Assuming that M_w and $\rho_i g l_b h_b$ are fixed, $1-\frac{(\rho_w-\rho_i)gl_b h_b l_{w,\text{eff}}\left(t\right)}{M_w}$ monotonically increases with time as $l_{w,\text{eff}}\left(t\right)$ decreases, which may cause the transition from $w_e(t) > 0$ to $w_e(t) < 0$. Note that this transition doesn't necessarily occur as it depends on the initial value of Eq. 5.32.

The position of the berm (topographic high) in an elastic shelf, denoted by x_b, follows

$$x_b = l_w \arctan\left(\frac{2M_w}{(\rho_w-\rho_i)gl_b h_b l_w}-1\right). \quad (5.33)$$

Thus the berm position $x_b(t)$ in the viscoelastic solution can be approximated as

$$x_b(t) = l_{w,\text{eff}}\left(t\right)\arctan\left(\frac{2M_w}{(\rho_w-\rho_i)gl_b h_b l_{w,\text{eff}}\left(t\right)}-1\right), \quad (5.34)$$

where $l_{w,\text{eff}}\left(t\right)$ follows Eq. 5.26. In Fig. 5.4(b) we show that Eq. 5.34 is a good approximation to the position of the berm extracted from the numerical solution. Initially, the berm quickly goes away from the edge and reaches the maximum distance, followed by a slow decrease in the distance. The berm–edge distance can be a metric to help constrain the viscoelastic models and make comparisons with the observed ice surface profiles.

In Fig. 5.5 we plot the bending moment $M(x)$ (Fig. 5.5(a)) and the maximum stress magnitude on the shelf (Fig. 5.5(b)) (occurring on the edge in this case). Bending moment around the berm within the shelf decreases with time, with the edge value $M_e = M_w(w_e)$ staying close to the initial condition. Thus the corre-

sponding stress at the edge also remains close to the elastic solution.

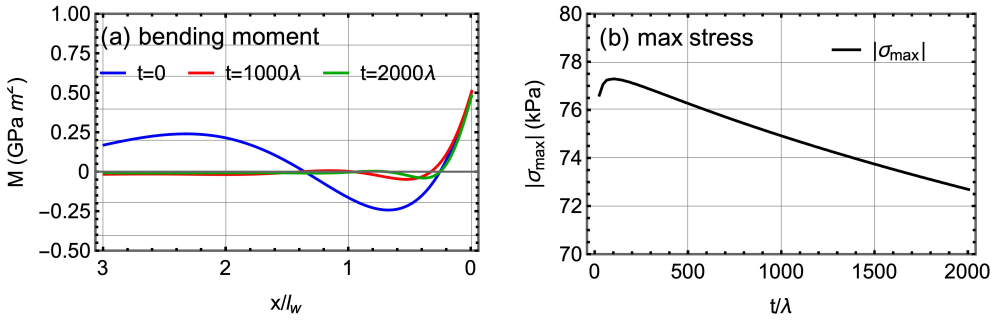

Figure 5.5: **(a)** Bending moment M near the edge at $t = 0, 1000\lambda, 2000\lambda$. **(b)** Evolution of the maximum horizontal stress magnitude $|\sigma_{max}|$. In this case $|\sigma_{max}|$ occurs on the edge.

5.4 Discussion

5.4.1 Comparison with observations at the Ross Ice Shelf

We modelled the viscoelastic flexure near the shelf edge using a simplified, linear Maxwell constitutive law. The results align with previous models, showing increasing ice deflection and a decreasing effective bending lengthscale due to viscous creep. To explain the observations of the edge deflection profile, we compare the results from two different hypotheses: vertically non-uniform viscosity and underwater ice feet. The two models yield different flexure profiles. In this section, we compare the modelled deflection profile with the observations from Sartore et al. (2024).

5.4.1.1 Vertically non-uniform viscosity

We first consider the vertically non-uniform viscosity as the cause of edge deflection. Note that a key parameter of such a rampart-moat profile or a berm profile

is the elevation difference between the topographic high and the topographic low, based on which we can conduct the model-data comparison. We first perform coordinate translation on the data such that the observed topographic high overlaps with the modelled one. We use the model results from the reference case, where the surface temperature is $-20°$C with no underwater ice feet. All values of parameters are the same as Table 5.1.

In Fig. 5.6, we plot the observed surface elevation profiles at 10/2003 and 02/2006. There is approximately 2.3yr between the time of the two observations. The modelled deflection profiles that are close to the observed elevation difference are at $t = 400\lambda$ and $t = 600\lambda$, respectively.

Note that we have shifted the data to match the topographic high with the modelled deflection profiles. However, the observed surface elevation profile has a steep downward slope towards the edge, which is absent from the modelled rampart profile. Instead, it can be a consequence of a berm profile caused by underwater ice feet, which we will consider in the following section.

5.4.1.2 Underwater ice feet

Here we compare the same observations with the modelled deflection profile with an underwater foot. The model results are from the reference case with the underwater foot. The observations are still shifted such that the topographic high overlaps with the modelled berm. At $t = 500\lambda$ and $t = 2000\lambda$, the elevation differences in the model results are close to the observations at 10/2003 and 02/2006, respectively.

As shown in Fig. 5.7, the modelled ice deflection not only matches the observation in the elevation difference but also has a similar downward slope towards the edge, indicating that the observed profile could be a berm caused by viscous creep.

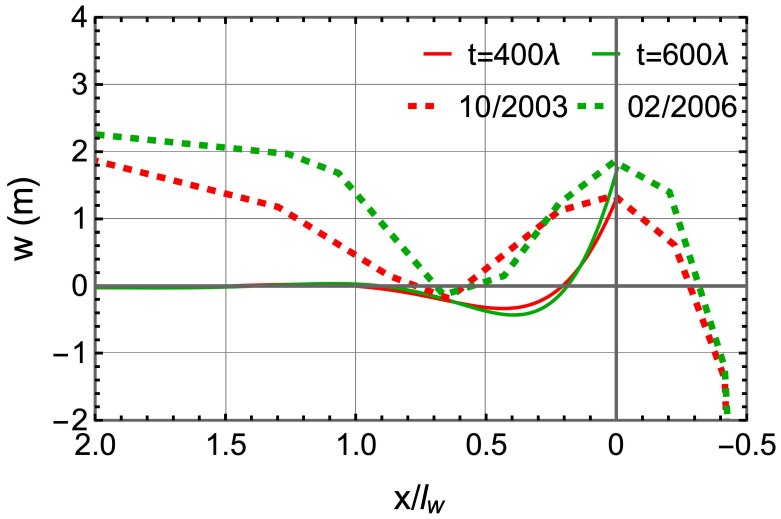

Figure 5.6: Comparison between the modelled ice deflection with vertically non-uniform viscosity and the observation at the Ross Ice Shelf (Sartore et al., 2024). The solid lines represent the modelled surface elevation at $t = 400\lambda$ (red) and $t = 600\lambda$ (green). The dashed lines are observed surface elevation profiles, which are shifted such that the topographic high is aligned with the modelled one.

However, this requires further investigation of the ICESat data. Meanwhile, the time interval between the two modelled profiles is about 1500λ. Given the typical ice Maxwell time is about several days, this is much larger than the observed time interval.

By comparing the model results with data from Sartore et al. (2024), we find that both mechanisms can produce part of the observed deflection near the edge of the Ross Ice Shelf. However, the growing rate of the deflection and surface slope towards the edge are different between the two mechanisms. Further analysis of the data is required to determine the real cause of the observed growing deflection profiles.

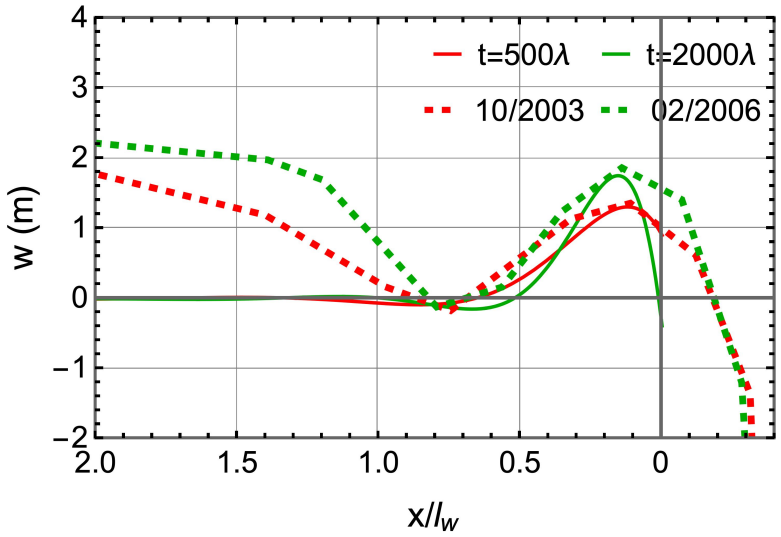

Figure 5.7: Comparison between the modelled ice deflection with an underwater ice foot and the observation at the Ross Ice Shelf (Sartore et al., 2024). The solid lines represent the modelled surface elevation at $t = 500\lambda$ (red) and $t = 2000\lambda$ (green). The dashed lines are observed surface elevation profiles, which are shifted such that the topographic high is aligned with the modelled one.

5.4.2 Limitations

This model has some limitations due to simplification. In the viscoelastic flexure model, although we considered the bending moment caused by vertically non-uniform viscosity, we use a constant viscosity when setting up the governing equation for flexure. For a real ice shelf bending near its edge, the viscosity should depend on the flexural strain and the vertical temperature profile as shown in Eq. 5.17. Meanwhile, when deriving the additional stress $\Delta\sigma$ in Eq. 5.20, we have assumed that the strain rate is vertically uniform in upstream ice shelves. However, given the vertically non-uniform ice viscosity, the upstream strain rate should also be depth-dependent. This could be solved by considering the vertically non-uniform viscosity in the thin-plate model Eq. 5.7.

The buoyancy force of ice feet scales linearly with the foot size. However, the

length of the underwater ice foot is poorly constrained when setting up the reference case by using an arbitrary lengthscale. In a real ice shelf, foot growth and viscous creep occur simultaneously, highlighting the necessity to incorporate the evolution of ice feet into the model. Since directly observing the size of underwater ice feet is challenging, one potential improvement could be to trace medium-sized icebergs that calve through the foot-bending mechanism.

To predict calving events, a fracturing criterion, such as a yield strength σ_Y or a LEFM model of fracture propagation is required to be combined with the modelled stress field (Sartore et al., 2024). For the case with underwater ice feet, the stress is complicated and consists of both the flexural tensile stress and the shearing force, which can cause mixed-mode fracture propagation near the edge Tada et al. (2000).

Therefore, Glen's flow law (Glen, 1955) should be used to calculate the viscosity related to ice flexure. Thus we make more accurate predictions of the surface elevation, which can be compared with the observed elevation profile. A fracturing criterion should be introduced to predict calving. For observations, more constraints on the size of the underwater ice feet are required to better account for their effect.

5.5 Conclusion

We have shown that viscoelastic flexure can explain the formation of both the "rampart–moat" and "berm" profiles observed at the edges of ice shelves. By comparing the results from two different hypotheses, we find that for a vertically non-uniform ice shelf, stress and deflection at the edge increase over time, leading to the formation of a rampart. In contrast, for an ice shelf with an underwater ice foot, the edge exhibits an initial upward deflection that transitions to downward

deflection, resulting in the formation of a berm. This change occurs due to the decreasing effective bending lengthscale caused by viscous creep. Our model serves as a preliminary approach to studying the evolution of the surface profiles and related calving events near the shelf edge. The model's prediction offers a new perspective for distinguishing between flexure profiles driven by these two different mechanisms.

6 | Conclusion

Using numerical models and geospatial data, I investigated the mechanics of fracture and flexure in the Antarctic Ice Sheet and ice shelves.

In grounded ice sheets, basal ice is subject to spatially non-uniform basal conditions such as soft and hard bed, influenced by varying subglacial hydrology and basal topography. The sticky patches can create excess tensile stress on the ice–bed interface, which promotes hydrofracturing. I modelled the mixed-mode fracture propagation near a sticky patch and explored the parameters controlling these hydrofracturing processes. The results showed that the size of sticky patches and the magnitude of excess shear stress together control the propagation of basal hydrofractures. For sticky patches larger than the local ice thickness, vertical fracturing is more likely to occur. In contrast, for sticky patches whose size is smaller or comparable to the local ice thickness, propagation of nearby basal hydrofractures deviates from previous mode-I assumptions. The crack trajectories tend to align upstream and can be approximated by the principal stress trajectories. This reflects the influence of localised stress fields generated by the sticky patch on fracture propagation. The fractures and their thermal effects can be parameterised in large-scale ice-flow models by utilizing the principal stress trajectories and the analytical solutions provided in our discussion. This approach would allow for a more accurate representation of fracture propagation and the associated thermal impact within Antarctic Ice Sheet, enhancing the predictive capabilities of large-scale models.

In the grounding zone, flexure and fracture are caused by the tidally modulated grounding line migration. Tidal flexure can induce supraglacial lake drainage through hydrofracturing. I modelled the viscoelastic mechanics of tidally-induced

grounding line migration using Full-Stokes model. Using LEFM, I have investigated the dependency of tidally induced drainage events on the ocean tidal amplitude. The relationship between the tidal amplitude and lake depth aligns with remotely sensed data analysis, highlighting the significant role of ocean tides in driving hydrofracturing in the grounding zone. Furthermore, sensitivity analysis of the model results underscores the necessity of using viscoelastic rheology in modelling tidal grounding line dynamics, particularly for estimating the magnitude of flexural stress and the width of the grounding zone. The elastic model tends to underestimate both the magnitude of tidally induced tensile stress and the grounding-zone width, while the viscous model overestimates them. The dependence of the grounding line dynamics on ice rheology have implications for large-scale modelling. The viscoelastic flexure model is necessary to obtain an accurate estimate of tidally induced stress when considering fracturing in the grounding zone. In addition, elastic or viscous representations of grounding-line migration could be improved.

In the next chapter, instead of using full-Stokes simulations, I modelled the viscoelastic tidal flexure in the grounding zone using a depth-integrated flow line model. This framework retains the crucial aspect of viscoelastic flexure for the grounding line while avoiding the complexity of the full-Stokes model. It can be used to investigate the mechanisms behind different nonlinear tidal responses at Antarctic ice streams. The results show that the nonlinear basal sliding law with viscoelastic flexure near the grounding line can cause nonlinear tidal responses, which is in agreement with previous results from full-Stokes models. The relative importance of fortnightly variations is controlled by the ratio of the tidal period to the Maxwell time of ice: fortnightly variations dominate only when the ice is sufficiently viscous over the tidal period.

In addition to the grounding zone, flexure and fracture also occur on ice shelves.

These processes are usually associated with calving, rifting, and ice-shelf disintegration. To better understand this, I focus on the edge of ice shelves: Using viscoelastic thin-plate theory, I modelled the flexure due to vertically non-uniform temperature and underwater ice foot. The viscoelastic ice shelf edge is characterised by a decreasing effective bending lengthscale and an increasing deflection magnitude near ice shelf edges, which is in agreement with previous studies. In specific, the vertically non-uniform viscosity could cause a growing rampart–moat profile with an increasing edge deflection. The underwater ice foot can induce similar rampart–moat profile when the flexure is mainly elastic, which transitions to a growing berm profile under the effect of viscous creep caused by stress imbalance. The growing berm profile is qualitatively consistent with the observations of the surface elevation profiles at the Ross Ice Shelf calving front. The above difference between the two mechanisms can be used to determine the controlling mechanism at a specific ice shelf. However, the model needs to be further developed to include nonlinear ice viscosity. In addition, it could be further expanded with a calving criterion to make testable predictions of the deflection profile and related calving events. Previous calving laws based on elastic flexure models could be further improved.

Further study is required to understand the mechanisms of flexure and fracture of ice, particularly in the grounding zone and near the calving front. In chapter 3 and chapter 4, we have shown that viscoelasticity plays an important role in tidally modulated grounding-line dynamics. However, most studies on viscoelastic grounding line and ice flexure are numerical. The role of viscoelasticity in ice flexure is still not fully understood. Therefore, analytical or semi-analytical models could be developed to gain mechanistic understanding of viscoelastic ice flexure, and how it could be parameterised in large-scale ice shelf models without complicated numerical treatment. Given the sensitivity of the grounding zone

to ice rheology, further remotely-sensed observations of the tidal grounding zone width would help to better constrain the Maxwell time of ice, which is a dominant control on the viscoelastic ice flexure.

In chapter 5, we have calculated the viscoelastic flexure under two different mechanisms. Our results have shown that the flexure at ice shelf edges is growing with time, which indicates that models of calving fronts should incorporate the effect of viscous creep when predicting the surface elevation profiles and fracturing. In addition, we have found that shelf edges that are subject to both the ice foot and stress imbalance could transition from a rampart–moat profile to a berm profile, which is different from edges subject to non-uniform viscosity. This difference can be used to find the controlling mechanism of flexure near ice shelf edges. In the future, the model needs to be improved by incorporating non-Newtonian viscosity and a spatially non-uniform thickness profile, which enables comparison with more complicated numerical models. Meanwhile, the model could be expanded with a fracturing criterion, and thus make testable predictions of calving events. Currently, the main uncertainty of the model comes from the size of the underwater foot, which is difficult to observe directly from satellite images. Instead, it could be better constrained by tracing medium-sized icebergs or in-situ field measurements.

Flexure and fracture are crucial factors influencing both the grounded ice sheets and floating ice shelves in Antarctica. By integrating mathematical models with geospatial analysis, this thesis offers new insights into the mechanics of flexure and fracture, and their relationship with spatially-varying basal conditions, tidal variations and viscoelastic rheology. The findings have important implications for large-scale modelling.

Bibliography

Alley, R. B., Horgan, H. J., Joughin, I., Cuffey, K. M., Dupont, T. K., Parizek, B. R., Anandakrishnan, S., and Bassis, J. (2008). A simple law for ice-shelf calving. *Science*, 322(5906):1344–1344.

Anandakrishnan, S., Voigt, D., Alley, R., and King, M. (2003). Ice stream D flow speed is strongly modulated by the tide beneath the Ross Ice Shelf. *Geophysical Research Letters*, 30(7).

Anandakrishnan, S. and Winberry, J. (2004). Antarctic subglacial sedimentary layer thickness from receiver function analysis. *Global and Planetary Change*, 42(1-4):167–176.

Andrews, L. C., Catania, G. A., Hoffman, M. J., Gulley, J. D., Lüthi, M. P., Ryser, C., Hawley, R. L., and Neumann, T. A. (2014). Direct observations of evolving subglacial drainage beneath the Greenland Ice Sheet. *Nature*, 514(7520):80–83.

Balay, S., Abhyankar, S., Adams, M. F., Benson, S., Brown, J., Brune, P., Buschelman, K., Constantinescu, E., Dalcin, L., Dener, A., Eijkhout, V., Faibussowitsch, J., Gropp, W. D., Hapla, V., Isaac, T., Jolivet, P., Karpeev, D., Kaushik, D., Knepley, M. G., Kong, F., Kruger, S., May, D. A., McInnes, L. C., Mills, R. T., Mitchell, L., Munson, T., Roman, J. E., Rupp, K., Sanan, P., Sarich, J., Smith, B. F., Suh, H., Zampini, S., Zhang, H., Zhang, H., and Zhang, J. (2024a). PETSc/TAO users manual. Technical Report ANL-21/39 - Revision 3.22, Argonne National Laboratory.

Balay, S., Abhyankar, S., Adams, M. F., Benson, S., Brown, J., Brune, P., Buschelman, K., Constantinescu, E. M., Dalcin, L., Dener, A., Eijkhout, V., Faibussowitsch, J., Gropp, W. D., Hapla, V., Isaac, T., Jolivet, P., Karpeev, D., Kaushik,

D., Knepley, M. G., Kong, F., Kruger, S., May, D. A., McInnes, L. C., Mills, R. T., Mitchell, L., Munson, T., Roman, J. E., Rupp, K., Sanan, P., Sarich, J., Smith, B. F., Zampini, S., Zhang, H., Zhang, H., and Zhang, J. (2024b). PETSc Web page. https://petsc.org/.

Balay, S., Gropp, W. D., McInnes, L. C., and Smith, B. F. (1997). Efficient Management of Parallelism in Object Oriented Numerical Software Libraries. In Arge, E., Bruaset, A. M., and Langtangen, H. P., editors, *Modern Software Tools in Scientific Computing*, pages 163–202. Birkhäuser Press.

Banks-Sills, L. and Sherman, D. (1986). Comparison of methods for calculating stress intensity factors with quarter-point elements. *International Journal of Fracture*, 32(2):127–140.

Banwell, A. F., MacAyeal, D. R., and Sergienko, O. V. (2013). Breakup of the Larsen B Ice Shelf triggered by chain reaction drainage of supraglacial lakes. *Geophysical Research Letters*, 40(22):5872–5876.

Banwell, A. F., Willis, I. C., Macdonald, G. J., Goodsell, B., and MacAyeal, D. R. (2019). Direct measurements of ice-shelf flexure caused by surface meltwater ponding and drainage. *Nature communications*, 10(1):730.

Banwell, A. F., Willis, I. C., Stevens, L. A., Dell, R. L., and MacAyeal, D. R. (2024). Observed meltwater-induced flexure and fracture at a doline on George VI Ice Shelf, Antarctica. *Journal of Glaciology*, pages 1–14.

Bassis, J. N. and Jacobs, S. (2013). Diverse calving patterns linked to glacier geometry. *Nature Geoscience*, 6(10):833–836.

Bassis, J. N. and Ma, Y. (2015). Evolution of basal crevasses links ice shelf stability to ocean forcing. *Earth and Planetary Science Letters*, 409:203–211.

Berg, B. and Bassis, J. (2022). Crevasse advection increases glacier calving. *Journal of Glaciology*, pages 1–10.

Bindschadler, R. A., King, M. A., Alley, R. B., Anandakrishnan, S., and Padman, L. (2003). Tidally controlled stick-slip discharge of a West Antarctic ice. *Science*, 301(5636):1087–1089.

Borstad, C., Khazendar, A., Larour, E., Morlighem, M., Rignot, E., Schodlok, M., and Seroussi, H. (2012). A damage mechanics assessment of the Larsen B ice shelf prior to collapse: Toward a physically-based calving law. *Geophysical Research Letters*, 39(18).

Brædstrup, C., Egholm, D., Ugelvig, S., and Pedersen, V. (2016). Basal shear stress under alpine glaciers: insights from experiments using the iSOSIA and Elmer/Ice models. *Earth Surface Dynamics*, 4(1):159–174.

Broek, D. (1982). *Elementary Engineering Fracture Mechanics*. Springer Science & Business Media.

Buck, W. R. (2024). The effect of ice rheology on shelf edge bending. *EGUsphere*, 2024:1–17.

Buck, W. R. and Lai, C.-Y. (2021). Flexural control of basal crevasse opening under ice shelves. *Geophysical Research Letters*, 48(8):e2021GL093110.

Budd, W., Keage, P., and Blundy, N. (1979). Empirical studies of ice sliding. *Journal of glaciology*, 23(89):157–170.

Carslaw, H. S. and Jaeger, J. C. (1959). *Conduction of Heat in Solids*. Clarendon P Oxford, United Kingdom.

Cathles, L. M. (2015). *Viscosity of the Earth's mantle*. Princeton University Press.

Chan, S., Tuba, I., and Wilson, W. (1970). On the finite element method in linear fracture mechanics. *Engineering Fracture Mechanics*, 2(1):1–17.

Chen, H., Rignot, E., Scheuchl, B., and Ehrenfeucht, S. (2023). Grounding Zone of Amery Ice Shelf, Antarctica, From Differential Synthetic-Aperture Radar Interferometry. *Geophysical Research Letters*, 50(6):e2022GL102430.

Cheng, G., Lötstedt, P., and von Sydow, L. (2020). A full Stokes subgrid scheme in two dimensions for simulation of grounding line migration in ice sheets using Elmer/ICE (v8. 3). *Geoscientific Model Development*, 13(5):2245–2258.

Christmann, J., Mueller, R., and Humbert, A. (2019). On nonlinear strain theory for a viscoelastic material model and its implications for calving of ice shelves. *Journal of Glaciology*, 65(250):212–224.

Christmann, J., Plate, C., Müller, R., and Humbert, A. (2016). Viscous and viscoelastic stress states at the calving front of Antarctic ice shelves. *Annals of Glaciology*, 57(73):10–18.

Colleoni, F., De Santis, L., Siddoway, C. S., Bergamasco, A., Golledge, N. R., Lohmann, G., Passchier, S., and Siegert, M. J. (2018). Spatio-temporal variability of processes across Antarctic ice-bed–ocean interfaces. *Nature Communications*, 9(1):2289.

Crouch, S. L. and Starfield, A. (1982). *Boundary Element Methods in Solid Mechanics: with applications in rock mechanics and geological engineering*. Allen & Unwin.

Cuffey, K. M. and Paterson, W. S. B. (2010). *The physics of glaciers*. Academic Press.

Dahm, T. (2000). Numerical simulations of the propagation path and the ar-

rest of fluid-filled fractures in the Earth. *Geophysical Journal International*, 141(3):623–638.

Daniels, K. A., Bastow, I., Keir, D., Sparks, R., and Menand, T. (2014). Thermal models of dyke intrusion during development of continent–ocean transition. *Earth and Planetary Science Letters*, 385:145–153.

Das, S. B., Joughin, I., Behn, M. D., Howat, I. M., King, M. A., Lizarralde, D., and Bhatia, M. P. (2008). Fracture propagation to the base of the Greenland Ice Sheet during supraglacial lake drainage. *Science*, 320(5877):778–781.

Davis, T. (2017). A new open source boundary element code and its application to geological deformation: exploring stress concentrations around voids and the effects of corrugation orientation on fault slip in 3D. Master's thesis, Aberdeen University.

de Diego, G. G., Farrell, P. E., and Hewitt, I. J. (2022). Numerical approximation of viscous contact problems applied to glacial sliding, volume=938. *Journal of Fluid Mechanics*, page A21.

Depoorter, M. A., Bamber, J. L., Griggs, J. A., Lenaerts, J. T., Ligtenberg, S. R., van den Broeke, M. R., and Moholdt, G. (2013). Calving fluxes and basal melt rates of Antarctic ice shelves. *Nature*, 502(7469):89–92.

Doyle, S. H., Hubbard, A. L., Dow, C. F., Jones, G. A., Fitzpatrick, A., Gusmeroli, A., Kulessa, B., Lindback, K., Pettersson, R., and Box, J. E. (2013). Ice tectonic deformation during the rapid in situ drainage of a supraglacial lake on the Greenland Ice Sheet. *The Cryosphere*, 7(1):129–140.

Drews, R., Wild, C. T., Marsh, O. J., Rack, W., Ehlers, T. A., Neckel, N., and Helm, V. (2021). Grounding-Zone Flow Variability of Priestley

Glacier, Antarctica, in a Diurnal Tidal Regime. *Geophysical Research Letters*, 48(20):e2021GL093853.

Dunmire, D., Lenaerts, J., Banwell, A., Wever, N., Shragge, J., Lhermitte, S., Drews, R., Pattyn, F., Hansen, J., Willis, I., et al. (2020). Observations of buried lake drainage on the Antarctic Ice Sheet. *Geophysical research letters*, 47(15):e2020GL087970.

Durand, G., Gagliardini, O., De Fleurian, B., Zwinger, T., and Le Meur, E. (2009). Marine ice sheet dynamics: Hysteresis and neutral equilibrium. *Journal of Geophysical Research: Earth Surface*, 114(F3).

Engelhardt, H., Humphrey, N., Kamb, B., and Fahnestock, M. (1990). Physical conditions at the base of a fast moving Antarctic ice stream. *Science*, 248(4951):57–59.

Favier, L., Gagliardini, O., Durand, G., and Zwinger, T. (2012). A three-dimensional full Stokes model of the grounding line dynamics: effect of a pinning point beneath the ice shelf. *The Cryosphere*, 6(1):101–112.

Fretwell, P., Pritchard, H. D., Vaughan, D. G., Bamber, J. L., Barrand, N. E., Bell, R., Bianchi, C., Bingham, R. G., Blankenship, D. D., Casassa, G., Catania, G., Callens, D., Conway, H., Cook, A. J., Corr, H. F. J., Damaske, D., Damm, V., Ferraccioli, F., Forsberg, R., Fujita, S., Gim, Y., Gogineni, P., Griggs, J. A., Hindmarsh, R. C. A., Holmlund, P., Holt, J. W., Jacobel, R. W., Jenkins, A., Jokat, W., Jordan, T., King, E. C., Kohler, J., Krabill, W., Riger-Kusk, M., Langley, K. A., Leitchenkov, G., Leuschen, C., Luyendyk, B. P., Matsuoka, K., Mouginot, J., Nitsche, F. O., Nogi, Y., Nost, O. A., Popov, S. V., Rignot, E., Rippin, D. M., Rivera, A., Roberts, J., Ross, N., Siegert, M. J., Smith, A. M., Steinhage, D., Studinger, M., Sun, B., Tinto, B. K., Welch, B. C., Wilson, D., Young, D. A., Xiangbin, C., and Zirizzotti, A. (2013). Bedmap2: improved ice

bed, surface and thickness datasets for Antarctica. *The Cryosphere*, 7(1):375–393.

Fricker, H. A., Young, N. W., Allison, I., and Coleman, R. (2002). Iceberg calving from the Amery Ice Shelf, East Antarctica. *Annals of Glaciology*, 34:241–246.

Geuzaine, C. and Remacle, J.-F. (2009). Gmsh: A 3-D finite element mesh generator with built-in pre-and post-processing facilities. *International Journal for Numerical Methods in engineering*, 79(11):1309–1331.

Glasser, N. F. and Scambos, T. (2008). A structural glaciological analysis of the 2002 Larsen B ice-shelf collapse. *Journal of Glaciology*, 54(184):3–16.

Glen, J. W. (1955). The creep of polycrystalline ice. *Proceedings of the Royal Society of London. Series A. Mathematical and Physical Sciences*, 228(1175):519–538.

Gow, A., Meese, D., Alley, R., Fitzpatrick, J., Anandakrishnan, S., Woods, G., and Elder, B. (1997). Physical and structural properties of the Greenland Ice Sheet Project 2 ice core: A review. *Journal of Geophysical Research: Oceans*, 102(C12):26559–26575.

Gudmundsson, G. H. (2006). Fortnightly variations in the flow velocity of Rutford Ice Stream, West Antarctica. *Nature*, 444(7122):1063–1064.

Gudmundsson, G. H. (2007). Tides and the flow of Rutford Ice Stream, West Antarctica. *Journal of Geophysical Research: Earth Surface*, 112(F4).

Gudmundsson, G. H. (2011). Ice-stream response to ocean tides and the form of the basal sliding law. *The Cryosphere*, 5(1):259–270.

Gudmundsson, G. H., Krug, J., Durand, G., Favier, L., and Gagliardini, O.

(2012). The stability of grounding lines on retrograde slopes. *The Cryosphere*, 6(6):1497–1505.

Guinea, G. V., Planas, J., and Elices, M. (2000). KI evaluation by the displacement extrapolation technique. *Engineering fracture mechanics*, 66(3):243–255.

Harper, J. T., Bradford, J. H., Humphrey, N. F., and Meierbachtol, T. W. (2010). Vertical extension of the subglacial drainage system into basal crevasses. *Nature*, 467(7315):579–582.

Harper, J. T., Humphrey, N. F., Pfeffer, W. T., Fudge, T., and O'Neel, S. (2005). Evolution of subglacial water pressure along a glacier's length. *Annals of Glaciology*, 40:31–36.

Haseloff, M. and Sergienko, O. V. (2022). Effects of calving and submarine melting on steady states and stability of buttressed marine ice sheets. *Journal of Glaciology*, 68(272):1149–1166.

Heinert, M. and Riedel, B. (2007). Parametric modelling of the geometrical ice-ocean interaction in the Ekstroemisen grounding zone based on short time-series. *Geophysical Journal International*, 169(2):407–420.

Helanow, C. and Ahlkrona, J. (2018). Stabilized equal low-order finite elements in ice sheet modeling–accuracy and robustness. *Computational Geosciences*, 22:951–974.

Helmstetter, A., Moreau, L., Nicolas, B., Comon, P., and Gay, M. (2015). Intermediate-depth icequakes and harmonic tremor in an Alpine glacier (Glacier d'Argentière, France): Evidence for hydraulic fracturing? *Journal of Geophysical Research: Earth Surface*, 120(3):402–416.

Hewitt, I. (2013). Seasonal changes in ice sheet motion due to melt water lubrication. *Earth and Planetary Science Letters*, 371-372:16–25.

Hindmarsh, R. C. (2012). An observationally validated theory of viscous flow dynamics at the ice-shelf calving front. *Journal of Glaciology*, 58(208):375–387.

Howard, S., Padman, L., and Erofeeva, S. (2019). Cats2008: Circum-antarctic tidal simulation version 2008. *United States Antarctic Program Data Center*, 10:601235.

Hudson, T. S., Brisbourne, A. M., White, R. S., Kendall, J.-M., Arthern, R., and Smith, A. M. (2020). Breaking the ice: Identifying hydraulically forced crevassing. *Geophysical Research Letters*, 47(21):e2020GL090597.

Hulbe, C. L., LeDOUX, C., and Cruikshank, K. (2010). Propagation of long fractures in the Ronne Ice Shelf, Antarctica, investigated using a numerical model of fracture propagation. *Journal of Glaciology*, 56(197):459–472.

Jarvis, G. T. and Clarke, G. K. (1974). Thermal effects of crevassing on Steele glacier, Yukon Territory, Canada. *Journal of Glaciology*, 13(68):243–254.

Jimenez, S. and Duddu, R. (2018). On the evaluation of the stress intensity factor in calving models using linear elastic fracture mechanics. *Journal of Glaciology*, 64(247):759–770.

Joughin, I., MacAyeal, D. R., and Tulaczyk, S. (2004). Basal shear stress of the Ross ice streams from control method inversions. *Journal of Geophysical Research: Solid Earth*, 109(B9).

Jouvet, G. and Rappaz, J. (2011). Analysis and finite element approximation of a nonlinear stationary Stokes problem arising in glaciology. *Advances in Numerical Analysis*, 2011.

Katz, R. F. and Worster, M. G. (2010). Stability of ice-sheet grounding lines.

Proceedings of the Royal Society A: Mathematical, Physical and Engineering Sciences, 466(2118):1597–1620.

Kikuchi, N. and Oden, J. T. (1988). *Contact problems in elasticity: a study of variational inequalities and finite element methods*. SIAM.

Krug, J., Weiss, J., Gagliardini, O., and Durand, G. (2014). Combining damage and fracture mechanics to model calving. *The Cryosphere*, 8(6):2101–2117.

Kufner, S.-K., Brisbourne, A. M., Smith, A. M., Hudson, T. S., Murray, T., Schlegel, R., Kendall, J. M., Anandakrishnan, S., and Lee, I. (2021). Not all icequakes are created equal: Basal icequakes suggest diverse bed deformation mechanisms at Rutford Ice Stream, West Antarctica. *Journal of Geophysical Research: Earth Surface*, 126(3):e2020JF006001.

Kyrke-Smith, T., Katz, R., and Fowler, A. (2014). Subglacial hydrology and the formation of ice streams. *Proceedings of the Royal Society A: Mathematical, Physical and Engineering Sciences*, 470(2161):20130494.

Lai, C.-Y., Kingslake, J., Wearing, M., Chen, P.-H. C., Gentine, P., Li, H., Spergel, J. J., and van Wessem, J. M. (2020). Vulnerability of Antarctica's ice shelves to meltwater-driven fracture. *Nature*, 584(7822):574–578.

Langtangen, H. P. and Logg, A. (2017). *Solving PDEs in Python*. Springer.

Law, R., Christoffersen, P., Hubbard, B., Doyle, S. H., Chudley, T. R., Schoonman, C. M., Bougamont, M., des Tombe, B., Schilperoort, B., Kechavarzi, C., et al. (2021). Thermodynamics of a fast-moving Greenlandic outlet glacier revealed by fiber-optic distributed temperature sensing. *Science Advances*, 7(20):eabe7136.

Lazzara, M., Jezek, K., Scambos, T., MacAyeal, D. R., and Van der Veen, C. J.

(1999). On the recent calving of icebergs from the Ross Ice Shelf. *Polar Geography*, 23(3):201–212.

Leeson, A., Shepherd, A., Briggs, K., Howat, I., Fettweis, X., Morlighem, M., and Rignot, E. (2015). Supraglacial lakes on the Greenland ice sheet advance inland under warming climate. *Nature Climate Change*, 5(1):51–55.

Lhermitte, S., Sun, S., Shuman, C., Wouters, B., Pattyn, F., Wuite, J., Berthier, E., and Nagler, T. (2020). Damage accelerates ice shelf instability and mass loss in Amundsen Sea Embayment. *Proceedings of the National Academy of Sciences*, 117(40):24735–24741.

Li, X., Rignot, E., Morlighem, M., Mouginot, J., and Scheuchl, B. (2015). Grounding line retreat of Totten Glacier, East Antarctica, 1996 to 2013. *Geophysical Research Letters*, 42(19):8049–8056.

Lipovsky, B. P. (2020). Ice shelf rift propagation: stability, three-dimensional effects, and the role of marginal weakening. *The Cryosphere*, 14(5):1673–1683.

Lipovsky, B. P., Meyer, C. R., Zoet, L. K., McCarthy, C., Hansen, D. D., Rempel, A. W., and Gimbert, F. (2019). Glacier sliding, seismicity and sediment entrainment. *Annals of Glaciology*, 60(79):182–192.

Logg, A., Mardal, K.-A., and Wells, G., editors (2012). *Automated Solution of Differential Equations by the Finite Element Method*, volume 84 of *Lecture Notes in Computational Science and Engineering*. Springer.

Logg, A. and Wells, G. N. (2010). DOLFIN: Automated finite element computing. *ACM Transactions on Mathematical Software (TOMS)*, 37(2):1–28.

Luckman, A., Jansen, D., Kulessa, B., King, E., Sammonds, P., and Benn, D. (2012). Basal crevasses in Larsen C Ice Shelf and implications for their global abundance. *The Cryosphere*, 6(1):113–123.

Luthra, T., Anandakrishnan, S., Winberry, J. P., Alley, R. B., and Holschuh, N. (2016). Basal characteristics of the main sticky spot on the ice plain of Whillans Ice Stream, Antarctica. *Earth and Planetary Science Letters*, 440:12–19.

MacAyeal, D. R. (1989). Large-scale ice flow over a viscous basal sediment: Theory and application to ice stream B, Antarctica. *Journal of Geophysical Research: Solid Earth*, 94(B4):4071–4087.

MacAyeal, D. R. and Sergienko, O. V. (2013). The flexural dynamics of melting ice shelves. *Annals of Glaciology*, 54(63):1–10.

MacAyeal, D. R., Sergienko, O. V., Banwell, A. F., Macdonald, G. J., Willis, I. C., and Stevens, L. A. (2021). Treatment of ice-shelf evolution combining flow and flexure. *Journal of Glaciology*, 67(265):885–902.

Marsh, O., Rack, W., Floricioiu, D., Golledge, N. R., and Lawson, W. (2013). Tidally induced velocity variations of the Beardmore Glacier, Antarctica, and their representation in satellite measurements of ice velocity. *The Cryosphere*, 7(5):1375–1384.

McCarthy, C., Savage, H., and Nettles, M. (2017). Temperature dependence of ice-on-rock friction at realistic glacier conditions. *Philosophical Transactions of the Royal Society A: Mathematical, Physical and Engineering Sciences*, 375(2086):20150348.

McDowell, I. E., Humphrey, N. F., Harper, J. T., and Meierbachtol, T. W. (2021). The cooling signature of basal crevasses in a hard-bedded region of the Greenland Ice Sheet. *The Cryosphere*, 15(2):897–907.

Meredith, M., Sommerkorn, M., Cassotta, S., Derksen, C., Ekaykin, A., Hollowed, A., Kofinas, G., Mackintosh, A., Melbourne-Thomas, J., Muelbert, M., et al. (2019). Polar regions. chapter 3, ipcc special report on the ocean

and cryosphere in a changing climate. *IPCC special report on the ocean and cryosphere in a changing climate*.

Minchew, B., Simons, M., Riel, B., and Milillo, P. (2017). Tidally induced variations in vertical and horizontal motion on Rutford Ice Stream, West Antarctica, inferred from remotely sensed observations. *Journal of Geophysical Research: Earth Surface*, 122(1):167–190.

Morlighem, M., Rignot, E., Binder, T., Blankenship, D., Drews, R., Eagles, G., Eisen, O., Ferraccioli, F., Forsberg, R., Fretwell, P., et al. (2020). Deep glacial troughs and stabilizing ridges unveiled beneath the margins of the Antarctic ice sheet. *Nature geoscience*, 13(2):132–137.

Morlighem, M., Williams, C. N., Rignot, E., An, L., Arndt, J. E., Bamber, J. L., Catania, G., Chauché, N., Dowdeswell, J. A., Dorschel, B., et al. (2017). BedMachine v3: Complete bed topography and ocean bathymetry mapping of Greenland from multibeam echo sounding combined with mass conservation. *Geophysical research letters*, 44(21):11–051.

Mosbeux, C., Wagner, T. J., Becker, M. K., and Fricker, H. A. (2020). Viscous and elastic buoyancy stresses as drivers of ice-shelf calving. *Journal of Glaciology*, 66(258):643–657.

Mouginot, J., Rignot, E., Scheuchl, B., and Millan, R. (2017). Comprehensive annual ice sheet velocity mapping using Landsat-8, Sentinel-1, and RADARSAT-2 data. *Remote Sensing*, 9(4):364.

Mouginot, J., Scheuchl, B., and Rignot, E. (2012). Mapping of ice motion in Antarctica using synthetic-aperture radar data. *Remote Sensing*, 4(9):2753–2767.

Moussavi, M. S., Abdalati, W., Pope, A., Scambos, T., Tedesco, M., MacFerrin,

M., and Grigsby, S. (2016). Derivation and validation of supraglacial lake volumes on the Greenland Ice Sheet from high-resolution satellite imagery. *Remote sensing of environment*, 183:294–303.

Muszynski, I. and Birchfield, G. (1987). A coupled marine ice-stream–ice-shelf model. *Journal of Glaciology*, 33(113):3–15.

Nowicki, S. and Wingham, D. (2008). Conditions for a steady ice sheet–ice shelf junction. *Earth and Planetary Science Letters*, 265(1-2):246–255.

Olive, J.-A., Behn, M. D., Mittelstaedt, E., Ito, G., and Klein, B. Z. (2016). The role of elasticity in simulating long-term tectonic extension. *Geophysical Journal International*, 205(2):728–743.

Pattyn, F. (2018). The paradigm shift in Antarctic ice sheet modelling. *Nature communications*, 9(1):2728.

Pattyn, F. and Morlighem, M. (2020). The uncertain future of the Antarctic Ice Sheet. *Science*, 367(6484):1331–1335.

Pegler, S. S. (2018). Marine ice sheet dynamics: the impacts of ice-shelf buttressing. *Journal of Fluid Mechanics*, 857:605–647.

Podrasky, D., Truffer, M., Lüthi, M., and Fahnestock, M. (2014). Quantifying velocity response to ocean tides and calving near the terminus of Jakobshavn Isbræ, Greenland. *Journal of Glaciology*, 60(222):609–621.

Pritchard, H. D., Ligtenberg, S. R., Fricker, H. A., Vaughan, D. G., van den Broeke, M. R., and Padman, L. (2012). Antarctic ice-sheet loss driven by basal melting of ice shelves. *Nature*, 484(7395):502–505.

Reeh, N. (1968). On the calving of ice from floating glaciers and ice shelves. *Journal of Glaciology*, 7(50):215–232.

Reeh, N., Christensen, E. L., Mayer, C., and Olesen, O. B. (2003). Tidal bending of glaciers: a linear viscoelastic approach. *Annals of Glaciology*, 37:83–89.

Reeh, N., Mayer, C., Olesen, O. B., Christensen, E. L., and Thomsen, H. H. (2000). Tidal movement of Nioghalvfjerdsfjorden glacier, northeast Greenland: observations and modelling. *Annals of Glaciology*, 31:111–117.

Rignot, E., Mouginot, J., Morlighem, M., Seroussi, H., and Scheuchl, B. (2014). Widespread, rapid grounding line retreat of Pine Island, Thwaites, Smith, and Kohler glaciers, West Antarctica, from 1992 to 2011. *Geophysical Research Letters*, 41(10):3502–3509.

Rignot, E., Mouginot, J., and Scheuchl, B. (2011a). Antarctic grounding line mapping from differential satellite radar interferometry. *Geophysical Research Letters*, 38(10).

Rignot, E., Mouginot, J., and Scheuchl, B. (2011b). Ice flow of the Antarctic ice sheet. *Science*, 333(6048):1427–1430.

Rignot, E., Mouginot, J., and Scheuchl, B. (2016a). MEaSUREs Antarctic Grounding Line from Differential Satellite Radar Interferometry, Version 2.

Rignot, E., Mouginot, J., and Scheuchl, B. (2016b). MEaSUREs Antarctic Grounding Line from Differential Satellite Radar Interferometry, Version 2.

Rignot, E., Mouginot, J., and Scheuchl., B. (2017). MEaSUREs InSAR-Based Antarctica Ice Velocity Map, Version 2.

Rignot, E., Mouginot, J., Scheuchl, B., Van Den Broeke, M., Van Wessem, M. J., and Morlighem, M. (2019). Four decades of Antarctic Ice Sheet mass balance from 1979–2017. *Proceedings of the National Academy of Sciences*, 116(4):1095–1103.

Rist, M., Sammonds, P., Murrell, S., Meredith, P., Oerter, H., and Doake, C. (1996). Experimental fracture and mechanical properties of Antarctic ice: preliminary results. *Annals of glaciology*, 23:284–292.

Robel, A. A., Tsai, V. C., Minchew, B., and Simons, M. (2017). Tidal modulation of ice shelf buttressing stresses. *Annals of glaciology*, 58(74):12–20.

Rosier, S. H. R. and Gudmundsson, G. H. (2020). Exploring mechanisms responsible for tidal modulation in flow of the Filchner–Ronne Ice Shelf. *The Cryosphere*, 14(1):17–37.

Rosier, S. H. R., Gudmundsson, G. H., and Green, J. A. M. (2015). Temporal variations in the flow of a large Antarctic ice stream controlled by tidally induced changes in the subglacial water system. *The Cryosphere*, 9(4):1649–1661.

Rosier, S. H. R., Gudmundsson, G. H., and Green, J. M. (2014). Insights into ice stream dynamics through modelling their response to tidal forcing. *The Cryosphere*, 8(5):1763–1775.

Sartore, N. B., Wagner, T. J., Siegfried, M. R., Pujara, N., and Zoet, L. K. (2024). Calving of Ross Ice Shelf from wave erosion and hydrostatic stresses. *EGUsphere*, 2024:1–23.

Sayag, R. and Worster, M. G. (2011). Elastic response of a grounded ice sheet coupled to a floating ice shelf. *Physical Review E*, 84(3):036111.

Scambos, T., Hulbe, C., Fahnestock, M., and Bohlander, J. (2000). The link between climate warming and break-up of ice shelves in the Antarctic Peninsula. *Journal of Glaciology*, 46(154):516–530.

Scambos, T., Sergienko, O., Sargent, A., MacAyeal, D., and Fastook, J. (2005). ICESat profiles of tabular iceberg margins and iceberg breakup at low latitudes. *Geophysical Research Letters*, 32(23).

Schoof, C. (2007a). Ice sheet grounding line dynamics: Steady states, stability, and hysteresis. *Journal of Geophysical Research: Earth Surface*, 112(F3).

Schoof, C. (2007b). Marine ice-sheet dynamics. Part 1. The case of rapid sliding. *Journal of Fluid Mechanics*, 573:27–55.

Schoof, C. (2012). Marine ice sheet stability. *Journal of Fluid Mechanics*, 698:62–72.

Schulson, E., Lim, P., and Lee, R. (1984). A brittle to ductile transition in ice under tension. *Philosophical Magazine A*, 49(3):353–363.

Sergienko, O. and Haseloff, M. (2023). 'Stable'and 'unstable'are not useful descriptions of marine ice sheets in the Earth's climate system. *Journal of Glaciology*, pages 1–17.

Sergienko, O. V. and Hindmarsh, R. C. (2013). Regular patterns in frictional resistance of ice-stream beds seen by surface data inversion. *Science*, 342(6162):1086–1089.

Sergienko, O. V., MacAyeal, D. R., and Bindschadler, R. A. (2009). Stick–slip behavior of ice streams: modeling investigations. *Annals of Glaciology*, 50(52):87–94.

Sinha, N. K. (1978). Short-term rheology of polycrystalline ice. *Journal of Glaciology*, 21(85):457–474.

Slater, D., Benn, D., Cowton, T., Bassis, J., and Todd, J. (2021). Calving multiplier effect controlled by melt undercut geometry. *Journal of Geophysical Research: Earth Surface*, 126(7):e2021JF006191.

Slater, D., Straneo, F., Das, S., Richards, C., Wagner, T., and Nienow, P. (2018).

Localized plumes drive front-wide ocean melting of a Greenlandic tidewater glacier. *Geophysical Research Letters*, 45(22):12–350.

Smith, R. (1976). The application of fracture mechanics to the problem of crevasse penetration. *Journal of Glaciology*, 17(76):223–228.

Stevens, L. A., Behn, M. D., McGuire, J. J., Das, S. B., Joughin, I., Herring, T., Shean, D. E., and King, M. A. (2015). Greenland supraglacial lake drainages triggered by hydrologically induced basal slip. *Nature*, 522(7554):73–76.

Stevens, L. A., Nettles, M., Davis, J. L., Creyts, T. T., Kingslake, J., Hewitt, I. J., and Stubblefield, A. (2022). Tidewater-glacier response to supraglacial lake drainage. *Nature Communications*, 13(1):6065.

Stokes, C. R., Clark, C. D., Lian, O. B., and Tulaczyk, S. (2007). Ice stream sticky spots: a review of their identification and influence beneath contemporary and palaeo-ice streams. *Earth-Science Reviews*, 81(3-4):217–249.

Stokes, C. R., Sanderson, J. E., Miles, B. W., Jamieson, S. S., and Leeson, A. A. (2019). Widespread distribution of supraglacial lakes around the margin of the East Antarctic Ice Sheet. *Scientific reports*, 9(1):13823.

Stubblefield, A. G., Spiegelman, M., and Creyts, T. T. (2021). Variational formulation of marine ice-sheet and subglacial-lake grounding-line dynamics. *Journal of Fluid Mechanics*, 919.

Tada, H., Paris, P., and Irwin, G. (2000). *The Analysis of Cracks Handbook*, volume 2. New York: ASME Press.

Tedesco, M., Lüthje, M., Steffen, K., Steiner, N., Fettweis, X., Willis, I., Bayou, N., and Banwell, A. (2012). Measurement and modeling of ablation of the bottom of supraglacial lakes in western Greenland. *Geophysical Research Letters*, 39(2).

Tedesco, M., Willis, I. C., Hoffman, M. J., Banwell, A. F., Alexander, P., and Arnold, N. S. (2013). Ice dynamic response to two modes of surface lake drainage on the Greenland ice sheet. *Environmental Research Letters*, 8(3):034007.

Timoshenko, S. (1955). *Strength of Materials*. Number pt. 1 in Strength of Materials. Van Nostrand.

Trusel, L. D., Pan, Z., and Moussavi, M. (2022). Repeated tidally induced hydrofracture of a supraglacial lake at the Amery Ice Shelf grounding zone. *Geophysical Research Letters*, 49(7):e2021GL095661.

Tsai, V. C., Stewart, A. L., and Thompson, A. F. (2015). Marine ice-sheet profiles and stability under Coulomb basal conditions. *Journal of Glaciology*, 61(226):205–215.

Turcotte, D. L. and Schubert, G. (2002). *Geodynamics*. Cambridge university press.

Van der Veen, C. J. (1998). Fracture mechanics approach to penetration of bottom crevasses on glaciers. *Cold Regions Science and Technology*, 27(3):213–223.

Van der Veen, C. J. (2013). *Fundamentals of Glacier Dynamics*. CRC Press.

Vaughan, D. G. (1995). Tidal flexure at ice shelf margins. *Journal of Geophysical Research: Solid Earth*, 100(B4):6213–6224.

Wagner, T. J., James, T. D., Murray, T., and Vella, D. (2016). On the role of buoyant flexure in glacier calving. *Geophysical Research Letters*, 43(1):232–240A.

Wagner, T. J., Wadhams, P., Bates, R., Elosegui, P., Stern, A., Vella, D., Abrahamsen, E. P., Crawford, A., and Nicholls, K. W. (2014). The "footloose"

mechanism: Iceberg decay from hydrostatic stresses. *Geophysical Research Letters*, 41(15):5522–5529.

WaIters, R. A. (1989). Small-amplitude, short-period variations in the speed of a tide-water glacier in south-central Alaska, USA. *Annals of glaciology*, 12:187–191.

Walker, R. T., Parizek, B. R., Alley, R. B., Anandakrishnan, S., Riverman, K. L., and Christianson, K. (2013). Ice-shelf tidal flexure and subglacial pressure variations. *Earth and Planetary Science Letters*, 361:422–428.

Walter, F., Dalban Canassy, P., Husen, S., and Clinton, J. F. (2013). Deep ice-quakes: What happens at the base of Alpine glaciers? *Journal of Geophysical Research: Earth Surface*, 118(3):1720–1728.

Warburton, K. L., Hewitt, D. R., and Neufeld, J. A. (2020). Tidal grounding-line migration modulated by subglacial hydrology. *Geophysical Research Letters*, 47(17):e2020GL089088.

Warner, R. C., Fricker, H. A., Adusumilli, S., Arndt, P., Kingslake, J., and Spergel, J. J. (2021). Rapid formation of an ice doline on Amery Ice Shelf, East Antarctica. *Geophysical Research Letters*, 48(14):e2020GL091095.

Wearing, M. (2017). *The flow dynamics and buttressing of ice shelves*. PhD thesis, University of Cambridge.

Wearing, M. and Kingslake, J. (2019). Holocene formation of Henry Ice Rise, West Antarctica, inferred from ice-penetrating radar. *Journal of Geophysical Research: Earth Surface*, 124(8):2224–2240.

Wearing, M. G., Hindmarsh, R. C., and Worster, M. G. (2015). Assessment of ice flow dynamics in the zone close to the calving front of Antarctic ice shelves. *Journal of Glaciology*, 61(230):1194–1206.

Weertman, J. (1957). On the sliding of glaciers. *Journal of glaciology*, 3(21):33–38.

Wiens, D. A., Anandakrishnan, S., Winberry, J. P., and King, M. A. (2008). Simultaneous teleseismic and geodetic observations of the stick–slip motion of an Antarctic ice stream. *Nature*, 453(7196):770–774.

Wilner, J. A., Morlighem, M., and Cheng, G. (2023). Evaluation of four calving laws for Antarctic ice shelves. *The Cryosphere Discussions*, 2023:1–19.

Wolovick, M. J., Creyts, T. T., Buck, W. R., and Bell, R. E. (2014). Traveling slippery patches produce thickness-scale folds in ice sheets. *Geophysical Research Letters*, 41(24):8895–8901.

Yu, H., Rignot, E., Morlighem, M., and Seroussi, H. (2017). Iceberg calving of Thwaites Glacier, West Antarctica: full-Stokes modeling combined with linear elastic fracture mechanics. *The Cryosphere*, 11(3):1283–1296.

Zhang, H., Davis, T., Katz, R. F., Stevens, L. A., and May, D. A. (2023). Basal hydrofractures near sticky patches. *Journal of Glaciology*, 69(275):475–486.

Zhong, M., Simons, M., Minchew, B., and Zhu, L. (2023). Inferring Tide-Induced Ephemeral Grounding in an Ice-Shelf-Stream System: Rutford Ice Stream, West Antarctica. *Journal of Geophysical Research: Earth Surface*, 128(2):e2022JF006789.

Zoet, L., Ikari, M., Alley, R., Marone, C., Anandakrishnan, S., Carpenter, B., and Scuderi, M. (2020). Application of constitutive friction laws to glacier seismicity. *Geophysical Research Letters*, 47(21):e2020GL088964.

A | Appendix

A.1 Appendix A. 2D elasticity in terms of perturbation stress

The domain is a notched ice strip with length $2L$ as shown in Figure 2.1. We set $L \gg W$ to make sure the crack is far from the boundaries to avoid any edge effects. Substituting $\boldsymbol{T} = \boldsymbol{\sigma} + p_i \boldsymbol{I}$ into the governing equation and boundary conditions, we can express the stress equilibrium equation in terms of the perturbation stress as

$$\boldsymbol{\nabla} \cdot \boldsymbol{T} = \boldsymbol{0}. \tag{A1}$$

For the top boundary, a traction-free boundary condition is imposed as

$$\boldsymbol{T} \cdot \boldsymbol{n} = \boldsymbol{0} \quad \text{for} \quad z = H, \tag{A2}$$

where $\boldsymbol{n}$ is the outward-pointing unit normal vector of the domain. On both sides, we impose traction-free boundary condition for the perturbation stress,

$$\boldsymbol{T} \cdot \boldsymbol{n} = \boldsymbol{0} \quad \text{for} \quad x = \pm L. \tag{A3}$$

On the crack walls ($x = W$, $0 \leq z \leq Z_C$), compression caused by static water pressure is imposed as

$$\boldsymbol{T} \cdot \boldsymbol{n} = \begin{cases} \rho_i g H \left[\left(\dfrac{\rho_w}{\rho_i} - 1 \right) \dfrac{z}{H} + 1 - f \right] \boldsymbol{n} & \text{for} \quad z < H_w, \\ \rho_i g H \left(-\dfrac{z}{H} + 1 \right) \boldsymbol{n} & \text{for} \quad z \geq H_w, \end{cases} \tag{A4}$$

where $\rho_i f H/\rho_w = H_w$ is the hydraulic head. The bottom boundary condition remains the same as (2.5) and (2.4), and since the overburden stress doesn't contribute to the shear stress and the elastic deformation,

$$\boldsymbol{t}\cdot\boldsymbol{T}\cdot\boldsymbol{n} = \tau\left(x,0\right) = \begin{cases} -\dfrac{W}{L}\Delta\tau & |x| \geq W, \\ \left(1-\dfrac{W}{L}\right)\Delta\tau & |x| < W, \end{cases} \tag{A5}$$

$$\boldsymbol{u}\cdot\boldsymbol{n} = 0. \tag{A6}$$

Here $\boldsymbol{t} = -\hat{\boldsymbol{x}}$ is the unit tangent vector to the bottom boundary. Note that in Eq. A5 an extra term $-W\Delta\tau/L$ is added on the bottom boundary in order to maintain the total force balance of the ice strip. Because $L \gg W$, we can neglect the near-field effect of this force-balance term.

Different from standard elasticity, we set up a constitutive relation between the *perturbation* stress tensor $\boldsymbol{T}$ and the strain tensor $\boldsymbol{\epsilon}$ as in Eq. 2.9.

A.2 Appendix B. Benchmark

The weight function method has proved to be a useful tool to calculate stress intensity factors in ice sheets under certain basal boundary conditions (Tada et al., 2000; Jimenez and Duddu, 2018). In essence, this involves calculating stress intensity factors by integrating the stress along a hypothesised crack in an uncracked domain with an appropriate weight function. The advantage of the weight function method is that the computation is performed in the uncracked domain with no discontinuity and singularity caused by cracks. For certain simple domain and crack geometry and boundary conditions, the weight function method can give SIFs with high accuracy.

Jimenez and Duddu (2018) has provided the appropriate weight function from Tada et al. (2000) to be used for basal cracks in a grounded ice-sheet,

$$K_I = \int_0^{Z_C} \sigma_{xx}(z)\, G_1(\lambda, \gamma)\, \mathrm{d}z, \tag{C1}$$

$$G_1(\lambda, \gamma) = \frac{2}{\sqrt{2H}} \sqrt{\frac{\tan\left(\frac{\pi\lambda}{2}\right)}{1 - \cos\frac{\pi\lambda}{2}/\cos\frac{\pi\lambda\gamma}{2}}} \left\{1 + 0.297\sqrt{1-\gamma^2}\left[1 - \cos\left(\frac{\pi}{2}\lambda\right)\right]\right\}, \tag{C2}$$

where $\lambda = Z_C/H$ is the non-dimensional crack length and $\gamma = z/Z_C$ is the z coordinate normalised by the crack length. This weight function can be used to predict the mode-I stress intensity factor K_I in grounded ice. A similar weight function in Tada et al. (2000) can also be applied to calculating mode-II stress intensity factor,

$$K_{II} = \int_0^{Z_C} \sigma_{xz}(z)\, G_2(\lambda, \gamma)\, \mathrm{d}z, \tag{C3}$$

$$G_2(\lambda, \gamma) = \frac{2}{\sqrt{2H}} \sqrt{\frac{\tan\left(\frac{\pi\lambda}{2}\right)}{1 - \cos\frac{\pi\lambda}{2}/\cos\frac{\pi\lambda\gamma}{2}}} \left\{1 + 0.297\sqrt{1-\gamma^2}\left[1 - \cos\left(\frac{\pi}{2}\lambda\right)\right]\right\} \frac{\sin\frac{\pi\lambda\gamma}{2}}{\sin\frac{\pi\lambda}{2}}. \tag{C4}$$

To verify the implementation of the DCM method we consider a problem where there is a mixed-mode (mode-I and mode-II) water-filled crack. SIFs are calculated by both the DCM method and the weight function method in Figure A.1. In the DCM calculation, the element size is set to be 0.005 times the crack length near the crack tip and 0.2 ice thicknesses away from the tip.

For K_I, these two methods agree over most crack lengths. However, there is large deviation for K_{II} at large crack length, likely due to the limitations of the DCM

method when the crack tip is near the boundaries. As the crack tip approaches a boundary, the stress singularity introduces errors into the displacement calculation, leading to the observed discrepancy between the DCM method and the analytical solution. Since we do not consider mode-II fractures in chapter 2, the deviation doesn't change the results.

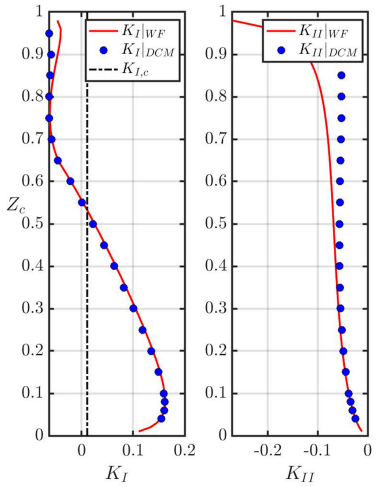

Figure A.1: Stress intensity factors K_I and K_{II} when $\Delta\tau' = 0.3$ and $f = 0.7$. The red lines show SIFs calculated by the weight function method ("WF" in the legend means "weight function"). The blue dots show SIFs calculated by DCM.

A.3 Appendix C. Thermal Structure of basal crevasses

A.3.1 Thermal structure of a single basal crevasse

Refreezing of water inside basal crevasses is a factor potentially affecting the thermal profile of ice. Using analytical solutions of Carslaw and Jaeger (1959), this section shows how a single basal crevasse or a series of basal crevasses affects the thermal structure of ice.

In order to simplify the computation, we neglect advection and other englacial

heat sources and focus on heat diffusion after refreezing (Luckman et al., 2012). The background temperature profile is assumed to have no effect on the heat conduction caused by refreezing. That means that the simple analytical model just accounts for the effect of refreezing and doesn't make any prediction of the net temperature profile. Let ΔT be the temperature perturbation induced by a basal crevasse. The ice sheet is simplified to an isotropic infinite strip $0 < z < H$. On the boundaries we assume zero temperature perturbation ($\Delta T = 0$) at $z = 0$, $z = H$ and $x = \pm\infty$. The governing equation of thermal conduction in terms of ΔT is

$$\frac{\partial^2 \Delta T}{\partial x^2} + \frac{\partial^2 \Delta T}{\partial z^2} = \frac{1}{\kappa}\frac{\partial \Delta T}{\partial t}, \tag{E1}$$

where κ is the thermal diffusivity of ice.

The boundary conditions are

$$\Delta T\left(\pm\infty, z\right) = 0, \tag{E2}$$

$$\Delta T\left(x, 0\right) = \Delta T\left(x, H\right) = 0. \tag{E3}$$

Table A.1 shows the values of parameters used in the calculation. At time $t = 0$, an amount of heat q_i per unit length per unit depth into the page is released by a line heat source from $(0, 0)$ to $(0, Z_c)$. In order to get an estimated value of that released heat, we need to estimate the volume of water that refreezes at $t = 0$. Based on the BEM simulations, the width of the crack w is approximately 0.1 m and hence q_i is estimated as

$$q_i = \rho_i L w = 3 \times 10^7 \text{ J m}^{-2}, \tag{E4}$$

where L is the latent heat of melting.

Thus we have the full thermal problem in an infinite strip with an initial line heat

source representing refreezing in real basal crevasses.

Table A.1: Constants used in calculation of temperature around basal crevasses.

Physical property	Notation	Value
Density of water	ρ_w	1.0×10^3 kg $\cdot$ m^{-3}
Density of ice	ρ_i	0.92×10^3 kg $\cdot$ m^{-3}
Latent heat of fusion	L	3.34×10^5 J $\cdot$ kg^{-1}
Thermal Conductivity	k	2.1 W $\cdot$ m^{-1}K^{-1}
Heat capacity of ice	C_p	2.10×10^3 J $\cdot$ kg^{-1} $\cdot$ K^{-1}
Thermal diffusivity	κ	1.09×10^{-6} m^2 $\cdot$ s^{-1}
Sliding velocity	v_s	1.0×10^2 m $\cdot$ y^{-1}
Crevasse spacing	w_s	1.0×10^2 m

The solutions are given by Carslaw and Jaeger (1959) as

$$\Delta T = \frac{q_i}{\pi \rho_i C_p \sqrt{\kappa \pi t}} \exp\left(-\frac{(x-x')^2}{4\kappa t}\right) \sum_{n=1}^{+\infty} \frac{1}{n}\left(1-\cos\left(\frac{n\pi Z_C}{H}\right)\right) \sin\left(\frac{n\pi z}{H}\right) \exp\left(\frac{-\kappa n^2 \pi^2 t}{H^2}\right). \quad \text{(E5)}$$

A.3.2 Thermal structure of a series of equally spaced basal crevasses

A stable sticky patch can cause a local stress variation and potentially generate a series of basal crevasses. The thermal effect of a single basal crevasse, which is shown above, can be advected downstream and superposed with the effect of other basal crevasses, resulting in temperature variation on a longer timescale and larger area. Mathematically, based on $\Delta T\,(x, z, t)$ that we have obtained above, the net effect of a series of basal crevasses can be obtained by a simple linear superposition of the ΔT of each crevasse.

Assuming these crevasses are generated at a fixed spacing $w_s = W = 100$ m in

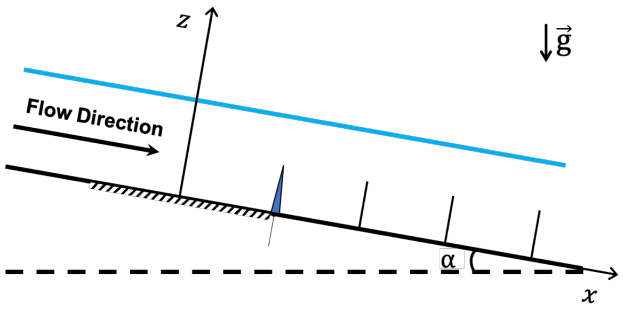

Figure A.2: Schematic of a series of basal crevasses produced on a sticky patch.

an 100-m-thick ice sheet, starting from $t = 0$, we fix the coordinate system on the sticky patch and move the ice sheet at $v_s = 100$ my^{-1}. Thus the crevasses are also generated at a fixed time interval $\Delta t = W/v_s = 1$ y. The net temperature perturbation ΔT_{net} is

$$\Delta T_{net} = \sum_{n=0}^{\infty} \Delta T \left(x - x'_n,\ z,\ t - t'_n\right), \tag{E6}$$

where n is the number of the crack, $x'_n = nw_s$ is the position of the crack n, $t'_n = -n\Delta t$ is the time when the crack n formed and refroze. Note that the solution assumes that each crack has moved an integer number of crack separations from the origin, thus is only a demonstration of the thermal perturbations at integer multiples of w_s/v_s.

A.4 Convergence test

This section is a convergence test of the viscoelastic grounding-line model in chapter 3. The convergence test shows the results are mesh-independent. Considering a marine ice sheet with bedslope $\theta = 10^{-3}$ and friction coefficient $C = 7 \times 10^5$, we use the fine-grid solution $x_{g,e}$, σ_e ($\Delta x = 6.25$m) as a best estimate of the exact solution. Here $x_{g,e}$ denotes the time series of the exact GL position, and σ_e denotes the time series of the exact maximum tensile stress on the ice-sheet surface within the lake region $|x - \bar{x}_g| \leq 0.5$ km. As Δx decreases, the GL position x_g and maximum tensile stress $\sigma_{xx,max}$ linearly converge to the fine-grid solution (Fig. A.3). Note that the magnitude of $||x_{g,e}||$ is sensitive to the choice of coordinate origin, thus Fig. A.3 is only a measurement of relative error.

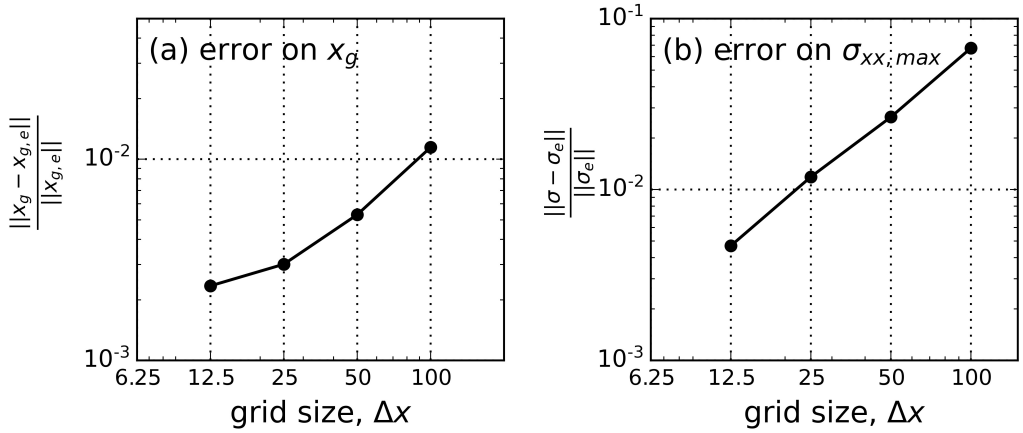

Figure A.3: Convergence of (a) GL position and (b) maximum tensile stress $\sigma_{xx,max}$ with decreasing element size Δx (12.5 m, 25 m, 50 m, 100 m). For simplicity, we denote $\sigma_{xx,max}$ by σ without causing any confusion. Here $x_{g,e}$ and σ_e denote the exact solution to the GL position and maximum tensile stress $\sigma_{xx,max}$, respectively. $||\cdot||$ is the L^2 norm taken over time.

A.5 Simulation with real bed topography

In Fig. A.4 we present model results using the real bed topography shown in Fig. 3.1e (Morlighem et al., 2017, 2020). For comparison, the physical properties of ice and basal slipperiness C are kept the same as in idealised models with a linear bed. The jagged variation of $x_g(t)$ is a consequence of the use of coarse grids near the grounding line for convergence. While the tidal stress and grounding-zone width are modified by bed undulation, the results have an equivalent order of magnitude to the case with linear bed topography, indicating the importance of tidal stress regardless of bed roughness. Therefore, we use the linear bed topography in the model.

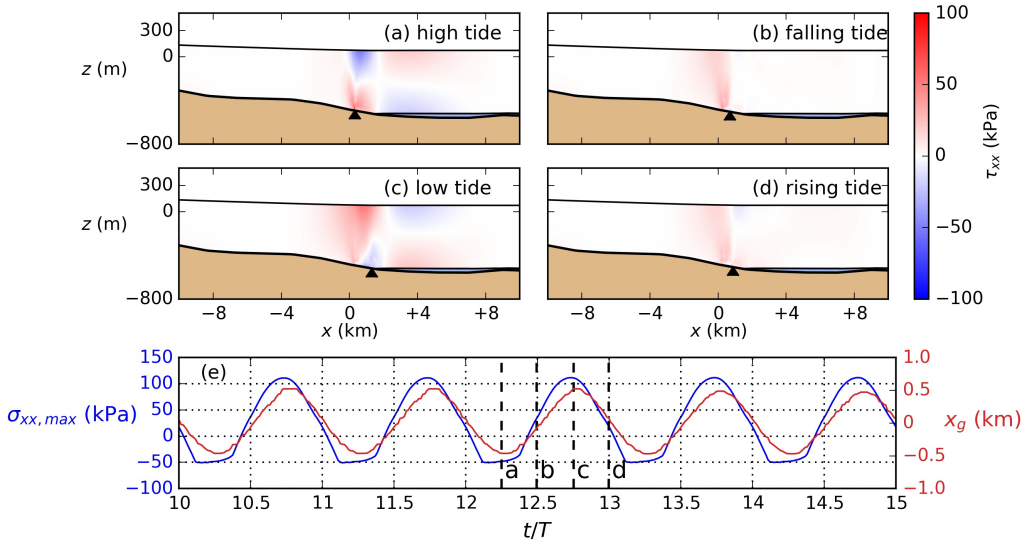

Figure A.4: Tidal response of the Amery Ice Shelf with real bed topography. **(a)–(d)** Deviatoric tensile stress τ_{xx} in one tidal period. **(e)** The maximum tensile stress $\sigma_{xx,max}$ (blue) on the top boundary within the lake region ($\bar{x_g} - 0.5$ km $\leq x \leq \bar{x_g} + 0.5$ km) and the GL position x_g (red) versus time (scaled by the tidal period T) with positive values representing downstream migration. Vertical dashed lines show the time of panels (a)-(d).

A.6 Viscoelastic Euler-Bernoulli beam model

We follow the derivation by Walker et al. (2013). The force balance for an Euler-Bernoulli beam suggests

$$\frac{\partial^2 M}{\partial x^2} = -q, \tag{A.7}$$

$$M(x) = \int_{-\frac{h}{2}}^{\frac{h}{2}} \sigma_{xx} z \mathrm{d}z, \tag{A.8}$$

where M is the bending moment, x is the horizontal coordinate, t is time, $w(x,t)$ is the beam deflection, q is the distributed force, h is the beam thickness and z is the z-coordinate with $z = 0$ on the neutral plane.

Neglecting the advection, the Maxwell viscoelastic constitutional law is

$$\frac{D\sigma_{xx}}{Dt} = \frac{\partial \sigma_{xx}}{\partial t} = E\left(\frac{\partial \varepsilon_{xx}}{\partial t} - \frac{1}{2\eta}\sigma_{xx}\right), \tag{A.9}$$

where E is the modified Young's modulus for plane strain, ν is Poisson's ratio and η is the viscosity that is assumed to be a constant in the following discussion.

The net strain ε_{xx} is related to the curvature κ as

$$\varepsilon_{xx} = -\kappa z = -z\frac{\partial^2 w}{\partial x^2} \tag{A.10}$$

Substituting Eq. A.9 and Eq. A.10 into (A.8) gives

$$\left(\frac{\partial}{\partial t} + \frac{E}{2\nu_s}\right) M = -\left[\frac{Eh^3}{12}\frac{\partial}{\partial t}\frac{\partial^2 w}{\partial x^2}\right]. \tag{A.11}$$

Finally, substituting Eq. A.11 into Eq. A.7 gives the governing equation for $w\left(x,t\right)$

$$\frac{\partial}{\partial t}\left[\frac{\partial^2}{\partial x^2}\left(EI\frac{\partial^2 w}{\partial x^2}\right)\right]=\frac{\partial q\left(x,t\right)}{\partial t}+\frac{E}{2\eta}q\left(x,t\right). \tag{A.12}$$

When $q(x)=-\rho_w g w(x,t)$, we have Eq. 5.7, which is the governing equation for viscoelastic flexure problems in terms of w.

A.6.1 Boundary conditions

The boundary conditions at the ice-shelf edge is

$$\begin{aligned} M&=M_e, \quad x=0,\\ Q=\frac{\partial M}{\partial x}&=Q_e, \quad x=0. \end{aligned} \tag{A.13}$$

Applying the operator $\left(\frac{\partial}{\partial t}+\frac{E}{2\eta}\right)$ to Eq. A.13, then substituting Eq. A.8 and Eq. A.10, we obtain

$$\begin{aligned} \left(\frac{\partial}{\partial t}+\frac{E}{2\eta}\right)M=-\int_{-h/2}^{+h/2}E\frac{\partial}{\partial t}\frac{\partial^2 w}{\partial x^2}z^2dz=-EI\frac{\partial}{\partial t}\frac{\partial^2 w}{\partial x^2}&=\left(\frac{\partial}{\partial t}+\frac{E}{2\eta}\right)M_e, \quad x=0\\ \left(\frac{\partial}{\partial t}+\frac{E}{2\eta}\right)Q=-EI\frac{\partial}{\partial t}\frac{\partial^3 w}{\partial x^3}&=\left(\frac{\partial}{\partial t}+\frac{E}{2\eta}\right)Q_e, \quad x=0. \end{aligned} \tag{A.14}$$

Eq. A.14 can be integrated over time from 0 to t to obtain

$$\begin{aligned} \int_0^t\frac{E}{2\eta}M_e\mathrm{d}\tau+M_e-M_{e,0}&=-EI\left[\frac{\partial^2 w}{\partial x^2}-\frac{\partial^2 w_0}{\partial x^2}\right], \quad x=0,\\ \int_0^t\frac{E}{2\eta}Q_e\mathrm{d}\tau+Q_e-Q_{e,0}&=-EI\left[\frac{\partial^3 w}{\partial x^3}-\frac{\partial^3 w_0}{\partial x^3}\right], \quad x=0, \end{aligned} \tag{A.15}$$

If $Q_e=Q_{e,0}$, Eq. A.15 is reduced to the boundary condition Eq. 5.8.